2010

Effects of Bondline Thickness on Nonlinear Interfacial Fracture of Bonded Adhesive Joint

Gefu Ji
Louisiana State University and Agricultural and Mechanical College

EFFECTS OF BONDLINE THICKNESS ON NONLINEAR INTERFACIAL FRACTURE OF BONDED ADHESIVE JOINT

A Dissertation

Submitted to the Graduate Faculty of the
Louisiana State University and
Agricultural and Mechanical College
in partial fulfillment of the
requirements for the degree of
Doctor of Philosophy

in

The Interdepartmental Program in Engineering Science

by
Gefu Ji
B.S., HuaZhong Agriculture University, Wuhan, China, June 2001
M.E., Southern University A&M College, Baton Rouge, LA, July 2006
M.S., Louisiana State University, Baton Rouge, LA, December 2008
December 2010

ACKNOWLEDGEMENTS

I would like to acknowledge the guidance and support provided by my major professor, Dr. Guoqiang Li and Dr. Zhenyu Ouyang during the course of this research work. This work would not have been possible without the extensive help and guidance by them. I would also like to thank the support and guidance of my graduate committee, Dr. Su-Seng Pang, Dr. Wanjun Wang, Dr. Steve Cai and Dr. Evanna Gleason, who is acting as the Dean's representative.

I wish to acknowledge my wife, and parents for the constant moral support they provided in pursuing this study. Also the help from my lab mates and family friends is greatly acknowledged.

This study is based upon work supported by the NSF under grant number (NSF CMMI 0900064), NASA/EPSCoR under grant number NASA/LEQSF (2007-10)-Phase3-01, and LONI institute under the grant number LEQSF (2007-12)-ENH-PKSFI-PRS-01 (Subcontract number: 17120).

TABLE OF CONTENTS

LIST OF TABLES

LIST OF FIGURES

ABSTRACT

A number of existing and emerging industrial applications are dependent on layered substrates through adhesive bonding. The interfacial fracture of adhesively bonded structures is a critical issue for its extensive applications to a variety of modern industries. In the recent two decades, cohesive zone models (CZMs) have been receiving intensive attentions for fracture problems of adhesively bonded joints due to its fairly simple and accurate predictive ability. In CZMs the nonlinear interfacial fracture behaviors are described by the traction-separation laws (also referred to as cohesive laws). The cohesive laws represent the local constitutive behavior, instead of the global parameter, such as toughness.

While numerous global tests have been conducted to measure the interfacial toughness of adhesive joints, limited local tests have been conducted to determine the interfacial traction-separation laws or interfacial cohesive laws. Among the limited local tests in some recent experimental studies, very few studies have considered the effects of adhesive thickness on the local interfacial traction-separation laws. In the present work, within the framework of nonlinear fracture mechanics, comprehensive experimental studies are conducted to investigate the effect of adhesive layer thickness on the local nonlinear interfacial behaviors. The fracture tests of adhesive joints with various adhesive layer thicknesses were conducted under different fracture modes: pure Mode-I (peel fracture), pure Mode-II (shear fracture), and mixed Mode I/II. The experimentally determined interfacial traction-separation laws provide valuable baseline data for parameter calibrations in numerical models. The current experimental results may also

facilitate the understanding of adhesive thickness dependent interface fracture of bonded joints.

CHAPTER 1

INTRODUCTION

1. 1Background

1.1.1 Adhesive Bonding Technology

The most primitive form of adhesive bonding technology can be traced back to 200,000 BC when people in central Italy glued spear stone flakes to a wood with birch-bark-tar (Mazza *et al*., 2006). Today adhesive bonding technology has been used in a wide variety of modern industries, such as automotive, aerospace, marine, construction, and military. Many components and structures, from microchips to large aircrafts, are made of materials arranged in layers through adhesive bonding (Ouyang and Li, 2009a).

The strength of attachment, or adhesion, between an adhesive and its substrate depends on the mechanisms of adhesion and the surface area over which the two materials contact. The mechanisms of adhesion can be categorized as mechanical, chemical, dispersive, electrostatic, or diffusive. Mechanical adhesion occurs when adhesive materials fill the voids or pores of the surfaces and the surfaces are held together by interlocking; chemical adhesion is developed when the two materials form a compound at the joint; dispersive adhesion is realized through the attraction between two molecules with regions of slight positive and negative charge (i.e., van der Waals forces); electrostatic adhesion happens when some conducting materials pass electrons to form a difference in electrical charge at the joint; finally, diffusive adhesion is realized when the molecules of both materials are mobile and soluble in each other and merge at the joint by diffusion (Comyn, 1997; Kinloch, 1987).

1.1.2 Three Basic Modes of Fracture

Failure of the adhesive joint imposes a major threat to the reliability of adhesively bonded structures. There are three basic modes of fracture, which are opening (mode I), shear (mode II), and tearing (mode III), as shown in Fig. 1.1.1. A fracture is considered as Mode I when the tensile stress is normal to the plane of the crack. When the shear stress acts parallel to the plane of the crack and perpendicular to the crack front, the fracture is considered Mode II. Mode III is characterized by a shear stress acting parallel to the plane of the crack and parallel to the crack font. In reality, however, all three modes occur simultaneously. In other words, it is a mixed mode.

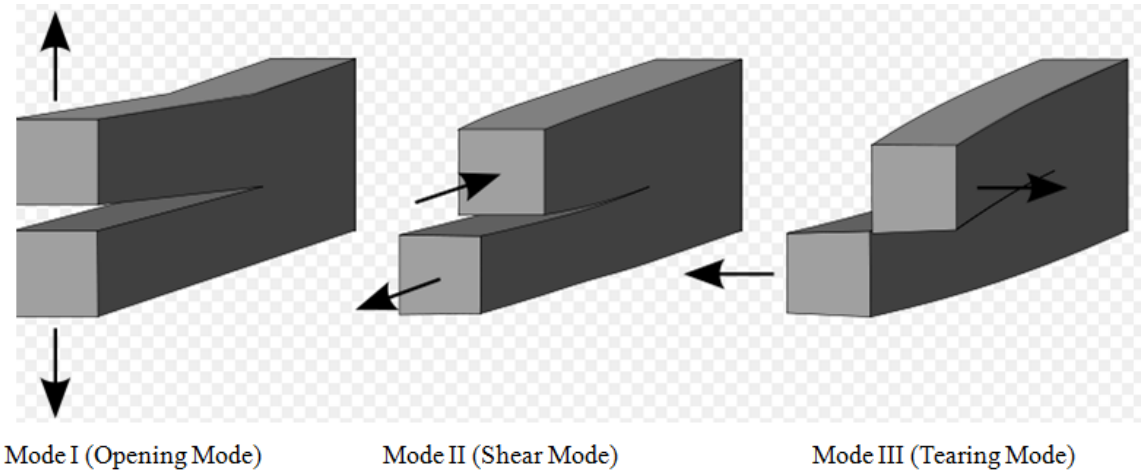

Figure 1.1.1: Three basic fracture modes (Twisp, 2008)

1.2 Classical Fracture Mechanics

During the World War I, many steel structures failed at low temperature. English aeronautical engineer, A. A. Griffith, provided a theory to explain the failure of brittle materials and built up the fundamental research of the Linear Elastic Fracture Mechanics,

as shown in Fig. 1.2.1. (Griffith, 1921). A major limitation of Griffith's theory is that it assumes infinite stress at the initial crack tip point as the radius "r" approaches zero. This is impossible in reality. Therefore, in 1954, Irwin modified the Griffith theory and proposed a plastic zone developed from the initial crack tip, as shown in Fig. 1.2.1. As the applied load increases, the plastic zone increases in size until the crack grows and the material behind the crack tip unloads. The plastic loading and unloading cycle near the crack tip leads to the dissipation of energy as heat. Hence, a dissipative term has to be added to the energy balance relation devised by Griffith for brittle materials. In physical terms, additional energy is needed for crack growth in ductile materials when compared to brittle materials (Irwin 1954). However, one basic assumption in Irwin's linear elastic fracture mechanics is that the size of the plastic zone is small compared to the crack length. This assumption is quite restrictive for certain types of failure in structural steels though such steels can be prone to brittle fracture, which has led to a number of catastrophic failures (Irwin 1954).

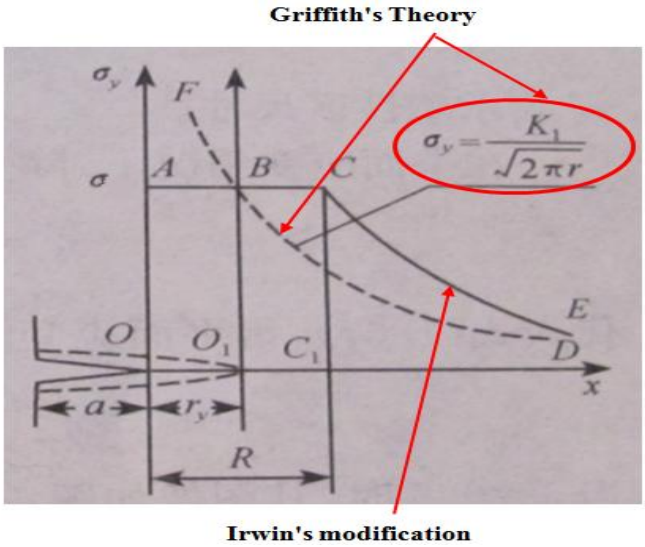

Figure 1.2.1: Griffith's theory and Irwin's modification theory (Irwin 1954)

In the following three decades, numerous studies had been contributed to failure problems of bonded joints (Hutchison and Evans 2000). During this stage, most efforts were focused on the classical linear elastic fracture mechanics (LEFM). The advantage of LEFM lies in the obvious simplicity and decent accuracy, especially for relatively brittle materials and interfaces. Within the framework of LEFM, the remote loadings can be correlated to the critical conditions (crack growth) by a local parameter: stress intensity factor (SIF) or a global parameter: strain energy release rate (ERR). Despite the huge success of LEFM, the assumption of small-scale yielding beyond the crack tip has been identified as one of the major limitations. Specifically, with the increased use of modern toughened adhesives, the cohesive fracture associated with plastic zones along the adhesive interlayer, in many cases, could be comparable to or even larger than the thickness of the adherends.

1.3 Nonlinear Fracture Mechanics

1.3.1 Cohesive Zone Method

Motivated by this limitation of LEFM, a number of efforts have been made along the direction of nonlinear fracture mechanics (NLFM). In the late 1950s and early 1960s, Barrenblatt (1959) and Dugdale (1960) independently proposed the concept of cohesive zone. Specifically, the stresses across a potential crack path were bounded, and a localized traction-separation law may be able to describe the fracture behaviors within the cohesive processing zone ahead of the apparent crack tip, as shown in Fig.1.3.1.

The stresses vary with the relative surface separations according to the assumed interface law during the fracture process.

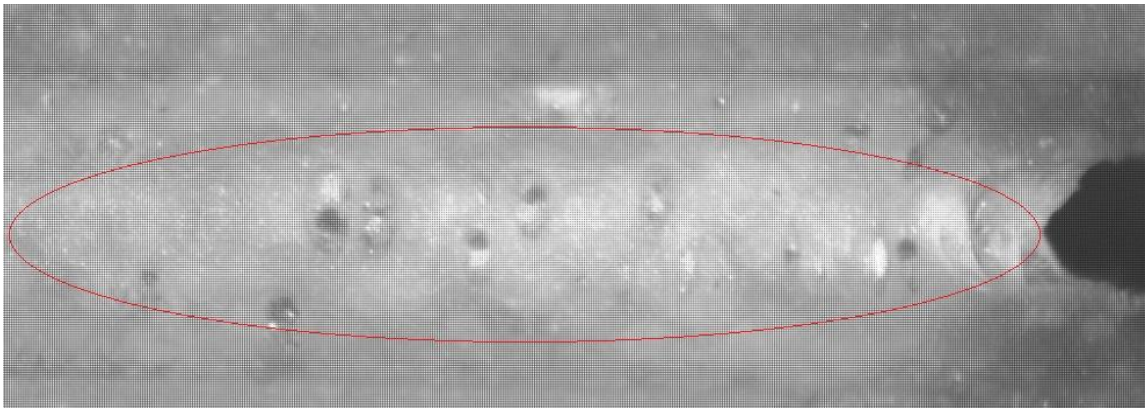

Figure 1.3.1 Cohesive Zone at Mode I Test

1.3.2 J-Integral

Also during this period of time, Rice (1968) proposed a path independent integral method to calculate the energy release rate (ERR), which is referred to as the well-known *J*-integral.

$$J = \int_{\Gamma} (W dy - T \frac{\partial u}{\partial x} ds) \qquad (1)$$

where $W(x, y)$ is the strain energy density; x and y are the coordinate directions, $T = n \cdot \sigma$ is the traction vector; $\boldsymbol{n}$ is the normal to the curve or path Γ, σ is the Cauchy stress, and $\boldsymbol{u}$ is the displacement vector (Rise,1968).

This method can describe the case when there is sufficient crack-tip deformation and the part no longer obeys the linear-elastic approximation. Rice's analysis, which assumes non-linear elastic (or monotonic deformation-theory plastic) deformation ahead of the crack tip, is designated as the J integral (Rice, 1968). This analysis is limited to some situations. First, plastic deformation at the crack tip can not extend to the furthest

edge of the loaded part. Second, the assumed non-linear elastic behavior of the material is a reasonable approximation in shape and magnitude to the real material's load response. Also note that the J integral approach can be reduced to the Griffith theory for linear-elastic behavior (Rice, 1968). This method can measure the ductile material with plastic deformation. Therefore, it can be used in this study to measure the fracture energy of adhesive layer.

1.4 Application of CZM in Adhesive Joint

Encouraged by these two achievements, intensive studies have been conducted to investigate the nonlinear fracture behaviors of adhesively bonded joints in the past three decades. The1990s might be the most rapidly developing period of CZMs. The realistic demands for nonlinear simulation become urgent due to the wide applications of modern toughened adhesive. With such a situation, the classical LEFM, which is basically a single-parameter method, may have difficulties of meeting the increased demands in the accurate fracture simulations and predictions. Instead of the single-parameter model in LEFM, it has been reported that two or even three parameters were needed in CZMs for the sake of accurate modeling. For instance, these constitutive parameters could be chosen as the fracture toughness J_{IC}/J_{IIC}, the cohesive strength σ_{max}/τ_{max} and/or the characteristic length δ at which the cohesive tractions vanish (Wei and Hutchinson 1998; Williams and Hadavinia 2002; Ouyang and Li 2009a).

Various cohesive zone models (cohesive laws) were proposed to model the fracture process (Hillerborg et al. 1976; Rose et al. 1983; Needleman 1987; Tvergaard 1990; Xu and Needleman 1993; Camacho and Ortiz 1996). The main difference between these models lies in the shape of the traction-displacement response, and the parameters

used to describe that shape. All of them start from the assumption that one or more interfaces can be defined, where crack propagation is allowed by the introduction of a possible discontinuity in the displacement field. One feature of CZMs is that they can be conveniently incorporated in the traditional finite element analysis (FEA) to model the fracture behaviors in various materials and structures, including adhesive joints (Hillerborg et al. 1976; Needleman 1987; Tvergaard 1990; Tvergaard and Hutchinson 1992; Xu and Needleman 1993; Corigliano 1993; Camacho and Ortiz 1996; Chowdhury and Narasimhan 2000; Yang et al. 2001a; Yang et al. 2001b; Alfano and Crisfield 2001; Andruet et al. 2001; Pardoena et al. 2005; Högberg 2006; Salomonsson and Andersson 2008; Parrinello et al. 2009; Yan and Shang 2009; Moura et al. 2009). It is worth noting that CZMs can be also incorporated in analytical models to derive the theoretical solutions for some types of specimens or structures with relatively simple geometries (Klarbring 1991; Williams and Hadavinia 2002; Blackman et al. 2003; Pan and Leung 2007; Ouyang and Li 2009a; Ouyang and Li, 2009b; Ouyang and Li 2009c; Ouyang and Li, 2009d; Lorenzis and Zavarise, 2009; Nguyen and Levy 2009).

Although CZM based methods showed considerable difference, parameters need calibrations by test data. Importantly, due to the effects of adhesive thickness on plastic dissipations, calibrations are highly preferred to be conducted with different thicknesses of adhesive layer. There might be two means for the parameter characterizations: global method and local method. For the global method, one may compare measured global loadings, deflections and toughnesses to those by numerical models embedded with the parameters to be calibrated, at different adhesive thicknesses. The global behaviors of bonded joints have been widely tested with different adhesive thicknesses (Kinloch and

Shaw 1981; Chai 1988; Chai 1995; Ikeda et al., 2000; Kafkalidis et al., 2000; Yan et al. 2001; Madhusudhana and Narasimhan 2002; Lee et al. 2004; Pardoena et al. 2005), to name a few. Their study clearly showed that the fracture energy varies with the thickness of the adhesive layer. On the contrary, fewer attentions have been paid to the local test on the interfacial traction-separation laws across the interlayer. However, this is also a quite important issue. First, it may provide direct thickness-dependent equivalent interfacial laws for simple models. Meanwhile, it can cross-calibrate the parameters required by the "CZM+elastoplastic continuum" model. One may argue that global tests are sufficiently good to calibrate the parameters. It is believed that the local separation between the two adherends may be even a more direct, rigorous and reliable means to calibrate the parameters in a numerical model.

Several local experimental tests have been conducted on the local interfacial traction-separation laws for bonded joints. For instance, Sørensen (2002) and Andersson and Stigh (2004) experimentally determined the interfacial traction-separation laws of bonded joint under Mode-I loadings. Andersson et al. (2005) and Leffler et al. (2007) experimentally obtained the interfacial traction-separation law of bonded joint under Mode-II loadings. Recently, interfacial traction-separation laws were also tested under mixed mode loadings (Högberg et. al. 2007). Most recently, Liechti and Zhu (2009) conducted a local fracture test to extract the loading rate-dependent traction–separation laws.

The Mode II, or in-plane interface shear fracture, loading mode is also of particular importance for adhesive joints (Blackman et al., 2005). Mode II loading may be induced when a cracked adhesive joint or a layered composite is subjected to bending.

The various experimental fracture mechanics approaches to Mode II usually utilize some form of test specimen which is subjected to applied bending loads in order to determine the values of the Mode II toughness G_{IIC} (Carlsson et al., 1986).

To measure the Mode II interlaminar fracture toughness, Russell (1982) introduced the customary end notched flexure (ENF) test, a three-point bending test. The compliance in bending is measured at several positions of the crack front with respect to the loading pin, and the load for the crack growth is determined for one definite crack position. The critical interlaminar fracture toughness is computed using the linear elastic fracture mechanics (LEFM) combined with data reduction techniques.

One of the main problems that have been encountered with Mode II loading has been the poor reproducibility of the values of the measured Mode II toughness G_{IIC} (Davies et al., 1999). The experimental loading-unloading cycling test conducted by Russel and Street (1982) indicated a maximum error of around 2% in G_{IIC} in composites if friction was ignored. More recently, Davidson and Sun (2005) and Davidson et al. (2007) considered the effects of friction in the ENF specimen and 4-ENF tests were conducted on composites. They concluded that friction accounted for only about 2% and 5%, respectively, of the measured values of G_{IIC} from their tests. The effects of friction in the specimen could be a possible reason for this poor reproducibility.

Another possible major cause of scatter and inconsistency in Mode II toughness may be a difficulty in determining the location of the crack tip according to some recent studies (Schuecker and Davidson, 2000; Brunner, 2000; Brunner et al., 2006). The difficulty in determining the true crack length has also been observed during Mode I peel tests in composites when extensive fiber-bridging and microcracking occurs. This has

been shown to cause variations and errors in the calculation of toughness when corrected beam theory was employed (Brunner, 2000).

Additionally, numerous studies in the past several decades revealed an important experimental phenomenon: the global fracture behaviors are dependent on the loading modes (Tvergaard 1992, Kinloch 1981, Corigliano 1993, Chai 1995, Chowdhury 2000, and Hogberg 2006). For instance, the toughness of Mode-I is usually much less than that of Mode-II, while those of mixed modes are between them depending on mode mixities. Although there are still arguments regarding the mechanism of fracture mode dependence, one thing for sure is that the independent fracture tests under pure Mode-I and Mode-II loading conditions will facilitate the understanding of the mode dependent phenomenon by eliminating the coupling of stress and plastic dissipation.

Some local tests have been conducted to measure the critical CZM parameters. For instance, with *J*-integral based form, the local interfacial traction-separation laws were experimentally tested under pure Mode-I and pure Mode-II loading conditions (Soensen 2002, Andersson 2004, and Leffler 2007). It is noted that these studies focused on the interface fracture of bonded joints with identical adherends through standard fracture test methods (for instance, double cantilever beam (DCB) and end notched fracture (ENF)). Recently, an experimental study was also conducted to investigate the local mixed mode interfacial constitutive behaviors (Hogberg 2007). Most recently, Liechti and Zhu (2009) conducted a local fracture test to extract the loading-rate dependent traction–separation laws. These recent efforts on the local test of interfacial traction-separation and traction-slipping laws across the adhesive interlayer provided valuable information.

1.5 Effects of Adhesive Thickness

Interfacial laws became dependent on the geometries, such as thickness of the adherend and adhesive. Because they can affect the size of plastic zone and the magnitude of plastic strain, they change the equivalent interfacial traction-separation laws.

The adhesive layers are usually weaker than the adherends. Therefore, the adherends can be treated as rigid constraints on the adhesive layer. This means that the region where a crack can propagate is almost in a state of prescribed deformation (Andersson, 2006). During crack propagation, a zone where the adhesive is damaged precedes the crack tip. This zone is denoted as the damage zone. With a tough engineering adhesive, it is substantially longer than it appeared in a bulk test and typically several times larger than the thickness of the layer (Andersson, 2006). Thus, fracture behavior depends on the thickness of the adhesive layer. The fracture energy for a specific adhesive can reach a maximum value at a certain layer thickness (Kinloch, 1987 and Chai, 1988). Therefore, the effect of adhesive thickness is a very important parameter to design the safety factor of structure.

However, this parameter still lack of sufficient research and attention. These recent efforts on the local test of interfacial traction-separation laws across the adhesive interlayer provided valuable information. Most of them were conducted with a fixed thickness of adhesive layer (Sørensen (2002) tested two thicknesses). As discussed before, in order to more efficiently calibrate the parameters, the local traction-separation laws tests may be desired with different adhesive thicknesses. However, very few tests have been conducted on the thickness-dependent local interfacial traction-separation laws. Among the very few local tests regarding effects of adhesive thickness, Kafkalidis et al.

(2000) investigated the interfacial fracture by considering three different thicknesses of adhesive layer.

1.6 Research Objectives

The purpose of the present work is thus to conduct a systematic study on the effects of adhesive thickness and obtain an entire picture about its effects by using Double Cantilever Beam (DCB) test, End Notched Flexure (ENF) test, and Single Leg Bending (SLB) test with different thicknesses of adhesive layer. Not only its effects on the fracture energy, but also its effects on the local interfacial traction-separation laws are investigated.

In order to reduce the workload, the thickness of the adherend (steel and laminated composite) remains identical in this work. The thickness of steel and laminated composite adherends is designed to be relatively thick to prevent from any plastic deformation. Thus, all the nonlinear behaviors are limited in the adhesive interlayer. For the cases that plastic deformations are involved in the adherends, one may refer to the studies by Yang and Thouless as well as their co-workers (Yang et al. 2001a; Yang et al. 2001b). Both local and global test are conducted simultaneously. With these test results, the dependency of the interface strength and the shape of the constitutive laws on adhesive thickness can be revealed. The current test results may provide valuable test data for the research communities and facilitate the characterization of the parameters required by the CZM based numerical methods discussed before.

1.7 Outline and Organization of the Dissertation

This dissertation will include 7 chapters. Background, introduction of classical fracture mechanics, nonlinear fracture mechanics, application of CZM in adhesive joint,

and objectives will be discussed in Chapter 1, followed by Chapter 2 on theoretical background and Chapter 3 on the raw materials and test setup. The experimental results and discussions will be given in Chapter 4, Chapter 5, and Chapter 6 for Mode I, Mode II, and mixed Mode, respectively. The conclusion and future work will be presented in Chapter 7.

CHAPTER 2

THEORETICAL BACKGROUND

2.1 General

Current design approaches for predicting the fracture of adhesively-bonded materials are still somewhat empirical, and improving these approaches is a critical issue for furthering the engineering applications of this technology. Before the physical macro-crack is formed, these two surfaces are held together by traction within a cohesive zone. The interfacial stresses vary according to the relative displacement of the surfaces, and an interface cohesive law describes the activities in the cohesive zone in terms of the separation and the traction of the interface to be formed under the fracture process. The fracture process of most layered or bonded structures is commonly under the control of mixed mode cracking combined with mode I and mode II component. Under mixed mode cracking, the failure process zone is subjected to both normal (mode I) and shear stresses (mode II). In order to investigate the mixed mode interface fracture of bonded joints, pure Mode I and pure Mode II fracture will be studied, respectively.

This chapter focuses on developing a theoretical model which is able to characterize the nonlinear interface laws for pure Mode I, pure Mode II and mixed mode interface fracture test. With this developed model, the effects of adhesive thickness on global and local interface fracture behaviors can be revealed under different loading conditions.

In this theoretical model, it is assumed that the crack opens in a monotonic fashion; neither unloading nor crack closure is permitted and the cohesive (or bridging)

laws are assumed to be the same for each point along the bond length. Since the cohesive stresses represent the failure process zone, it may be also reasonable to assume that a certain crack opening exists, at which the cohesive stresses vanish when the failure criterion is satisfied. The classic beam theory is adapted for the adherends in adhesive joints. Meanwhile, it is assumed that the thickness of adhesive layer is very thin compared to that of the adherends. It is also assumed that the bond length is sufficiently long for all adhesively bonded joints.

2.2 Theoretical Derivations

Let's consider an infinitesimal section of two adherends bonded with a thin adhesive layer as shown in Fig. 2-1. It is noted that this infinitesimal section is located within the bonded length. With the classical beam theory, the displacements field of the two beams $U(x, z)$ and $W(x, z)$ have the form (each adherend is modeled by a beam),

$$U_1(x_1, z_1) = u_{10}(x) + z_1 \frac{dw_1(x)}{dx}; \qquad U_2(x, z_2) = u_{20}(x) + z_2 \frac{dw_2(x)}{dx} \tag{2-1}$$

$$W_1(x, z_1) = w_{10}(x); \qquad W_2(x, z_2) = w_{20}(x) \tag{2-2}$$

where subscripts i=1, 2 correspond to the upper and lower adherends, respectively; coordinate x and z correspond to longitudinal and vertical direction of adherends; u_{i0} represents the longitudinal displacements of the neutral axis in the adherends; $w_{i\,0}$ is the vertical displacements of the neutral axis in the adherends.

The longitudinal displacement of the bottom fiber of the upper beam u_1 and that of the top fiber of the bottom beam u_2 can be described as follows, respectively,

$$u_1 = u_{10} - \frac{h_1}{2}\frac{dw_1(x)}{dx}; \qquad u_2 = u_{20} + \frac{h_2}{2}\frac{dw_2(x)}{dx} \tag{2-3}$$

where w_1 represents the vertical displacement of the bottom fiber of the upper beam; and w_2 is the vertical displacement of the top fiber of the lower beam.

According to the classical beam theory, $w_1 = w_{10}$, and $w_2 = w_{20}$. Associated with Eq. (2-2), obviously, the normal interface separation w (normal relative displacement) between the bottom fiber of the upper adherend and top fiber of the lower adherend can be defined by

$$w = w_1 - w_2 \tag{2-4}$$

And,

$$\frac{dw}{dx} = \frac{dw_1}{dx} - \frac{dw_2}{dx} \tag{2-5}$$

According to Eq. (2-3), the relative tangential sliding δ (interface cohesive slip) between the upper adherend and lower adherend can be expressed by

$$\delta = u_1 - u_2 = (u_{10} - u_{20}) - (\frac{h_1}{2}\frac{dw_1}{dx} + \frac{h_2}{2}\frac{dw_2}{dx}) \tag{2-6}$$

The constitutive equations are written by

$$N_i = A_i \frac{du_{i0}}{dx}; \qquad M_i = D_i \frac{d^2 w_i}{dx^2} \tag{2-7}$$

in which

$$A_i = \frac{E_{xi} h_i}{1 - v_{zxi}^2}; \quad D_i = \frac{E_{xi} h_i^3}{12(1 - v_{zxi}^2)}$$

N_i and M_i are the axial force and bending moment *per unit width* of the beam i (i=1, 2), respectively; A_i and D_i are the axial and bending stiffness of the beam i (i=1, 2) *per unit width* under the plane strain condition.

The equilibrium equations of each beam *within the bonded region* are written in the conventional way as

$$\frac{dN_1}{dx} = \tau(x); \qquad \frac{dN_2}{dx} = -\tau(x) \tag{2-8}$$

$$\frac{dQ_1}{dx} = \sigma(x); \qquad \frac{dQ_2}{dx} = -\sigma(x) \tag{2-9}$$

$$\frac{dM_1}{dx} = Q_1 - \frac{h_1}{2}\tau(x); \qquad \frac{dM_2}{dx} = Q_2 - \frac{h_2}{2}\tau(x) \tag{2-10}$$

where $\sigma(x)$ and $\tau(x)$ are the interface normal and shear stress, respectively; N_1 and N_2 are the internal axial forces in beam 1 and 2, respectively; M_1 and M_2 are the internal bending moments in beam 1 and 2, respectively; Q_1 and Q_2 are the internal shear forces in beam 1 and 2, respectively (see Fig. 2.3.1).

The resultant forces and moment in the two beams are denoted as follows:

$$N_1 + N_1 = N_T; \quad Q_1 + Q_2 = Q_T; \quad M_1 + M_2 = M_T \tag{2-11}$$

By substituting Eq. (2-7) into the derivative of Eq. (2-6), it can be derived that

$$\delta' = -\frac{h_1}{2D_1}M_1 + \frac{N_1}{A_1} - (\frac{h_2}{2D_2}M_2 + \frac{N_2}{A_2}) \tag{2-12}$$

With Eq. (2-7) and note that w=w_1-w_2, we have follows:

$$w'' = w_1'' - w_2'' = (\frac{M_1}{D_1} - \frac{M_2}{D_2}) \tag{2-13}$$

$$w''' = w_1''' - w_2''' = (\frac{1}{D_1}\frac{dM_1}{dx} - \frac{1}{D_2}\frac{dM_2}{dx}) \tag{2-14}$$

With Eqs. (2-4) through (2-14), the following two equations can be derived that,

$$\delta'' + \frac{h_1 D_2 - h_2 D_1}{2(D_1 + D_2)} w''' + \frac{h_1 + h_2}{2(D_1 + D_2)} Q_T = [(\frac{1}{A_1} + \frac{1}{A_2}) + \frac{(h_1 + h_2)^2}{4(D_1 + D_2)}]\tau \tag{2-15}$$

$$\delta'' + (\frac{h_1}{2D_1} Q_1 + \frac{h_2}{2D_2} Q_2) = (\frac{h_1^2}{4D_1} + \frac{h_2^2}{4D_2} + \frac{1}{A_1} + \frac{1}{A_2}) \cdot \tau \tag{2-16}$$

By further taking the derivative of both sides of Eqs. (2-15) and (2-16), the follows can be derived, respectively,

$$\frac{h_1 D_2 - h_2 D_1}{2(D_1 + D_2)} w^{(4)} + \frac{h_1 + h_2}{2(D_1 + D_2)} \frac{dQ_T}{dx} = [(\frac{1}{A_1} + \frac{1}{A_2}) + \frac{(h_1 + h_2)^2}{4(D_1 + D_2)}]\tau' - \delta''' \tag{2-17}$$

$$(\frac{h_1}{2D_1} - \frac{h_2}{2D_2})\sigma = (\frac{h_1^2}{4D_1} + \frac{h_2^2}{4D_2} + \frac{1}{A_1} + \frac{1}{A_2}) \cdot \tau' - \delta''' \tag{2-18}$$

The resultant shear force Q_T=Q_1+Q_2 in the two adherends can be determined by global analysis with the given boundary conditions. For the sake of simplicity, in the current theoretical model, we only consider the conditions that Q_T is constant or piecewisely constant.

Therefore, the derivative of Q_T (or dQ_T/dx) in Eq. (2-17) becomes zero. The division of Eq. (2-17) by Eq. (2-18) gives

$$D_T \cdot \frac{d^4 w}{dx^4} = \frac{\xi_1 - \frac{\delta'''}{\tau'}}{\xi_2 - \frac{\delta'''}{\tau'}} \cdot \sigma(w) \tag{2-19}$$

where

$$D_T = \frac{D_2 D_1}{(D_1 + D_2)}; \quad \xi_1 = \frac{1}{A_1} + \frac{1}{A_2} + \frac{(h_1 + h_2)^2}{4(D_1 + D_2)}; \quad \xi_2 = \frac{h_1^2}{4D_1} + \frac{h_2^2}{4D_2} + \frac{1}{A_1} + \frac{1}{A_2} \tag{2-20}$$

2.3 Governing Equations

In this dissertation, two adherends materials: steel and glass fiber composites, are considered. However, the adherends in the adhesive joints have identical thickness, width and material, although the thickness of adhesive layer may vary.

Therefore, we have the follows for all conditions:

$$A_1 = A_2; \qquad h_1 = h_2; \qquad D_1 = D_2 \tag{2-21}$$

By substituting Eq. (2-21) into Eq. (2-20), it is not difficult to verify that

$$\xi_1 = \xi_2 \tag{2-22}$$

For the sake of clarify, we denote that

$$h_1 = h_2 = h; \quad A_1 = A_2 = A; \; D_1 = D_2 = D; \quad h_1/D_1 = h_2/D_2 = h/D \tag{2-23}$$

By inserting Eqs. (2-22) and (2-23) into Eq. (2-15), we have

$$\delta'' + \frac{h}{2D} Q_T = \tau \cdot \left[\frac{2}{A} + \frac{h^2}{2D} \right] \tag{2-24}$$

By substituting Eqs. (2-22) and (2-23) into Eq. (2-19), we obtain

$$\frac{D}{2} \cdot \frac{d^4 w}{dx^4} = \sigma(w) \tag{2-25}$$

It is worth noting that Eq. (2-24) represents the governing equation of interfacial shear behaviors, while Eq. (2-25) represents the governing equation of interfacial peel behaviors. It is also noted that if only: (i) the resultant shear force Q_T in the two adherends is a constant or piecewisely constant within the bonded length; and (ii) the two adherends are identical.

2.4 *J*- integral for Interface Shear Behaviors

Strictly, the adhesive material must be nonlinearly elastic during the test. However, for a monotonic loading process (no unloading occurs), the cohesive separation as well as plastic dissipation in the adhesive layer might still be considered by the well-known path independent integral or J-integral as follow (Rice 1968):

$$J = \int_{\Gamma} (Wdy - T\frac{\partial u}{\partial x} ds) \tag{2-26}$$

where $W(x, y)$ is the strain energy density; x and y are the coordinate directions, $T=\boldsymbol{n}\cdot\boldsymbol{\sigma}$ is the traction vector; $\boldsymbol{n}$ is the normal to the curve or path Γ, $\boldsymbol{\sigma}$ is the Cauchy stress, and $\boldsymbol{u}$ is the displacement vector.

Let us consider an arbitrary tangential cohesive law $\tau=\tau(\delta)$. Note $Q_1+Q_2=Q_T$ is a constant along the x coordinate. Let us integrate both sides of the governing Eq. (2-24) as follow:

$$\int \delta'' d\delta + \frac{h}{2D}\cdot\int Q_T d\delta = \left[\frac{2}{A} + \frac{h^2}{2D}\right]\cdot\int \tau(\delta) d\delta \tag{2-27}$$

Eq. (2-27), which is the equivalent integral form, can be rewritten by

$$\int (\frac{\partial \delta'}{\partial \delta}\delta') d\delta + \frac{h}{2D}\cdot Q_T \int d\delta = \left[\frac{2}{A} + \frac{h^2}{2D}\right]\cdot\int \tau(\delta) d\delta \tag{2-28}$$

By integrating δ' with respect to δ from 0 to δ, it can be derived that,

$$\frac{1}{2}[(\delta')^2-(\delta'_m)^2]+\frac{h}{2D}\cdot Q_T\cdot(\delta-\delta_m)=\left[\frac{2}{A}+\frac{h^2}{2D}\right]\cdot\int_{\delta_m}^{\delta}\tau(\delta)d\delta \tag{2-29}$$

where δ'_m represents the derivative of δ=0, and δ_m represents the value of δ when $d\delta/dx$=0.

It should be noticed that the integral limits on both sides of Eq. (2-29) must be corresponded to each other. However, when the joint's overlap length and the length between the support and concentrated middle load are sufficiently long relative to the cohesive zone, we may approximate the solution with $\delta_m \to 0$ and $\delta'_m \to 0$.

Therefore, for the specimens with sufficiently long bond length, by denoting the tangential cohesive slip at the crack tip by δ_0, Eq. (2-29) can be reduced to,

$$\frac{1}{2}(\delta'_0)^2+\frac{h}{2D}\cdot Q_T\cdot\delta_0=\left[\frac{2}{A}+\frac{h^2}{2D}\right]\cdot\int_0^{\delta_0}\tau(\delta)d\delta \tag{2-30}$$

Consequently, the mode II energy release rate J_{II} can be written by

$$J_{II}(\delta_0)=\int_0^{\delta_0}\tau(\delta)d\delta=\frac{\frac{1}{2}(\delta'_0)^2+\frac{h}{2D}\cdot Q_T\cdot\delta_0}{\frac{2}{A}+\frac{h^2}{2D}} \tag{2-31}$$

The value of δ'_0 at the crack tip can be readily determined as a function of the external forces, bending moments through global analysis as described by Eq. (2-12). In other words, once the crack tip slip δ_0 is experimentally measured, the mode II energy release rate J_{II} is then determined.

2.5 *J*- integral for Interface Peel Behaviors

Similar to the discussion in interface tangential behavior, let us consider an arbitrary normal cohesive law $\sigma=\sigma(w)$. It can be observed that the governing Eq. (2-25) is equivalent to the equation as

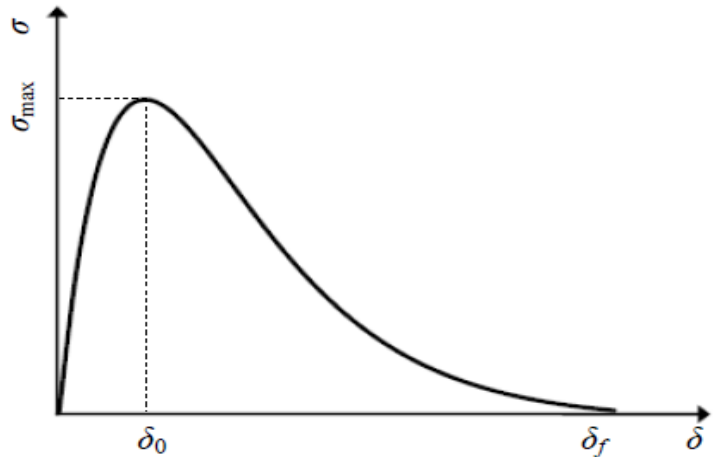

Figure 2.1.1: A typical nonlinear interfacial traction-separation law

f ollow,

$$\frac{d^3w}{dx^3}\cdot\frac{dw}{dx}-\frac{1}{2}\left(\frac{d^2w}{dx^2}\right)^2+\frac{2}{D}\cdot\int_0^w\sigma(w)dw=0 \qquad (2\text{-}32)$$

One may verify the equivalence between Eqs. (2-25) and (2-32) by taking derivative of Eq. (2-32) with respect to x and then comparing it to Eq. (2-25).

Let us denote the beam's rotations by θ_i (i=1, 2) for adherend 1 and adherend 2, respectively. The relative crack tip rotation between the two beam is denoted by $\theta_0=\theta_{10}-\theta_{20}$. Meanwhile, the crack tip normal opening is correspondingly denoted by w_0. Obviously, the crack tip ***relative rotation*** $\theta_0=-dw_0/dx$. Simultaneously, by expressing d^2w_0/dx^2 and $dw_0{}^3/dx^3$ in terms of the bending moments and the shear forces at the crack tip, one may see that

$$J_I = \int_0^{w_0} \sigma(w)dw = \frac{1}{2} \cdot \frac{D_1 D_2}{D_1 + D_2}[\frac{M_1}{D_1} - \frac{M_2}{D_2}]^2 + \frac{D_1 D_2}{D_1 + D_2}(\frac{P_1}{D_1} - \frac{P_2}{D_2})\theta_0 \quad (2\text{-}33)$$

Since D_1=D_2=D, we may further obtain

$$J_I = \int_0^{w_0} \sigma(w)dw = \frac{1}{4D}[M_1 - M_2]^2 + \frac{1}{2}(P_1 - P_2)\theta_0 \quad (2\text{-}34)$$

2.6 Determination of Interface Cohesive Laws

It is important to note that the interfacial separation w and δ represent the normal opening and tangential slip between the bottom fiber of the upper adherend and the top fiber of the lower adherend. A typical nonlinear equivalent cohesive law is shown in Fig. 2.1.2. For most CZMs in the literature, the traction-separation laws are such that with increasing interfacial separation, the traction across the interface reaches a maximum, then decreases and eventually vanishes. This typical nonlinear separation-traction law has three segments: (a) elastic stage when the normal interfacial separation $\delta \leq \delta_0$. The normal interfacial stress σ increases with separation until the maximum interfacial stress $\sigma_{\max}$ (interfacial strength) is reached; (b) softening stage when $\delta_0 \leq \delta \leq \delta_f$. The normal traction σ decreases with separation δ; and (c) complete debonding stage. There is no interfacial stress when $\delta \geq \delta_f$. By conducting the fracture tests with different adhesive thicknesses, the effects of adhesive layer on the constitutive laws, such as the interfacial strength, shape of the interfacial traction-separation law, and fracture energy can be revealed.

$$\sigma(w) = \frac{\partial J_I(w)}{\partial w} = \frac{\partial\left\{\frac{1}{4D}[M_1 - M_2]^2 + \frac{1}{2}(P_1 - P_2)\theta_0\right\}}{\partial w} \quad (2\text{-}35)$$

$$\tau(\delta) = \frac{\partial J_{II}(\delta)}{\partial \delta} = \frac{\partial \left\{ \dfrac{\frac{1}{2}(\delta_0')^2 + \frac{h}{2D} \cdot Q_T \cdot \delta_0}{\frac{2}{A} + \frac{h^2}{2D}} \right\}}{\partial \delta} \tag{2-36}$$

We shall discuss more details regarding how to measure the cohesive laws in the next chapter. Meanwhile, it is noted that this interface constitutive relationship is the equivalent interface cohesive law, not necessarily the intrinsic cohesive law. This is because in addition to the intrinsic cohesive separation, possible plastic deformations in the adhesive layer contribute to the entire separation between the two adherends during the fracture test.

2.7 Fracture Tests by DCB, ENF and SLB Specimens

By this point, the general theoretical models have been derived for the interface peel behavior or normal separation (Mode-I fracture) and the interface shear behavior or tangential slip (Mode-II fracture). It is worth noting that the derived model can be also applied to the in-plane mixed mode fracture (Mode I/II fracture) only if the two adherends are identical.

However, as mentioned before, the specific formula might be different for different fracture test configurations due to the different boundary conditions. Therefore, in the work, three common standard fracture test methods: double cantilever beam (DCB), end notched flexure (ENF) and single leg bending (SLB) are adopted for Mode-I, Mode-II and in-plane mixed Mode I/II, respectively.

2.7.1 DCB Specimens for Mode-I Fracture Test

DCB specimens have been widely adopted to investigate the pure Mode-I interface fracture of bonded joints in previous studies (Ouyang 2009a, Tvergaard 1996, Xu 1993, Camacho 1996, Chowdhury 2000, Madhusudhana 2002, Pardoena 2005, Li 2005, Kinloch 1981, Chai 1995, Ikeda 2000, Kafkalidis 2000, Yan 2001, Soensen 2002, and Andesson 2004).

Consider a typical double cantilever beam (DCB) specimen as shown in Fig. 2.1.1. It is assumed that the adherends are linearly elastic during the entire fracture test process. A thin adhesive layer is used to bond the two adherends.

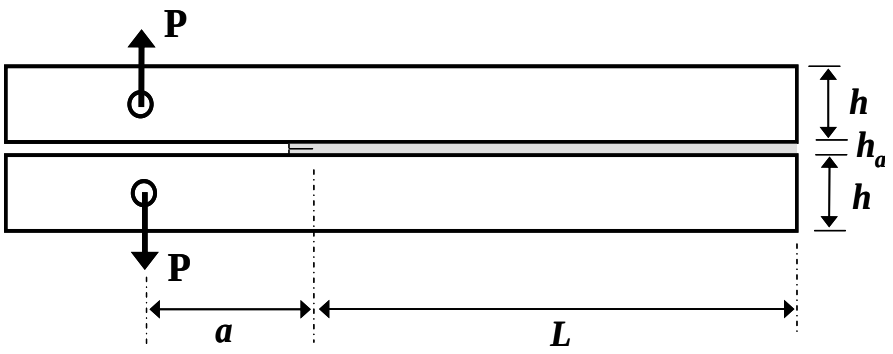

Figure 2.1.2: Schematic of DCB test specimen

Obviously, with the DCB configuration, the bending moments M_1 and M_2 at the cross section of crack tip are $M_1=Pa$ and $M_2= -Pa$, respectively (note $P_1=-P_2=P$). Note the relationship between the relative rotation and each beam's rotation at the crack tip is $\theta_0=2\theta_{10}=-2\theta_{20}$. Therefore, Eq. (2-34) can be rewritten for DCB specimen as follow:

$$J_I = \int_0^{w_0} \sigma(w)dw = \frac{P^2a^2}{D} + 2P\theta_{10} \tag{2-37}$$

Further rewriting Eq. (2-37) as follow:

$$J_{\mathrm{I}} = \int_0^{w_0} \sigma(w)dw = 2P \cdot [\frac{Pa^2}{2D} + \theta_{10}] \tag{2-38}$$

The first term ($Pa^2/2D$) in the bracket reflect the variation of rotation in each beam, the sum in the bracket can be replaced as follow:

$$\frac{Pa^2}{2D} + \theta_{10} = \theta_{1P} \tag{2-39}$$

where $\theta_{1\mathrm{P}}$ is the upper beam's rotation at the cross section of loadline. In addition, we may denote the lower beam's rotation at the cross section of loadline by $\theta_{2\mathrm{P}}$. One may readily see that $\theta_{1\mathrm{P}} = -\theta_{2\mathrm{P}}$. We further introduce a concept: ***relative rotation*** $\boldsymbol{\theta_{\mathrm{P}}}$, which reflects the relative rotation between the two beams at the cross section of loadline.

Obviously, for the DCB specimen, one can see

$$\theta_P = 2\theta_{1P} = -2\theta_{2P} \tag{2-40}$$

Finally, with Eq. (2-38) through (2-40), we have

$$J_{\mathrm{I}}(w_0) = \int_0^{w_0} \sigma(w)dw = P \cdot \theta_P \tag{2-41}$$

Eq. (2-41) indicates that the energy release J_{I} for pure Mode-I fracture of DCB specimen equals the product of peel force P and relative rotation θ_{P} between the two beams at the loadline.

According to Eq. (2-35), the interfacial normal stress σ of DCB specimen (at the crack tip) can be determined as follow:

$$\sigma(w) = \frac{\partial J_{\mathrm{I}}(w_0)}{\partial w_0} = \frac{\partial\{P \cdot \theta_P\}}{\partial w_0} \tag{2-42}$$

Eq. (2-42) indicates that once the crack tip opening w_0 and J_I are simultaneously measured (or J_I-w_0 curve is measured), the interface normal stress σ is experimentally determined.

2.7.2 ENF Specimens for Mode-II Fracture Test

End notched flexure (ENF) specimens have been widely applied to investigate the pure Mode-II interface fracture of bonded joints (Andersson and Stigh 2004; Ouyang and Li 2009b).

Consider a typical end notched flexure (ENF) specimen as shown in Fig. 2.1.2. It is assumed that the adherends are linearly elastic during the entire fracture test process. A thin adhesive layer is used to bond the two adherends.

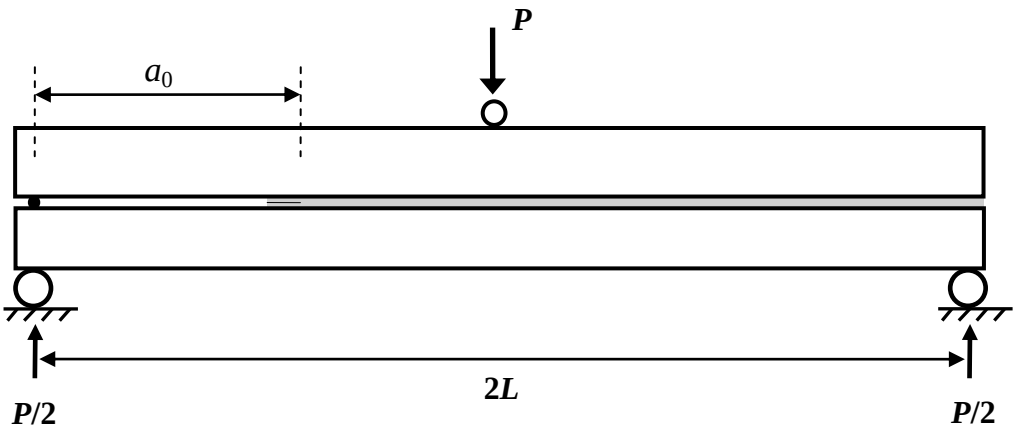

Fig. 2.1.3: Schematic of ENF specimen test

Obviously, with the ENF configuration, the resultant shear force Q_T in the section from left support to the mid-span loading P is a constant. Let's assume that the shear forces in the upper and lower beam at the cross section of crack tip are Q_1 and Q_2, respectively. Evidently, Q_1 and Q_2 will not vary within the region from the left support to the cross section of crack tip.

Since the axial forces N_1=N_2=0 at the cross section of crack tip, with Eq. (2-12), h_1/D_1=h_2/D_2=h/D, the parameter δ_0' in Eq. (2-31) can be expressed for ENF specimens as follow:

$$\delta' = -\frac{h}{2D}(M_1 + M_2) = -\frac{h}{2D}M_T \tag{2-43}$$

Note that the resultant M_T at the cross section of crack tip is $M_T = M_1 + M_2 = Q_T \cdot a$ (Q_T is also equal to the support reaction force, and Q_T=P/2). Associated with Eq. (2-31), the energy release rate J_{II} of ENF specimen can be expressed by,

$$J_{II}(\delta_0) = \int_0^{\delta_0} \tau(\delta) d\delta = \frac{\frac{1}{2}(\frac{ha}{2D}\cdot\frac{P}{2})^2 + \frac{h}{2D}\cdot\frac{P}{2}\cdot\delta_0}{\frac{2}{A} + \frac{h^2}{2D}} \tag{2-44}$$

According to Eq. (2-36), the interfacial shear stress τ of ENF specimen (at the crack tip) can be determined as follow:

$$\tau(\delta) = \frac{\partial J_{II}(\delta_0)}{\partial \delta_0} = \frac{\partial\left\{\frac{\frac{1}{2}(\frac{ha}{2D}\cdot\frac{P}{2})^2 + \frac{h}{2D}\cdot\frac{P}{2}\cdot\delta_0}{\frac{2}{A} + \frac{h^2}{2D}}\right\}}{\partial \delta_0} \tag{2-45}$$

Eq. (2-45) indicates that once the crack tip slip δ_0 and J_{II} are simultaneously measured (or J_{II}-δ_0 curve is measured), the interface shear stress τ (δ_0) is experimentally determined.

2.7.3 SLB Specimens for Mixed Mode I/II Fracture Test

Single leg bending (SLB) specimens have been widely applied to investigate the in-plane mixed Mode I/II interface fracture of bonded joints in previous studies. Let's

consider a typical SLB specimen as shown in Fig. 2.1.3. It is noted that for the SLB specimen, both Mode-I fracture component and Mode-II fracture component exist. Therefore, we will give the formula for J_{I} and J_{II}, as well as the corresponding formula for interface normal stress σ and shear stress τ, separately.

Note for the SLB specimen, the resultant M_{T} at the cross section of crack tip is still $M_T = M_1 + M_2 = Q_T \cdot a = Pa/2$ (Q_{T} is still equal to the support reaction force, and Q_{T}=P/2); although $M_1 = Pa/2$ and M_2=0, respectively. With the same argument as in section 2.7.2, the energy release rate component J_{II} of SLB specimen can be expressed by,

$$J_{\mathrm{II}}(\delta_0) = \int_0^{\delta_0} \tau(\delta) d\delta = \frac{\frac{1}{2}\left(\frac{ha}{2D} \cdot \frac{P}{2}\right)^2 + \frac{h}{2D} \cdot \frac{P}{2} \cdot \delta_0}{\frac{2}{A} + \frac{h^2}{2D}} \tag{2-46}$$

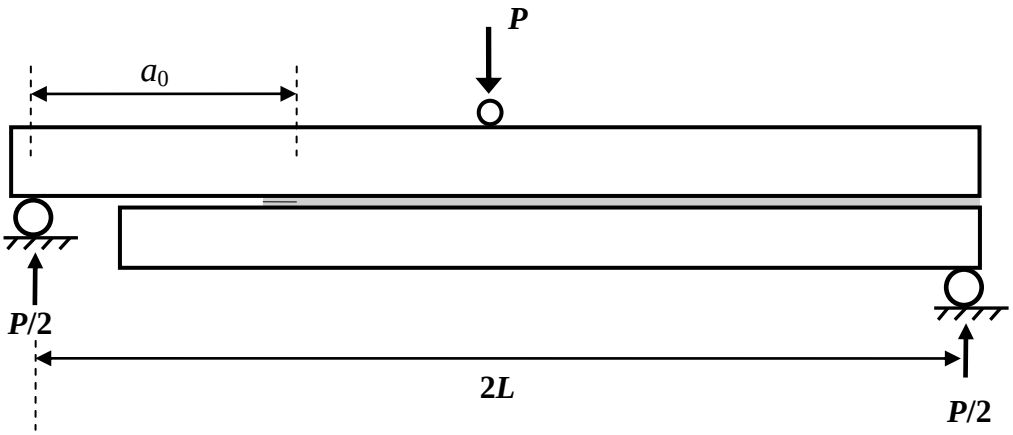

Fig. 2.1.4: Schematic of SLB specimen test

Similarly, the interfacial shear stress $\tau(\delta_0)$ of SLB specimen (at the crack tip) can be determined as follow:

$$\tau(\delta)=\frac{\partial J_{\text{II}}(\delta_0)}{\partial\delta_0}=\frac{\partial\left\{\dfrac{\frac{1}{2}(\frac{ha}{2D}\cdot\frac{P}{2})^2+\frac{h}{2D}\cdot\frac{P}{2}\cdot\delta_0}{\frac{2}{A}+\frac{h^2}{2D}}\right\}}{\partial\delta_0} \tag{2-47}$$

In order to determine the energy release rate component J_{I} of SLB specimen, let's recall Eq. (2-34). Meanwhile, for SLB specimen, $M_1=Q_T\cdot a=Pa/2$, M_2=0; P_1=Q_{T}=P/2, P_2=0. Therefore, Eq. (2-34) can be rewritten by

$$J_{\text{I}}=\int_0^{w_0}\sigma(w)dw=\frac{1}{4D}[Q_T a]^2+\frac{1}{2}(Q_T)\theta_0 \tag{2-48}$$

With the similar approach in section 2.7.1, and note that the lower beam's rotation at the crack tip is equal to that at the loadline (θ_{20}=$\theta_{2\text{P}}$) since there are no bending moment in the lower beam within the region from left support to the crack tip. Thus the Mode-I energy release rate component J_{I} can be expressed as follow:

$$\begin{aligned}J_{\text{I}}&=\frac{Q_T}{2}\cdot[\frac{Q_T a^2}{2D}+\theta_0]=\frac{Q_T}{2}\cdot[\frac{Q_T a^2}{2D}+\theta_{10}-\theta_{20}]\\&=\frac{Q_T}{2}\cdot[\frac{Q_T a^2}{2D}+\theta_{10}-\theta_{2P}]=\frac{Q_T}{2}\cdot[\theta_{1P}-\theta_{2P}]\\&=\frac{Q_T}{2}\cdot\theta_P\end{aligned} \tag{2-49}$$

where θ_{P} is the relative rotation between the two beams at the loadline. It is worth noting that in a real experimental SLB, it is not convenient to measure the rotation of lower beam's rotation at the loadline due to the presence of the support, neither that at the crack tip. However, one may simply choose location between crack tip and support where is more convenient, since the lower beam's rotations within this region are identical.

Since P=2Q_{T}, with Eq. (2-49), Mode-I energy release rate component J_{I} can be expressed as follow:

$$J_{\mathrm{I}} = \int_0^{w_0} \sigma(w)dw = \frac{P}{4} \cdot \theta_P \tag{2-50}$$

According to Eq. (2-35), the interfacial normal stress σ of SLB specimen (at the crack tip) can be determined as follow:

$$\sigma(w) = \frac{\partial J_{\mathrm{I}}(w_0)}{\partial w_0} = \frac{\partial\left\{\frac{1}{4}P \cdot \theta_P\right\}}{\partial w_0} \tag{2-51}$$

Eqs. (2-46), (2-47), (2-50) and (2-51) indicate that once the crack tip slip δ_0, loading force P, and the rotation of the two adherends are simultaneously recorded, J_{I} and J_{II} can be calculated (or J_{I}-w_0 and J_{II}-δ_0 curves can be obtained). Then, the interface shear stress τ (δ_0) and interface normal stress σ (w_0) can be experimentally determined, simultaneously.

CHAPTER 3

EXPERIMENTAL METHOD

3.1 Raw Material

3.1.1 Adhesive Material

The adhesive, LOCTITE Hysol 9460, is a modified structural epoxy adhesive. This material has high peel strength, good impact resistance, and good fatigue resistance. The mix ratio of resin and hardener is 1:1 by weight. According to the manufacturer, its elastic modulus, tensile strength and elongation are 2.76 GPa, 30.3 MPa and 3.5%, respectively. The glass transition temperature is 68^{o}C.

3.1.2 Adherends Material

- **Metal Adherends**

General purpose 1018 low carbon steel bars with yield strength of 372.3 MPa with elastic modulus 209 GPa were used to fabricate metal based adherends of Double Cantilever Beam (DCB), End Notched Flexure (ENF), and Single Leg Bending (SLB) specimens. Before the adhesive was applied, the surface of the adherends were grounded by sand paper, and then cleaned by using acetone.

- **Composite Adherends**

Continuous glass woven fabric reinforced polymer laminate were used to fabricate the laminated composite based adherends of DCB, ENF, and SLB specimens. The mechanical parameters were given in Table 3.1.1. The adherend was made of layers of glass cloth (0^{o} and 90^{o} crossply) with epoxy resin. Before the adhesive was applied, the surface of the adherends were experienced sanding and cleaning processes.

Table 3.1.1 mechanical parameters of laminated composite

E_1 (GPa)	E_2 (GPa)	E_3 (GPa)	G_{12} (GPa)
18.61	15.17	0.46	7.38

3.2 Fabrication of Specimen

There are two different methods to manufacture the DCBs. One is that the adherends are cut before the adhesive curing processes. The other one is that the two adherends with adhesive experience the curing processes and then are cut to small DCB specimens. The major problem of this method is that during the milling and cutting processes, the adhesive layer could be damaged by metal chips. Therefore, this study cut the adherends before bonding them with adhesive.

The thickness of the adherends was measured before the adhesive was applied and compared with the thickness of the specimen after curing. In order to obtain different and desirable thickness of the adhesive layer, six different thickness feeler gage inserts were inserted in between the two adherends. The feeler gages can also control the edge of the adhesive and help in keeping the adherends parallel. It is also noted that the surface of the feeler gauges were sprayed with a super-thin layer of mold release agent so that the feeler gauges could be easily removed after the curing.

A very thin mylar tape with thickness of 0.035 mm was carefully inserted from the edge of adhesive layer by 2 mm at the middle height of the adhesive layer immediately after the application of the adhesive layer to create a sharp initial crack, as shown in Fig.3.2.1.

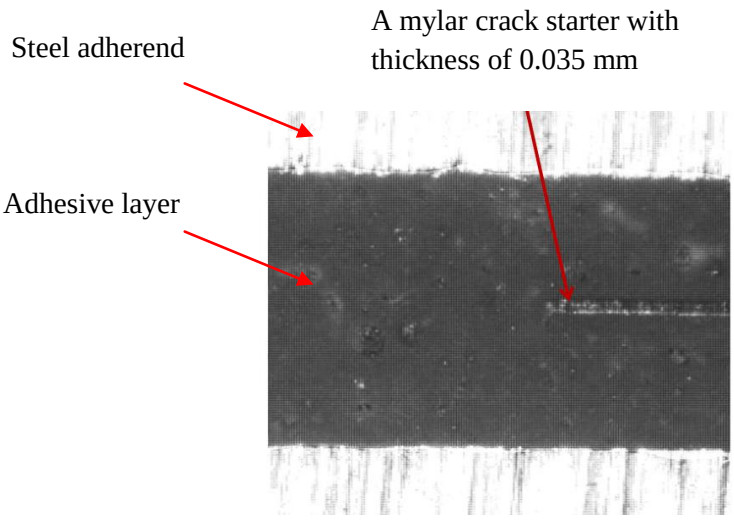

Figure 3.2.1: microscope image shows the inserted 0.035 mm thick mylar sheet located at the middle plane of the adhesive layer

The prepared specimens were then pressed by the same weights and cured for 24 hours at room temperature. The specimens were further put into an oven at 60.5^{o}C (141^{o}F) for 1 hour for post-curing. After that, they were cooled down to room temperature before test.

3.2.1 Steel Based DCB Specimen for Mode I Test

The actual average adhesive thicknesses of the six groups of specimens were 0.09 mm, 0.2 mm, 0.4 mm, 0.6 mm, 0.8 mm, and 1.0 mm. After cutting, a hole (11.11mm in diameter), which was 50.8 mm from one end of the adherend, was drilled coaxially in the upper and lower adherends and coaxially machined threads inside the hole to apply the peel load using our specially designed loading fixture as will be discussed later. Once the surface of the adherends was cleaned by using acetone, the adherends were ready for preparing the DCB specimens, as shown in Fig.3.2.2.

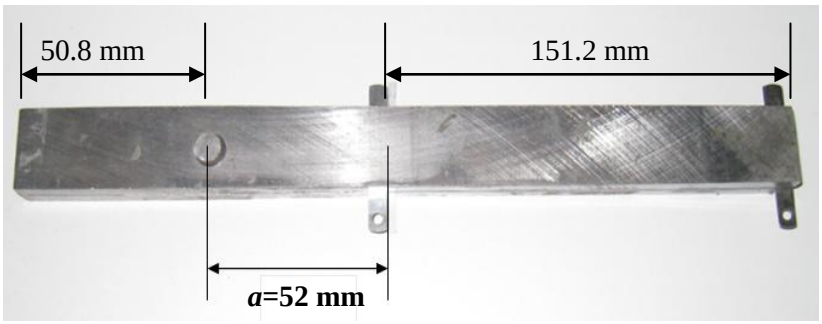

Figure 3.2.2: DCB specimen bonded with polished/cleaned adherends and uniform thickness of adhesive layer through standard feeler gauge

Table 3.2.1 Geometry of steel based adherends of specimens in mode I test:

Group Number	Average adhesive thickness (mm)	Length (mm)	Height (mm)	Width (mm)	Initial Crack Length (mm)
1	0.09	254.10	6.44	25.41	52.12
2	0.2	254.11	6.55	25.44	52.22
3	0.4	254.09	6.75	25.42	52.18
4	0.6	254.08	6.95	25.39	52.44
5	0.8	254.10	7.15	25.46	52.37
6	1.0	254.08	7.35	25.37	52.11

Since the distance between the loadline and the edge of the adhesive layer is 50 mm, the total initial crack length "*a*" is 52mm. The geometry information of each group of specimens was given in Table 3.2.1. After the adhesive was applied, a steel pin with the same diameter as the threaded hole was inserted into the hole to hold the adherends in place.

3.2.2 Laminated Composite Based DCB Specimen for Mode I Test

Continuous glass woven fabric reinforced polymer laminate were used to fabricate the 3.1mm thick, 25.4mm wide and 304.8 mm long adherends of DCB specimens. The adherend was made of 17 layers of glass cloth (0^o and 90^o crossply) with epoxy resin. Totally, five groups of specimens were prepared with the actual average adhesive thicknesses of 0.1 mm, 0.2 mm, 0.4 mm, 0.6 mm, and 0.8 mm (numbered by

group 1 through group 5, respectively). The geometry of specimens was given in Table 3.2.2. A hole was drilled in each of two pieces of tool-grade steel blocks. These two steel blocks were sanded, polished and then carefully bonded on the surface of the composite laminates at one end of the specimen by super glue, as shown in Fig.3.2.3.

Table 3.2.2 Geometry of laminated composite based adherends of specimens in mode I test:

Group Number	Average adhesive thickness (mm)	Length (mm)	Height (mm)	Width (mm)	Initial Crack Length (mm)
1	0.1	304.11	6.32	25.41	50.81
2	0.2	304.12	6.42	25.44	50.81
3	0.4	304.07	6.62	25.42	50.82
4	0.6	304.09	6.82	25.39	50.82
5	0.8	304.10	7.02	25.46	50.80

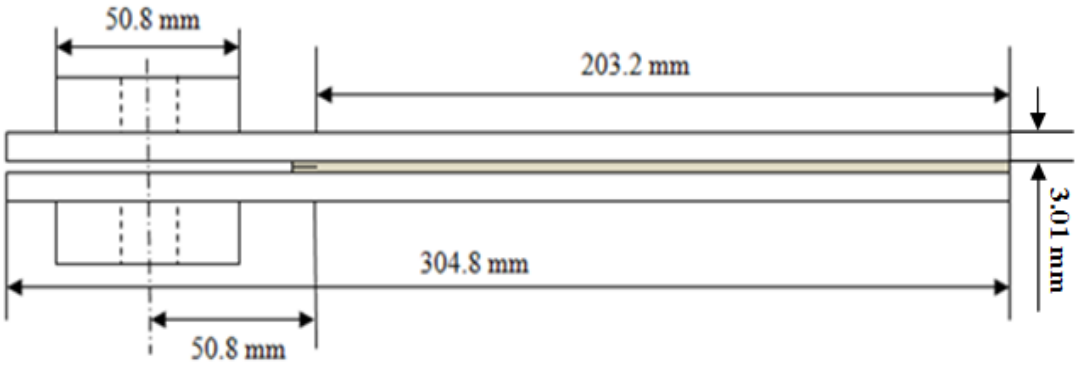

Figure 3.2.3: DCB specimen bonded with polished/cleaned adherends and uniform thickness of adhesive layer and two steel loading blocks.

3.2.3 Steel Based ENF Specimen for Mode II Test

In the current study, low carbon steel bar were used to fabricate the 9.5mm thick, 25.4mm wide and 609.6 mm long adherends of ENF specimens, as shown in Fig.3.2.4. A total of five groups of specimens were numbered from group 1 to group 5 for the average adhesive thicknesses of 0.1 mm, 0.2mm, 0.4mm, 0.6mm, and 0.8mm, respectively. Each group had 3 effective specimens, and a total of 15 effective specimens were fabricated. The specimen geometries were given by Table 3.2.3.

Table 3.2.3 Geometry of steel based adherends of specimens in mode II test

Group Number	Average adhesive thickness (mm)	Length (mm)	Height (mm)	Width (mm)	Initial Crack Length (mm)
1	0.1	609.61	19.16	25.41	103.62
2	0.2	609.66	19.26	25.44	103.11
3	0.4	609.62	19.46	25.42	103.35
4	0.6	609.66	19.66	25.39	103.56
5	0.8	609.65	19.86	25.46	103.19

After curing, the wire shape feeler gages with relevant thickness were inserted to the end of the specimen. Therefore, during the three-point bending test, the upper and lower adherends can rotate with the same angle.

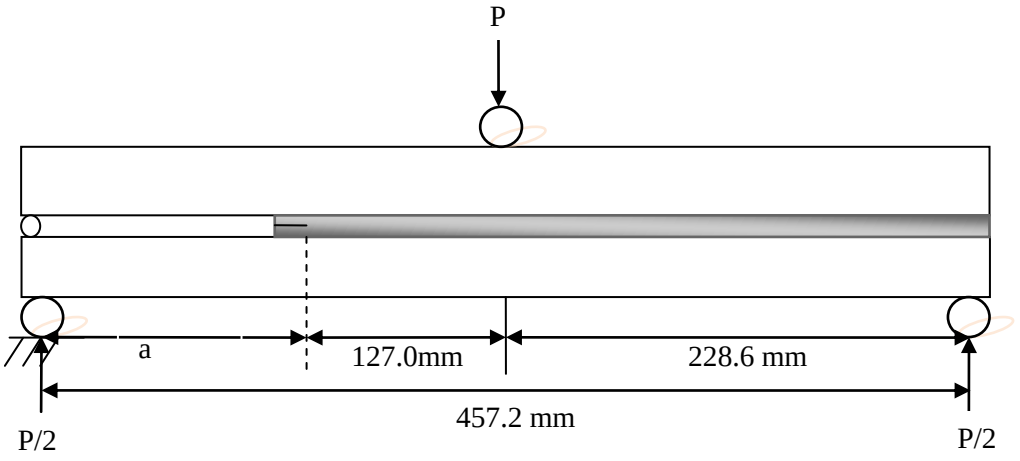

Figure 3.2.4: Schematic of steel based adherends of ENF specimen

3.2.4 Laminated Composite Based ENF Specimen for Mode II Test

Continuous glass woven fabric reinforced polymer laminate were used to fabricate the 6.35mm thick, 25.4mm wide and 304.0 mm long adherends of ENF specimens, as shown in Fig.3.2.5. The adherend was made of 35 layers of glass cloth (0^o and 90^o crossply) with epoxy resin. In the current study, a total of five groups of specimens were numbered from group 1 to group 5 for the average adhesive thicknesses

of 0.1 mm, 0.2mm, 0.4mm, 0.6mm, and 0.8mm, respectively. Each group had 3 effective specimens, and a total of 15 effective ENF specimens were prepared. The average of specimen geometries was given by Table 3.2.4. Specimens

Table 3.2.4 Geometry of Composite based adherends of specimens in mode II test

Group Number	Average adhesive thickness (mm)	Length (mm)	Height (mm)	Width (mm)	Initial Crack Length (mm)
1	0.1	304.8	6.35	25.41	88.91
2	0.2	304.8	6.35	25.44	88.93
3	0.4	304.8	6.35	25.42	88.88
4	0.6	304.8	6.35	25.39	88.89
5	0.8	304.8	6.35	25.46	88.92

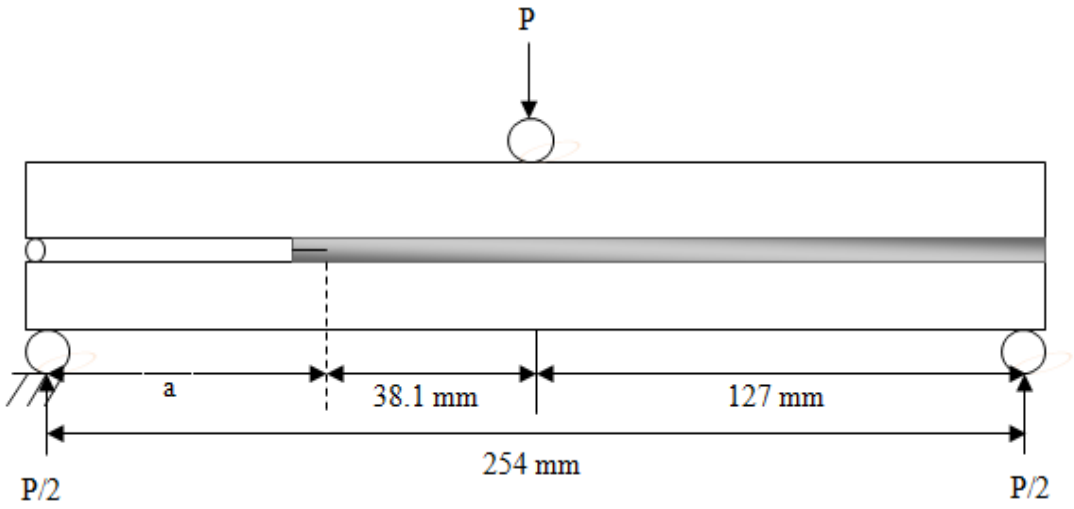

Figure 3.2.5: Schematic of composite based adherends of ENF specimen

3.2.5 Steel and Laminated Composite Based Single Leg Bending Specimen for Mixed Mode I/II Test

In the current study, steel based adherends has the same geometry as laminated composite based adherends. A total of five groups of specimens were numbered from ha=0.1mm to ha=0.8mm with the average adhesive thicknesses of 0.1 mm, 0.2mm,

0.4mm, 0.6mm, and 0.8mm, respectively. In order to consider the effect of the initial crack length, three initial crack length were selected from a=20mm, 50mm, and 80mm. Specimen design was shown in Fig.3.2.6.

For each different initial crack length, 5 groups of specimens were prepared. Each group had 3 effective specimens, and a total of 45 effective steel based specimens and a total of 45 effective laminated composite based specimens were fabricated, geometry of SLB specimens was provided in Table 3.2.5.

Table 3.2.5 Geometry of SLB specimens in Mixed Mode I/II test

Average adhesive thickness (mm)	Length (mm)	Height (mm)	Width (mm)	Initial Crack Length (mm)	Initial Crack Length (mm)	Initial Crack Length (mm)
0.1	254.0	12.80	25.4	20.0	50.0	80.0
0.2	254.0	12.90	25.4	20.0	50.0	80.0
0.4	254.0	13.10	25.4	20.0	50.0	80.0
0.6	254.0	13.30	25.4	20.0	50.0	80.0
0.8	254.0	13.50	25.4	20.0	50.0	80.0

3.3 Fabrication of Self-Aligned Ball Pin

In order to maintain coaxial peel force during the testing, two self-aligned, free-rotating ball pins were designed and fabricated using tool-grade steel, as schematically shown in Fig. 3.3.1.

One end of the ball pin with threads was mated with the prefabricated threads within the holes in the test specimen, and the other end was connected with the MTS machine. The ball pin had an ability to rotate 360^{o} in the XZ plane and 30^{o} to -30^{o} in the XY and YZ planes.

3.4 Instrumentation and Test Method

The MTS 810 machine was used to conduct the peel test and collect the loading force data "P" and the displacement "Δ" of the DCB specimens at the loading point. The fracture test was conducted under the displacement controlled mode. The loading rate was set as 1 μm/s and the data collecting frequency was 1 Hz.

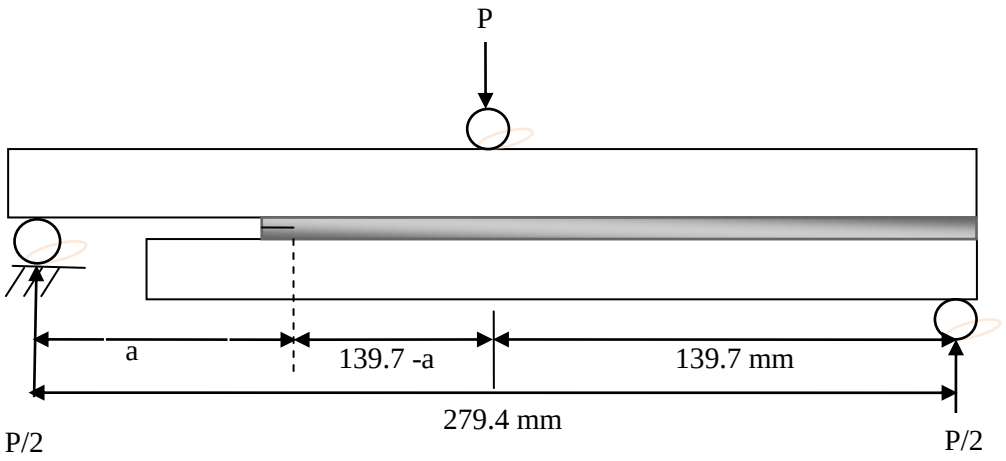

Figure 3.2.6: Schematic of single leg bending test

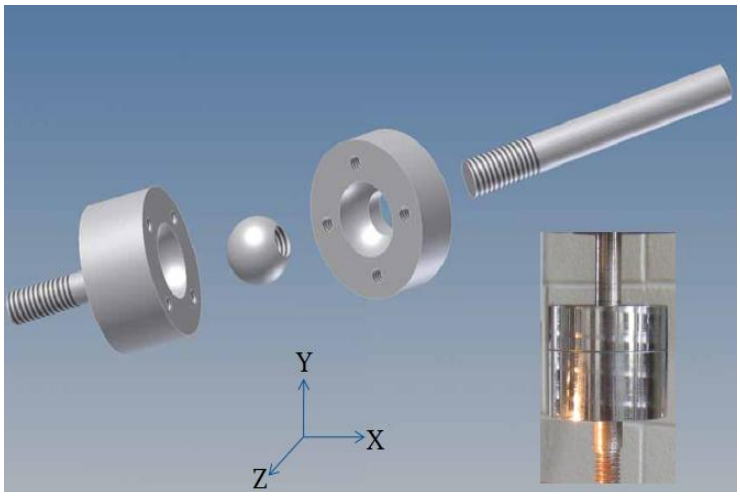

Figure 3.3.1: Schematic of self-aligned free-rotating ball joint

In order to measure the rotating angle "θ" of the adherends during the peel test, a digital inclinometer and sensor were attached at the free end of the adherends to collect the data during the test. The accuracy of the inclinometer is 0.01^{o}. The test range is from -70^{o} to 70^{o}. The data acquisition frequency is 1 Hz.

Sony XCD-CR90 High resolution CCD camera with a resolution of 3.7×3.7 μm/pixel was used in this experiment. The position of the camera was adjusted to be perpendicular to the side of the test specimen and the deformation images of test specimen during the test was shot, with focus on the adhesive layer. The camera shooting rate was 1 Hz. The collected images were input to an image processing toolkit, *ImageJ*, to post-analyze the recorded images and thus obtained the local separation of the crack tip "δ". The Mode I, Mode II, and Mixed Mode (Mode I/ Mode II) test setup was shown in Fig. 3.4.1, Fig. 3.4.2, and Fig. 3.4.3, respectively.

Figure 3.4.1: DCB specimen attached with inclinometer during the peeltest

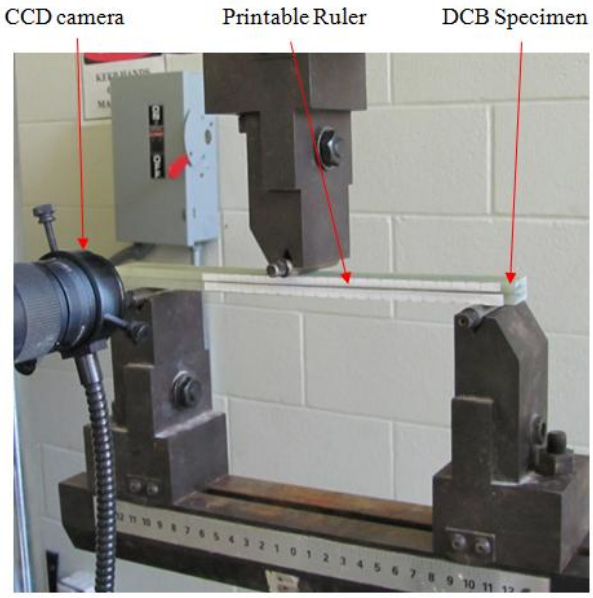

Figure 3.4.2: DCB specimen during the peel test

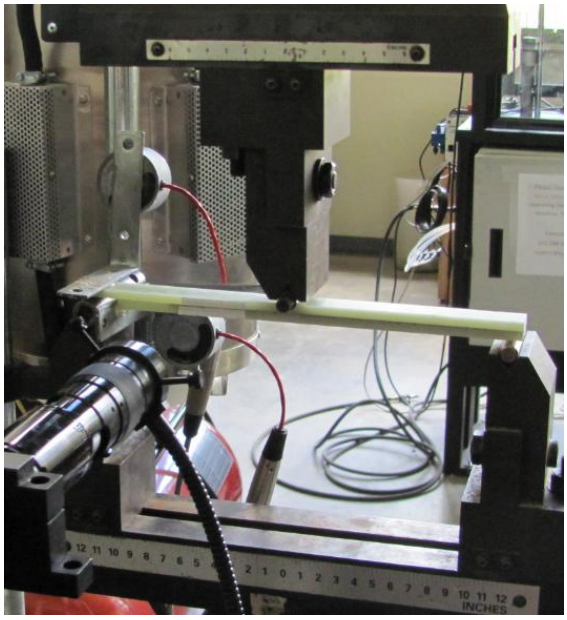

Fig. 3.4.3: Mixed Mode I/II fracture test of two adhesively bonded laminated composite joint with mini inclinometer and high resolution CCD camera

CHAPTER 4

RESULTS AND DISCUSSION OF MODE I TEST

This chapter includes two parts: one is the results and discussion based on the Mode I test data of steel adherends DCB specimens; the other is based on the data of laminated composite DCB Specimens.

4.1 Results and Discussions of Mode I Test with Steel Based Specimen

4.1.1 Global Test Results

The loading rate (at loading point) was equal to 1 μm/s. The preliminary studies showed that this rate could lead to a very stable descending branch when the crack was propagated, and it could be safely treated as a quasistatic loading condition. In the current study, a total of six groups of specimens which were numbered from group 1 to group 6 for the average adhesive thicknesses of 0.09 mm, 0.2mm, 0.4mm, 0.6mm, 0.8mm, and 1mm, respectively, were prepared and tested. Each group had 5 effective specimens, and a total of 30 effective specimens experienced the double cantilever beam (DCB) test by using the MTS 810 machine. The geometric parameters of each specimen are given in Table 4.1.1. Based on the analytical results of Ouyang and Li (2009a), with the current geometric configuration and the experimental data, it was found that all adherends (tool-grade steel) remained linear elastic during the entire test process without any plastic deformation. This indicates that all energy dissipations were contributed by cohesive fracture and the plastic dissipations in the adhesive layer. A typical force vs. displacement curve (a specimen in group 2 with an adhesive thickness of 0.2 mm) at the loading point is shown in Fig.4.1.1.

Table 4.1.1 Geometry of specimens

Group Number	Average adhesive thickness (mm)	Length (mm)	Height (mm)	Width (mm)	Initial Crack Length (mm)
1	0.09	254.10	6.35	25.41	52.12
2	0.2	254.11	6.35	25.44	52.22
3	0.4	254.09	6.34	25.42	52.18
4	0.6	254.08	6.35	25.39	52.44
5	0.8	254.10	6.36	25.46	52.37
6	1.0	254.08	6.35	25.37	52.11

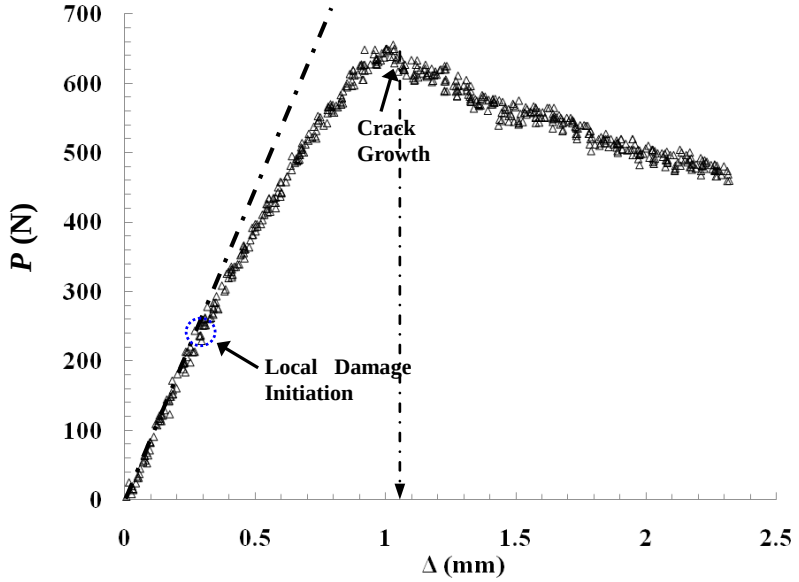

Figure 4.1.1: A typical relationship between loadline displacements Δ and loadline peel force *P* for Group 2 (h_a=0.2mm)

The force linearly increased until the local damage occurs. The load nonlinearly increases until the crack initiation process is completed. After that, the crack tip starts propagating. A continuous drop in the peel force was seen as the crack continuously propagated until the crack reached the DCB specimen's end.

Although there was no TEM, AFM or spectroscopy (XPS) examination of the morphology of fractured surfaces, with the help of high resolution microscope, it was

found that the failure mode is cohesive fracture for all cases. Even for the thinnest adhesive layer of 90μm, an extremely thin adhesive layer was remained on the surfaces of the two separated adherends. It was thus believed that even for the thinnest layers, failure mode is still in the form of cohesive fracture instead of adhesive failure. This failure mode may be because careful surface cleaning and treatment were conducted during the specimen preparation associated with the good bonding between the adhesive and adherends.

The data of the rotation angel at the loading point were collected by the inclinometer.

A typical experimental curve between the rotation angle θ_P at the loadline and the displacement Δ at the loadline (a specimen in group 2 with thickness of 0.2 mm) is shown in Fig. 4.1.4. With Eq. (2-41), the experimental energy release rate J is determined by combining the measured θ_P and P (or combining Fig. 4.1.1 and Fig. 4.1.2). A typical relationship (a specimen in group 2 with thickness of 0.2 mm) between global energy release rate J and loadline displacement Δ is given in Fig. 4.1.3. In a real test, we found that it was fairly difficult to exactly define when the initial crack tip was propagated. Therefore, a characteristic strain energy release rate J_0 was defined which represented the J value when the maximum peel force P was reached. Note that with the growth of the crack, the global strain energy release rate keeps increasing as shown in Fig. 4.1.3 (J-Δ curve). This implies that the plastic dissipations beyond the crack tip must keep increasing during this stable growth process. However, the increase rate of J becomes slower and slower as the crack grows, which seems nearly stable even by the end of the test. Therefore, an approximate asymptote is added in Fig. 4.1.3 to estimate the

interfacial toughness of the bonded joints. And this estimated asymptotic value is denoted by J_C or fracture energy.

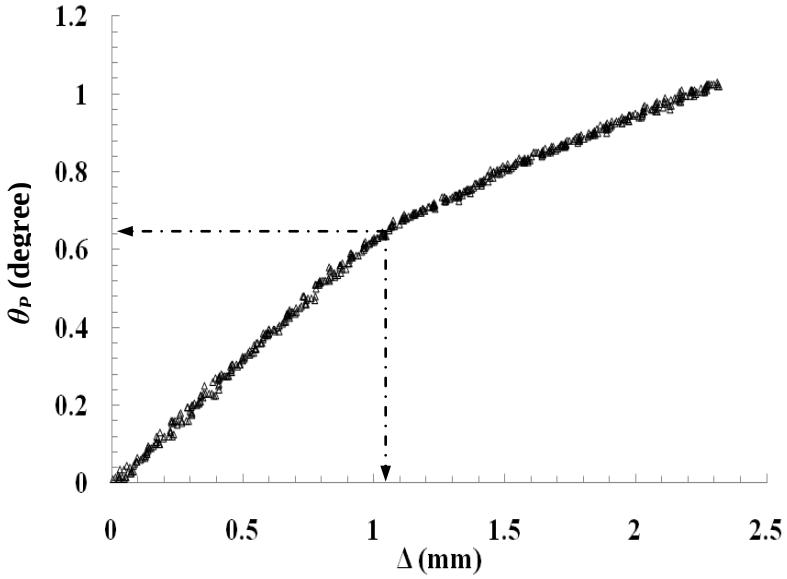

Figure 4.1.2: A typical relationship between loadline displacements Δ and loadline rotation of adherend θ_P for Group 2 (h_a=0.2mm)

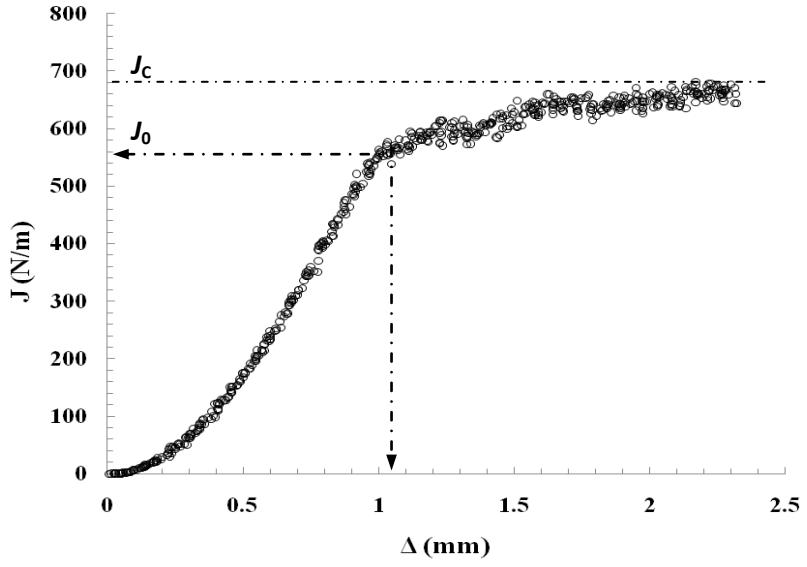

Figure 4.1.3: A typical relationship between loadline displacements Δ and energy release rate *J* for Group 2 (h_a=0.2mm)

4.1.2 Local Test Results

In this study, crack tip local deformations along the entire adhesive layer were recorded using high resolution CCD camera. It was also observed that a whitening zone appeared near the initial crack tip and was becoming more visible as the load was increased, as shown in Fig. 4.1.4.

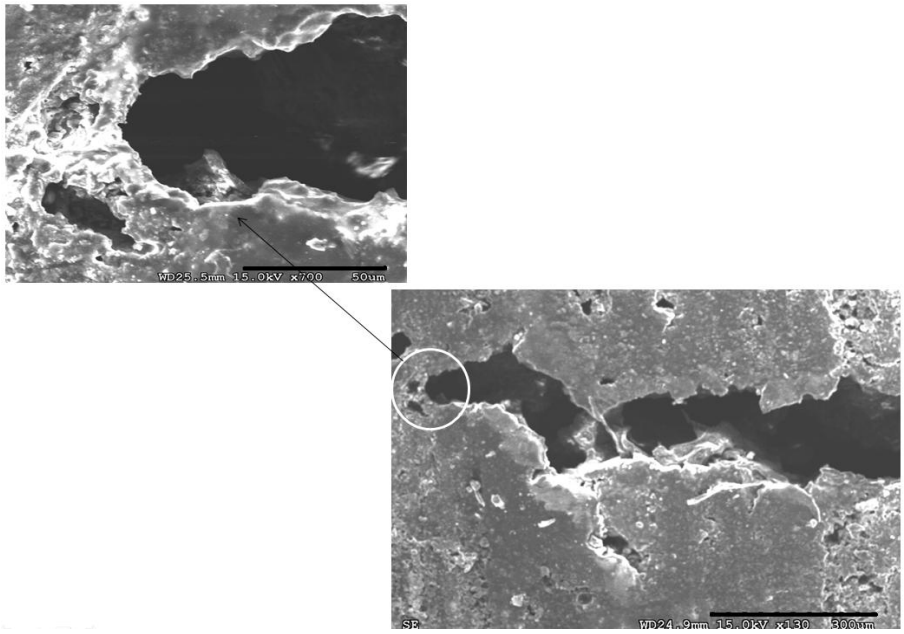

Figure 4.1.4: Local plastic deformation as shown by the whitening region

It was believed that the whitening zone consisted of numerous microcracks. When a lot of micro cracks were merged together and formed a macro crack, the initial crack started to propagate with the continuously increasing load. Digital images of the displacement field at the initial crack tip region were taken by the high resolution CCD camera. The value of the crack tip separation δ was measured as the relative normal displacement between the two adherends at the location of initial crack tip through the recorded digital images. Fig. 4.1.5 gives a typical relationship between the loadline displacement Δ (global displacement) and the local crack tip opening δ. By combining

Fig. 4.1.3 and Fig. 4.1.5, a typical experimental *J*-δ curve was obtained as shown in Fig. 4.1.6 (a specimen in group 2 with thickness of 0.2 mm). Based on Eq. (2-42), the experimental *J*-δ curves were used to determine the equivalent interfacial traction-separation laws or $\sigma=\sigma(\delta)$ at different adhesive thicknesses.

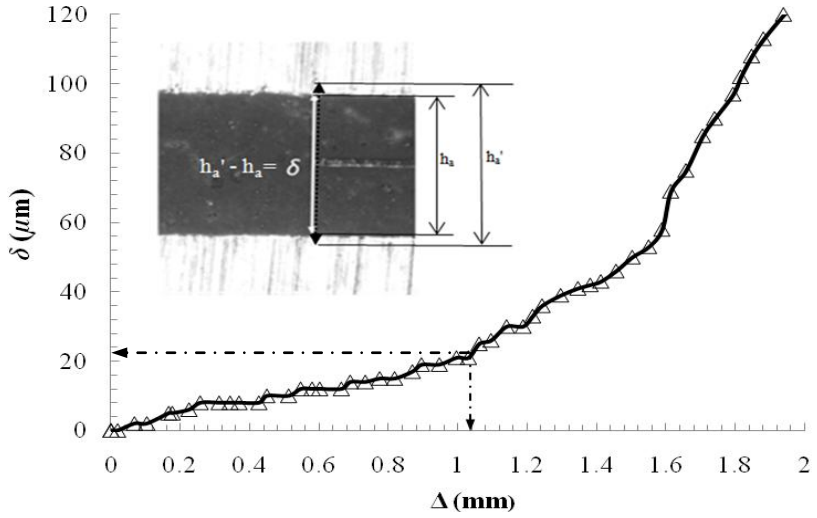

Figure 4.1.5: A typical relationship between loadline displacements

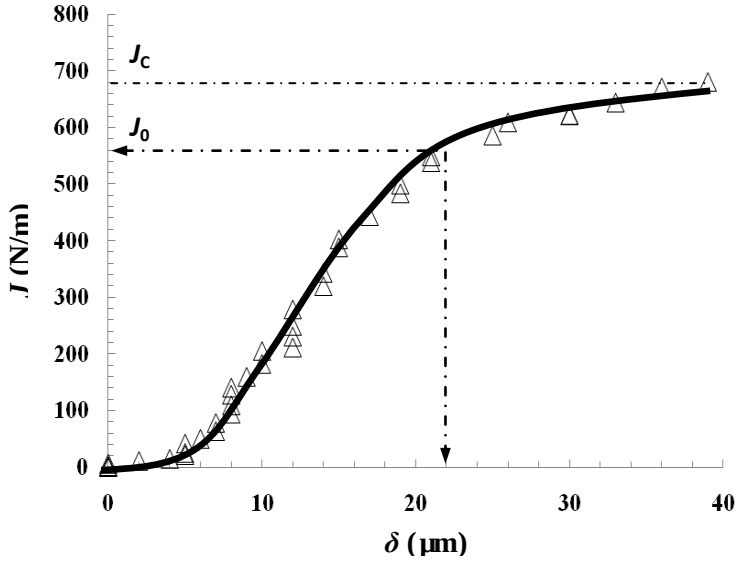

Figure 4.1.6: A typical relationship between energy release rate *J* and local crack tip separation δ for Group 2 (h_a=0.2mm)

4.1.3 Effects of the Thickness of the Adhesive Layer

With the global test results of different groups, the average maximum peel loads P_{cr} of the five specimens in each group (with error bar) are plotted as a function of the adhesive thicknesses (0.09 mm, 0.2 mm, 0.4 mm, 0.6 mm, 0.8 mm, and 1.0 mm) in Fig. 4.1.7. It can be observed that the average peak load was increased from 578.8 N (Group 1) to 791.12 N (Group 6) when the thickness of the adhesive layer increased (from 0.09 mm to 1.0 mm). These critical loads correspond to the characteristic energy release rate J_0. The average estimated fracture energy J_C (by the approximate asymptotes) and the average characteristic J_0 (at the maximum peel load) of the five specimens in each group (with error bar) were plotted as a function of the adhesive thickness in Fig. 4.1.8. One may see that the fracture energy J_C at the thickness of 0.09 mm is increased by approximately 160% when the adhesive thickness becomes 1.0 mm. The significant increase of J_0 and J_C are responsible for the increased load capacity when the adhesive thickness becomes thicker. Meanwhile, with Fig. 4.1.8, one may see that when the adhesive thickness is thin, J_0 and J_C are relatively close to each other. On the other hand, when it is relatively thick, J_0 and J_C are relatively departed from each other. Thus, we denote the difference between J_0 and J_C by $\Delta J=J_C-J_0$. Let's consider a parameter ξ, which represents the ratio of the average ΔJ over the pertinent average J_0 of the five specimens in each group. This ratio ξ is then plotted as a function of the adhesive thickness in Fig. 4.1.9. Obviously, the ratio ξ represents the relative increase in J to its initial value of J_0 as J value becomes a nearly stable value (J_C). Thus, Fig. 4.1.9 actually reflects the effects of adhesive thickness on the contributions by geometry a/h to the increase of plastic dissipations as crack grows.

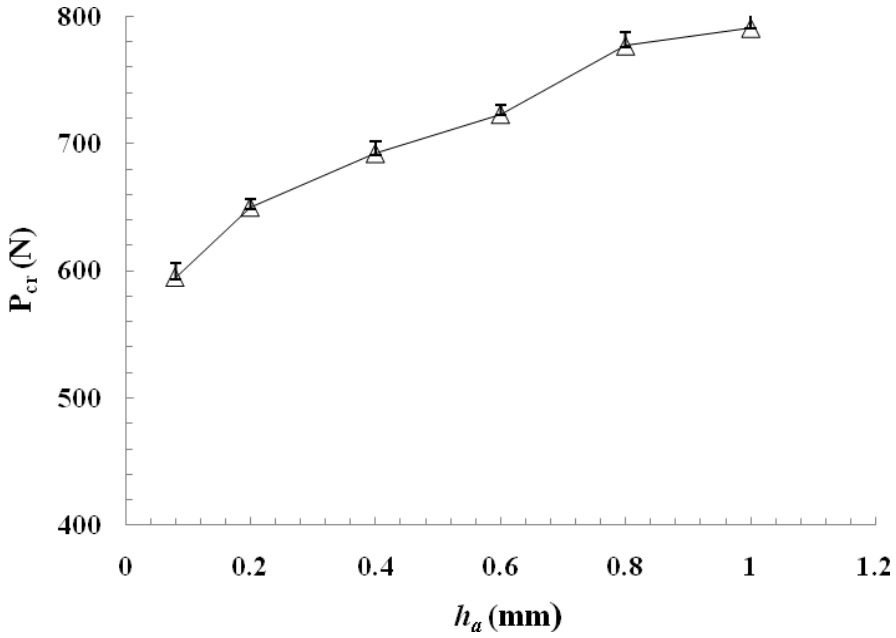

Figure 4.1.7: The average maximum peel load P_{cr} at different adhesive thicknesses h_a

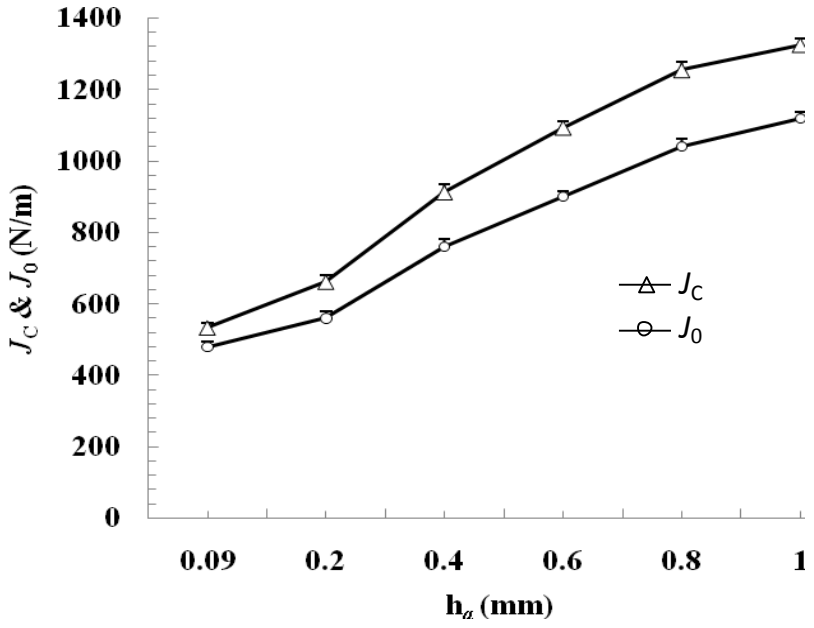

Figure 4.1.8: The estimated fracture energy J_C and the characteristic energy release rate J_0 (corresponding to P_{cr}) with different adhesive thicknesses h_a

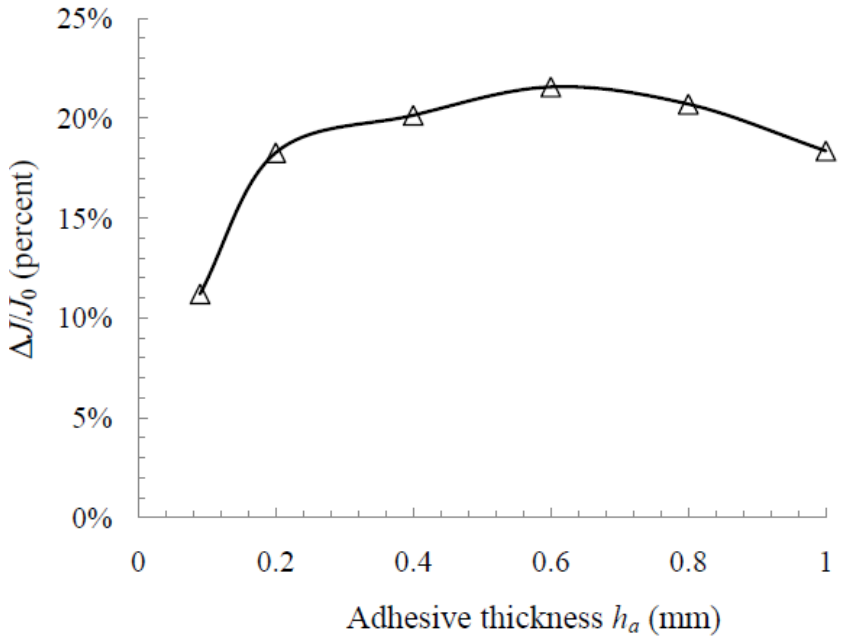

Figure 4.1.9: The ratio of ΔJ ($\Delta J=J_C-J_0$) over J_0 as a function of the adhesive thickness h_a

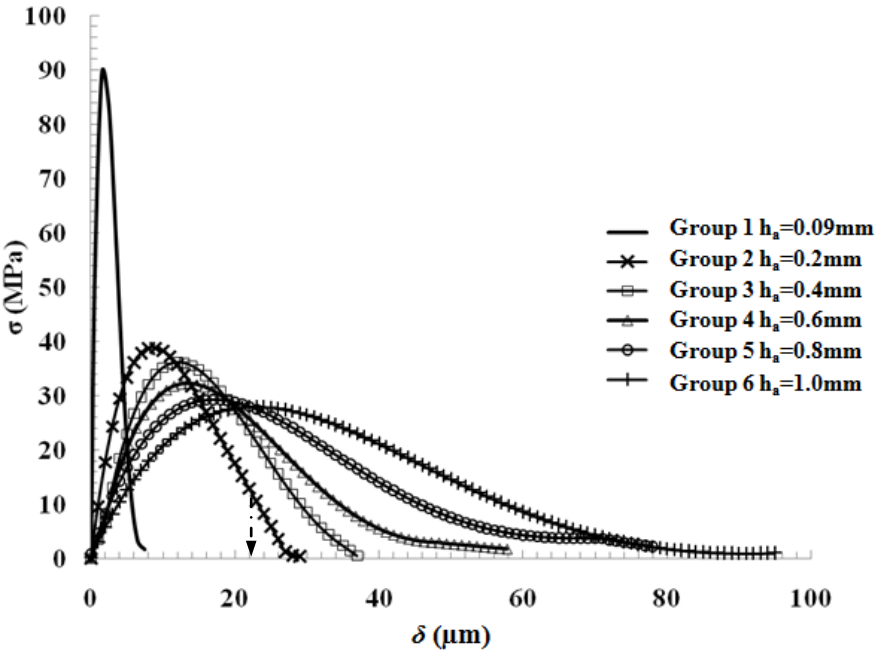

Figure 4.1.10: Typical shape of the equivalent interfacial traction-separation laws with different thicknesses of adhesive layer

After data collecting and curve-fitting process of the experimental J-δ curves, by applying Eq. (2-42), one can see that the interfacial traction-separation laws were

determined by numerically differentiating the experimental J-δ curves. The cohesive law was calculated for each specimen. The typical equivalent cohesive law of each group is given in Fig.4.1.10 at different adhesive thicknesses. From Fig. 4.1.10, one can see that three major effects of the adhesive thickness. First, the local characteristic separation (δ_0) corresponding to the interfacial strength σ_{max}, decreases with the decrease of the adhesive thickness. Second, the interfacial strength increases with the decrease of the adhesive thickness. Finally, the total area under the δ-σ curve, which represents the strain energy release rate at crack propagation, increases with the increase of the adhesive thickness. The complete thirty interfacial traction-separation laws (six groups with various adhesive thicknesses) are given in Fig. 4.1.11. One may see the five specimens in each group (each adhesive thickness) present fairly consistent results.

The average interfacial strength σ_{max} of the six groups (with error bar) are plotted as a function of the adhesive thickness in Fig. 4.1.12. According to the manufacturer, the tensile strength of the bulk adhesive material is approximately 30.3 MPa (its yield strength is slightly lower than its tensile strength). One can see that the interfacial strength was 88 MPa at the thickness of 0.09 mm, which is approximately 3 times as large as the yield strength of the bulk adhesive material. The author expects that with further decrease of the adhesive thickness, the measured equivalent interfacial strengths should keep increasing. On the contrary, with the increase of adhesive thickness, the measured interfacial strengths asymptotically approach a constant value. This asymptote seems being the yield strength of bulk adhesive material. Another phenomenon is that the equivalent interfacial strength seems increasing dramatically when the adhesive thickness was thinner than a certain value (such as 0.2 mm).

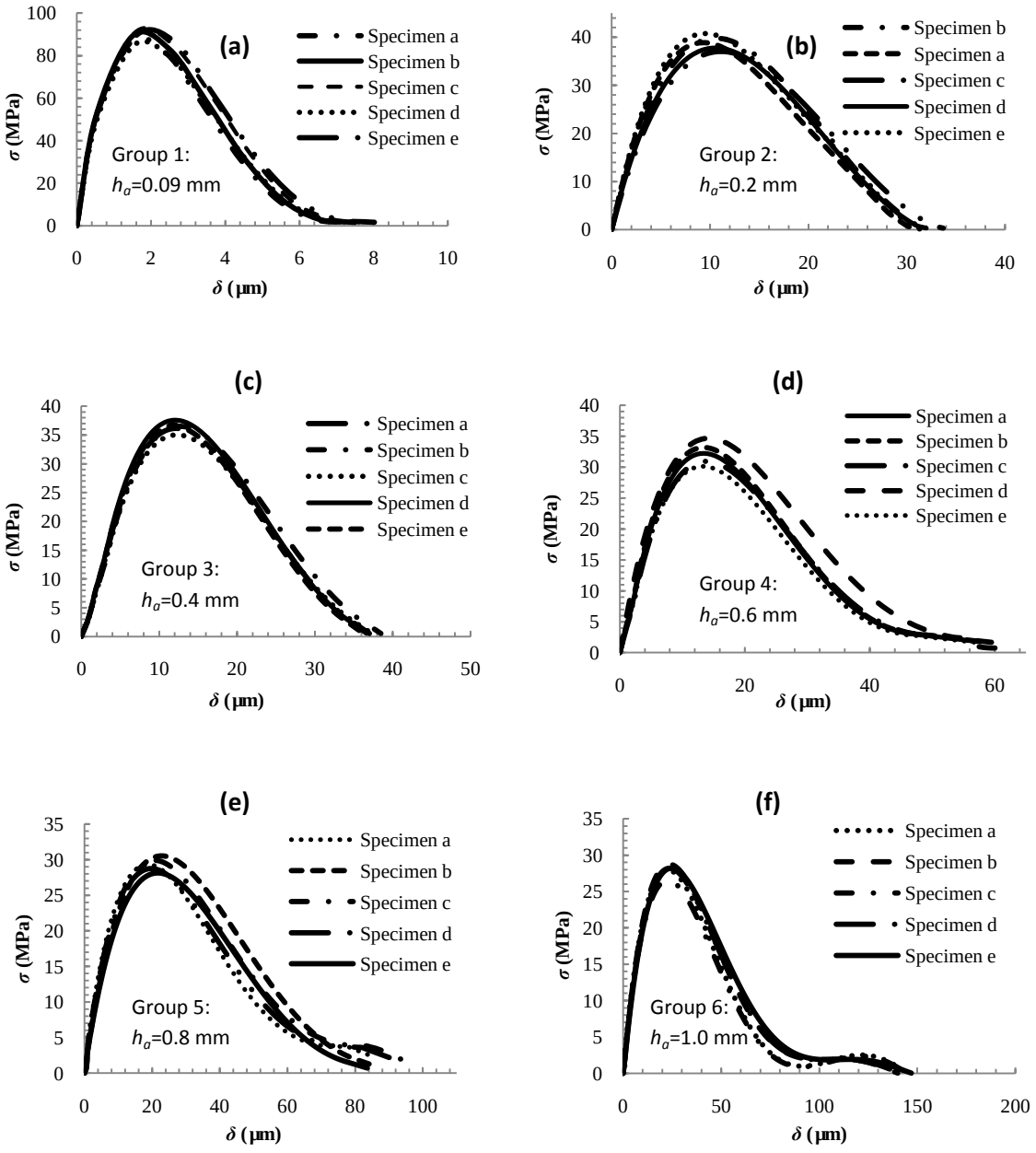

Figure 4.1.11: The shapes of all equivalent interfacial traction-separation laws with different thicknesses of adhesive layer: (a) adhesive thickness h_a=0.09 mm; (b) adhesive thickness h_a=0.2 mm; (c) adhesive thickness h_a=0.4 mm; (d) adhesive thickness h_a=0.6 mm; (e) adhesive thickness h_a=0.8 mm; (f) adhesive thickness h_a=1.0 mm

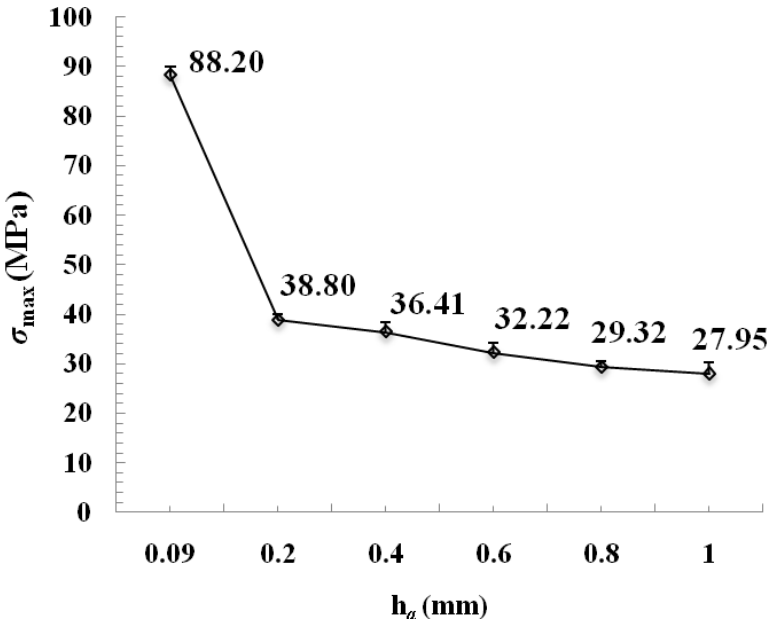

Figure 4.1.12: The effect of the adhesive thickness on the interfacial strength σ_{max}

4.2 Test Results and Discussions of Mode I with Laminated Composite Based Specimen

4.2.1 Global and Local Tests

A typical force vs. displacement curve at the loading point (a specimen in group 3 with an adhesive thickness of 0.4 mm) is shown in Fig. 4.2.1. Based on our experimental observations, there were no fiber bridging phenomena occurred between the two prefabricated composite laminates during the peel test.

Nearly all nonlinear energy dissipations were contributed by the cohesive fracture and the plastic dissipations in the bondline. With the help of the high resolution microscope, it was found that even for the thinnest bondline with thickness of 0.1mm, an extremely thin adhesive layer was remained on the surfaces of the two separated composite substrates.

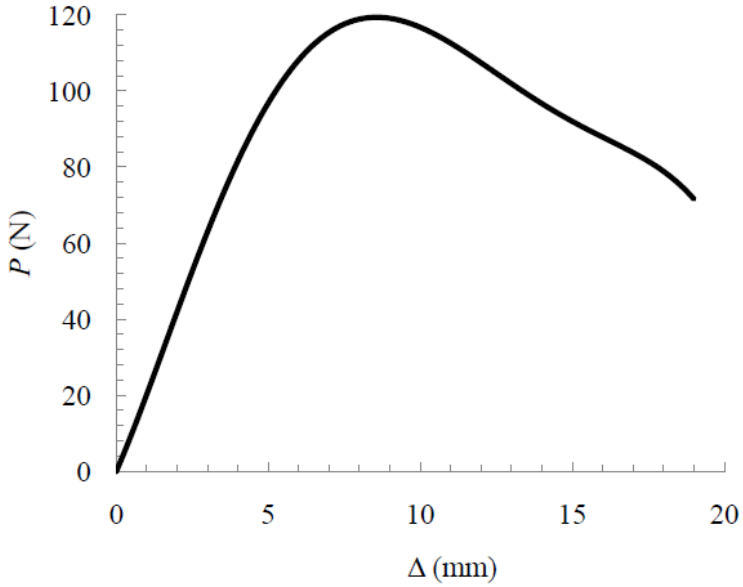

Figure 4.2.1: A typical relationship between loadline displacements Δ and loadline peel force *P* for Group 3 (h_a=0.4 mm)

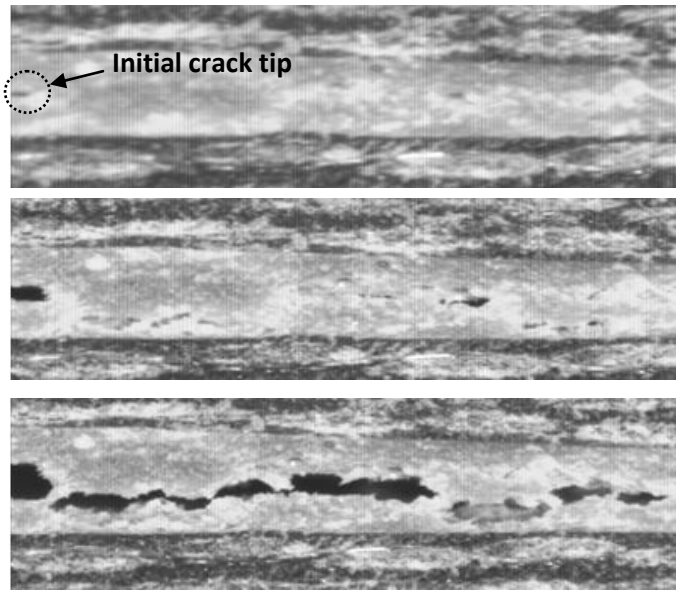

Figure 4.2.2: Local damage, fracture and deformation in the bondline

Therefore, it is believed that the failure mode is cohesive fracture instead of adhesive failure. It was also observed that a whitening zone appeared near the initial

crack tip and was becoming more visible as the load was increased during the fracture test process, as shown in Fig. 4.2.2. It is believed that the whitening zone consisted of many microcracks. When a lot of microcracks were merged together, a macro crack was formed with the increasing load.

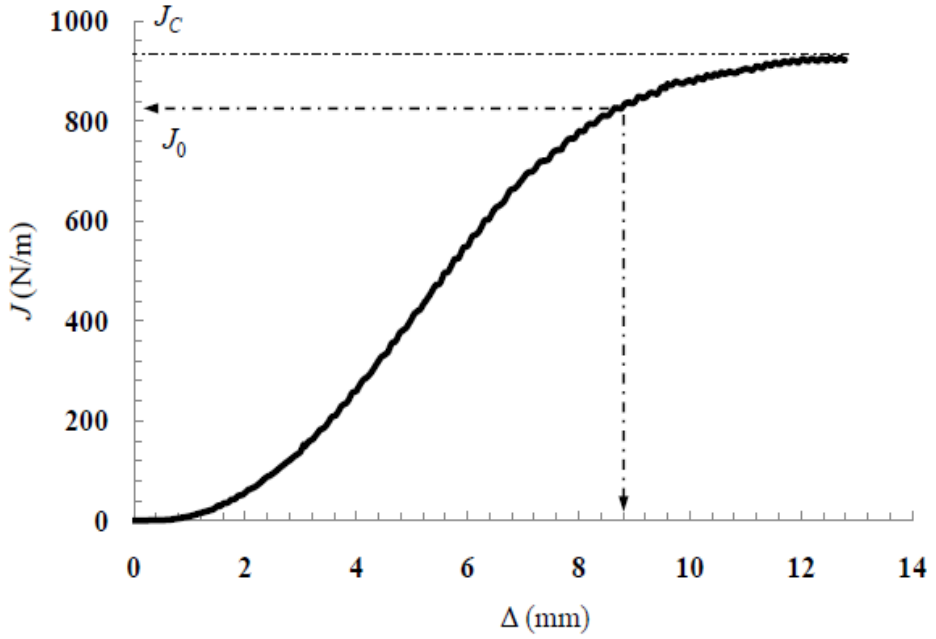

Figure 4.2.3: A typical relationship between loadline displacements Δ and energy release rate *J* for Group 3 (h_a=0.4 mm)

The experimental energy release rate J is calculated according to Eq. (2-41) with the measured loadline rotation θ_P and peel force P. A typical relationship between global energy release rate J and loadline displacement Δ is given in Fig. 4.2.3. In a real test, we found that it was fairly difficult to exactly define when the initial crack tip was propagated. Therefore, a characteristic strain energy release rate J_0 was adopted where the maximum peel force P_{cr} was reached. Note that with the growth of the crack, the global strain energy release rate keeps increasing as shown in Fig. 4.2.3 (J-Δ curve). This implies that the plastic dissipations beyond the crack tip must keep increasing during this

stable growth process. However, the increase of J becomes slower and slower as the crack grows, which seems nearly stable even by the end of the test. Therefore, an approximate asymptote is added in Fig. 4.2.3 to estimate the interfacial toughness. And this estimated asymptotic value of the fracture energy is denoted by J_C.

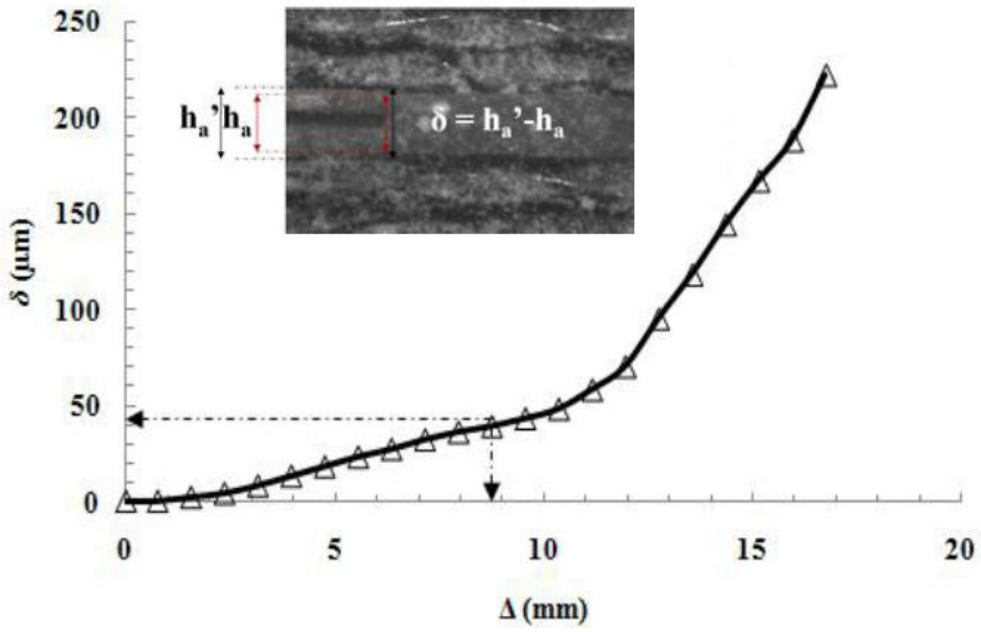

Figure 4.2.4: A typical relationship between loadline displacement Δ and local crack tip separation δ for Group 3 (h_a=0.4 mm), where h_a' in the inset represents the interlayer's thickness after deformation from its initial thickness h_a

The value of the crack tip separation δ was measured as the relative normal displacement between the two laminated composite adherends at the location of initial crack tip through the recorded digital images. Fig. 4.2.4 gives a typical relationship between the loadline displacement Δ (global displacement) and the local crack tip opening δ. By combining Fig. 4.2.3 and Fig. 4.2.4, a typical experimental J-δ curve was obtained as shown in Fig. 4.2.5 (a specimen in group 3 with thickness of 0.4 mm). With Eq. (2-42), the experimental J-δ curves were used to determine the equivalent interfacial traction-separation laws or $\sigma=\sigma(\delta)$ at different bondline thicknesses.

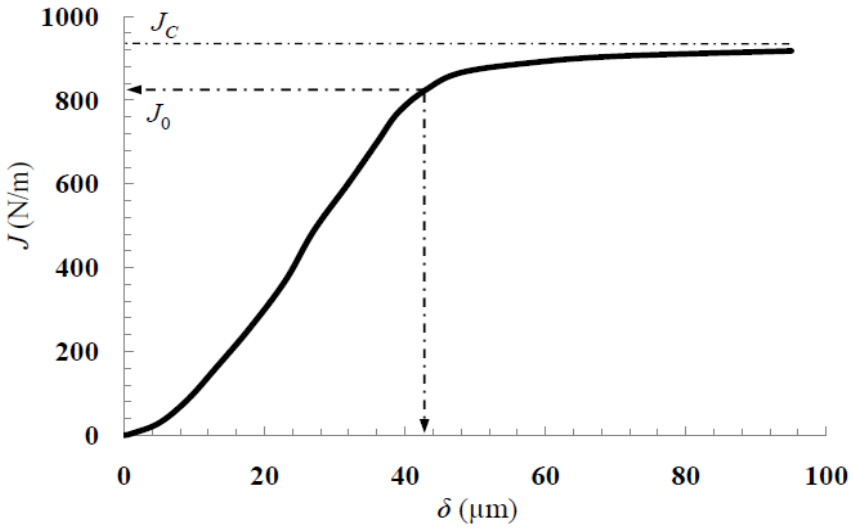

Figure 4.2.5: A typical relationship between energy release rate *J* and local crack tip separation δ for Group 3 (h_a=0.4 mm)

4.2.2 Effects of the Bondline Thickness

The average estimated fracture energy J_C and the average characteristic J_0 (at the maximum peel load) were plotted as a function of the bondline thickness in Fig. 4.2.6 (0.1 mm, 0.2 mm, 0.4 mm, 0.6 mm and 0.8 mm). The significant increase in J_0 and J_C is responsible for the increased load capacity when the adhesive becomes thicker. Meanwhile, one may see that when the adhesive thickness is thin, J_0 and J_C are relatively close to each other. When it is relatively thick, J_0 and J_C are relatively departed. After data collecting and curve-fitting process of the experimental *J*-δ curves, by applying Eq. (2-42), the interfacial traction-separation laws were determined by numerically differentiating the experimental *J*-δ curves. A typical equivalent interfacial law of each group is given in Fig. 4.2.7 at different bondline thicknesses. From Fig. 4.2.7, one may see the effects of the bondline thickness on the interfacial traction-separation laws of laminated composite joints. First, the interfacial strength increases with the increase of the bondline thickness. Second, the initial stiffnesses of the interfacial laws (the initial

slope of the σ-δ curve) are identical with various bondline thicknesses. Finally, the fracture energy (the total area under the δ-σ curve) increases with the bondline thickness.

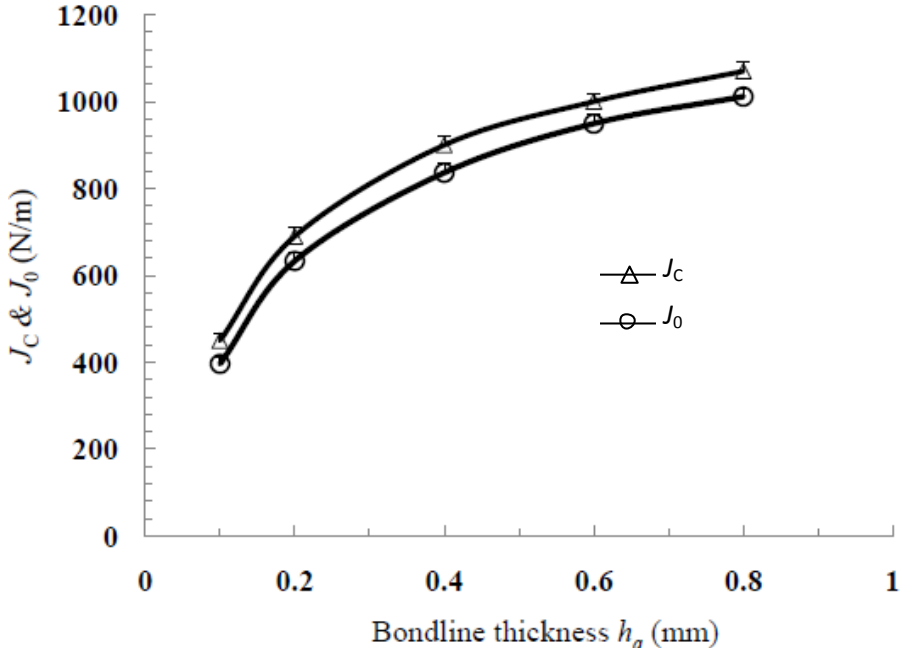

Figure 4.2.6: The estimated fracture energy J_C and the characteristic energy release rate J_0 (corresponding to P_{cr}) with different adhesive thicknesses h_a

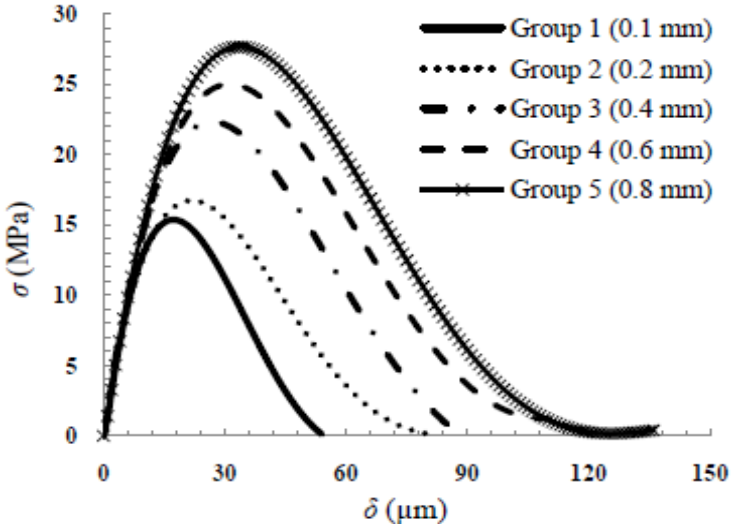

Figure 4.2.7: Typical shapes of the interfacial traction-separation laws of *bonded composite laminates* with different bondline thicknesses h_a

By comparing Fig. 4.2.7 with Fig. 4.1.10, one may find the significant difference of the effects of bondline thickness on the interfacial laws. For the steel joints, the thinner bondline caused a higher interfacial strength, which is opposite to that of the laminated composite joints. In addition, the initial stiffnesses of the interfacial laws for steel joints are dependent on bondline thickness, which is also different from composite joints. Obviously this is due to the different adherends made of composite laminates and steel. With the same bondline thickness and adhesive material, steel adherend has much higher stiffness than that of composite adherend, leading to higher constraint to the adhesive interlayer. The different external constraints cause the distinct different local interfacial traction-separation behaviors. A numerical study will be conducted to simulate this interesting phenomenon in the future. It is noted that for both cases, the total area under the δ-σ curve, which represents the strain energy release rate, increases with the bondline thickness as concluded by previous global fracture tests.

The average interfacial strength σ_{max} of the five groups (with error bar) are plotted as a function of the adhesive thickness in Fig. 4.2.8. According to the manufacturer, the tensile strength of the bulk adhesive material is approximately 30.3 MPa (its yield strength is slightly lower than its tensile strength). One can see that the interfacial strength of laminated composite joints was 15 MPa at the thickness of 0.1 mm, which is only approximately half of the yield strength of the bulk adhesive material. When the bondline thickness was 0.8 mm, the measured interfacial strength was approximately 27.3 MPa.

The author expects that with further increase in the bondline thickness, the measured interfacial strengths should asymptotically approach a constant value as the

case of a compact tension test. Interestingly, for the steel joints, with the increase of the bondline thickness, the measured interfacial strengths asymptotically approached a constant value (Ji et al. 2010). For both cases, this asymptote seems being the yield strength of the bulk adhesive material. However, these approaches come from different size. Finally, the complete fifteen interfacial laws of the bonded laminate composites (three specimens in each of the five groups at various bondline thicknesses) are presented in Fig. 4.2.9. One may see the fairly consistent results of the three specimens in each group at various bondline thicknesses.

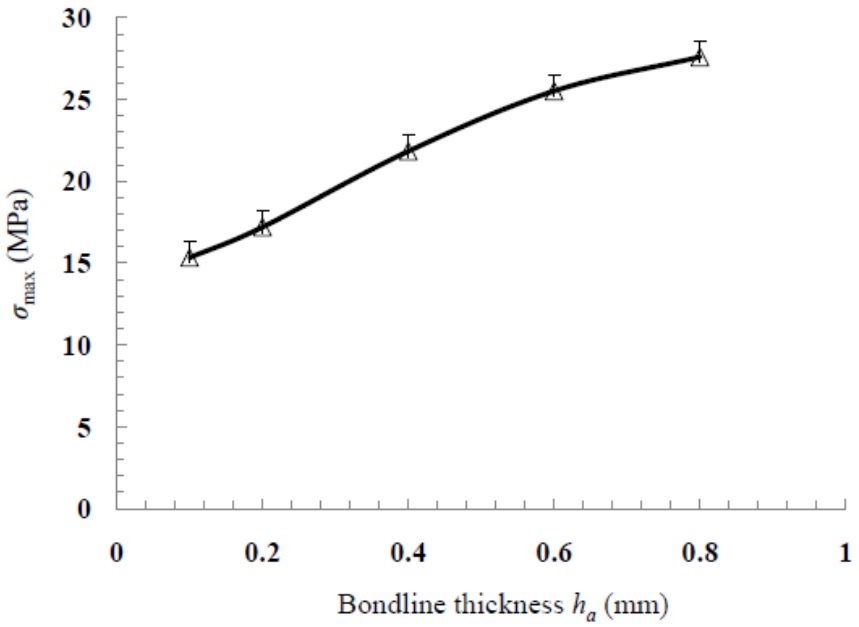

Figure 4.2.8: The effect of the bondline thickness on the interfacial strength σ_{max}

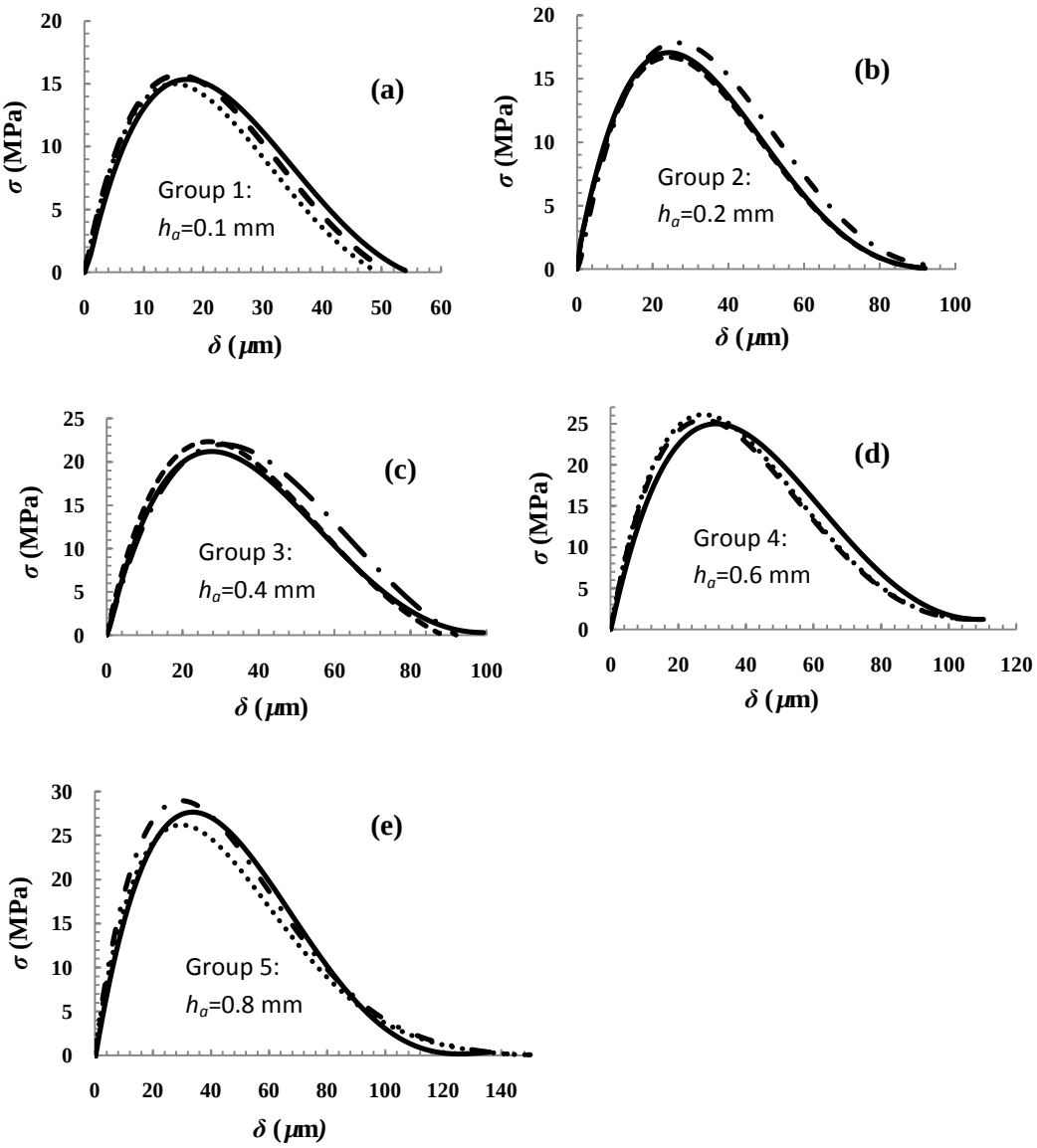

Figure 4.2.9: The shapes of all interfacial traction-separation laws with different thicknesses of bondline: (a) bondline thickness h_a=0.1 mm; (b) bondline thickness h_a=0.2 mm; (c) bondline thickness h_a=0.4 mm; (d) bondline thickness h_a=0.6 mm; (e) bondline thickness h_a=0.8 mm

CHAPTER 5

RESULTS AND DISCUSSIONS OF MODE II TEST

This chapter includes two parts: one is the results and discussion based on the Mode II test data of steel adherends ENF specimens; the other is based on the data of laminated composite ENF Specimens.

5.1 Results and Discussions of Mode II Test with Steel Based Specimen

5.1.1 Global and Local Experimental Results

Based on the analytical results of Ouyang and Li (2009a), with the current geometric configuration and the experimental data, it was found that all adherends (low carbon steel) remained linear elastic during the entire test process without any plastic deformation. This indicates that all the energy dissipation during the crack initiation and propagation were contributed by the intrinsic cohesive fracture and the possible plastic dissipation in the adhesive layer. A typical force vs. displacement curve at the loading point is shown in Fig. 5.1.1 (a specimen in group 1 with thickness of 0.1 mm). The force linearly increases until the local damage occurs. However, the load increases in a nonlinear form until the crack initiation process is completed. After that, the crack tip starts propagating. The crack continuously propagates with a continuous drop in the force until the crack propagates to the end of the ENF specimen. With Eq. (2-44), the experimental value of the strain energy release rate J_{II} can be obtained by combining experimental values of δ_0 and Q_T.

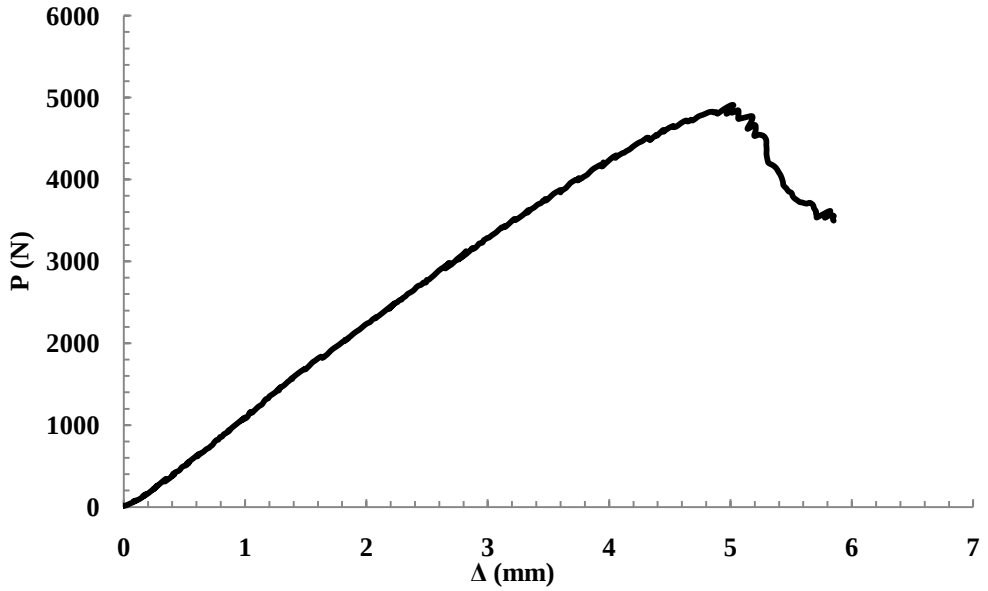

Figure 5.1.1: A typical relationship between loadline displacements Δ and loadline peel force *P* for Group 1 (h_a=0.1 mm)

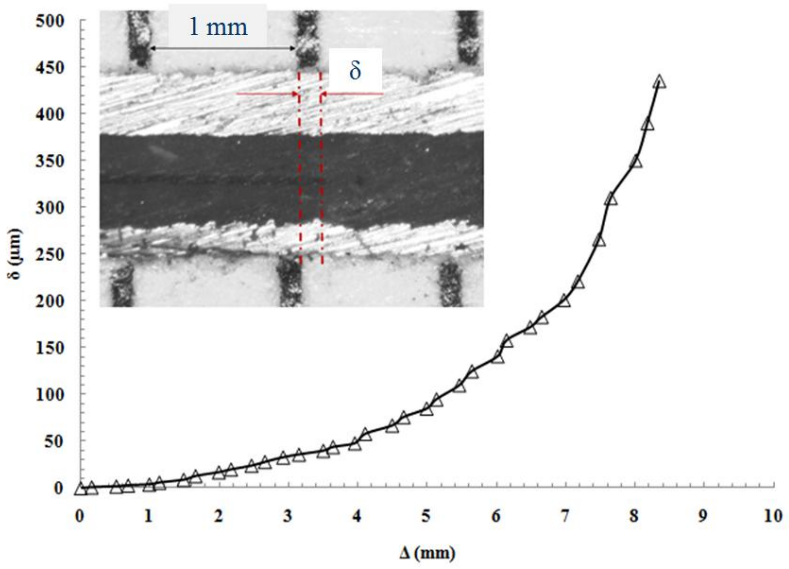

Figure 5.1.2: A typical relationship between loadline displacement Δ and local crack tip slip *δ* for Group 1 (h_a=0.1 mm)

The value of the shear slip w between the two adherends at the location of the initial crack tip is calculated based on the digital images, and they are plotted as a function of the loadline displacement Δ (global displacement) in Fig. 5.1.2 (a specimen in group 1 with thickness of 0.1 mm). By combining Fig. 5.1.1 and Fig. 5.1.2, a typical

experimental J-w curve is obtained as shown in Fig. 5.1.3 (a specimen in group 1 with thickness of 0.1 mm). With Eq. (2-45), the experimental J-w curves are used to determine the equivalent interfacial traction-separation laws or $\tau=\tau(w)$ at different adhesive thicknesses. A characteristic strain energy release rate J_0 is defined as the J value when the crack starts propagating immediately after the maximum fracture load P_{cr} is reached. It can be seen that J_0 is generally smaller than the critical strain energy release rate or the fracture energy J_{IIC}, which reflects that the strain energy release rate J_{II} keeps increasing after the crack propagation. This is because the plastic dissipation (or plastic zone) can be further increased after the crack initiation.

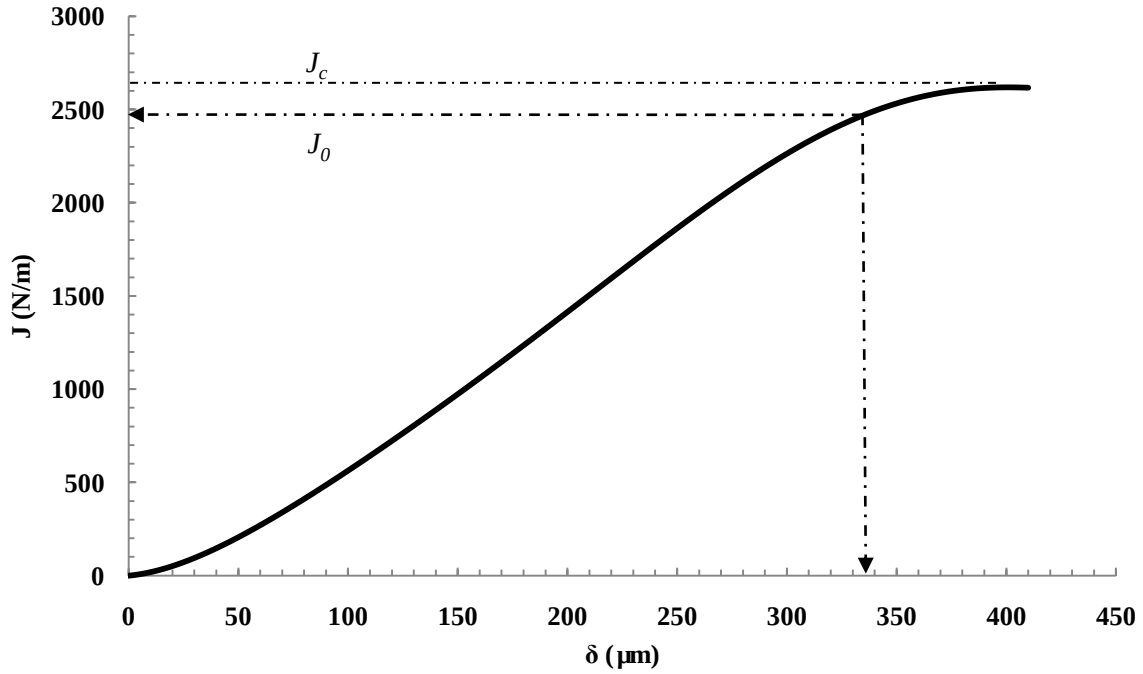

Figure 5.1.3: A typical relationship between energy release rate *J* and local crack tip slip *w* for Group 1 (h_a=0.1 mm)

In this study, the crack initiation and propagation process were recorded by using the high resolution CCD camera. It was observed that the initial crack tip started opening as the shear load increased. It was also observed that the whiting zone appeared near the

initial crack tip and was becoming more visible as the load was increased, as shown in Fig. 5.1.4 (red circle area).

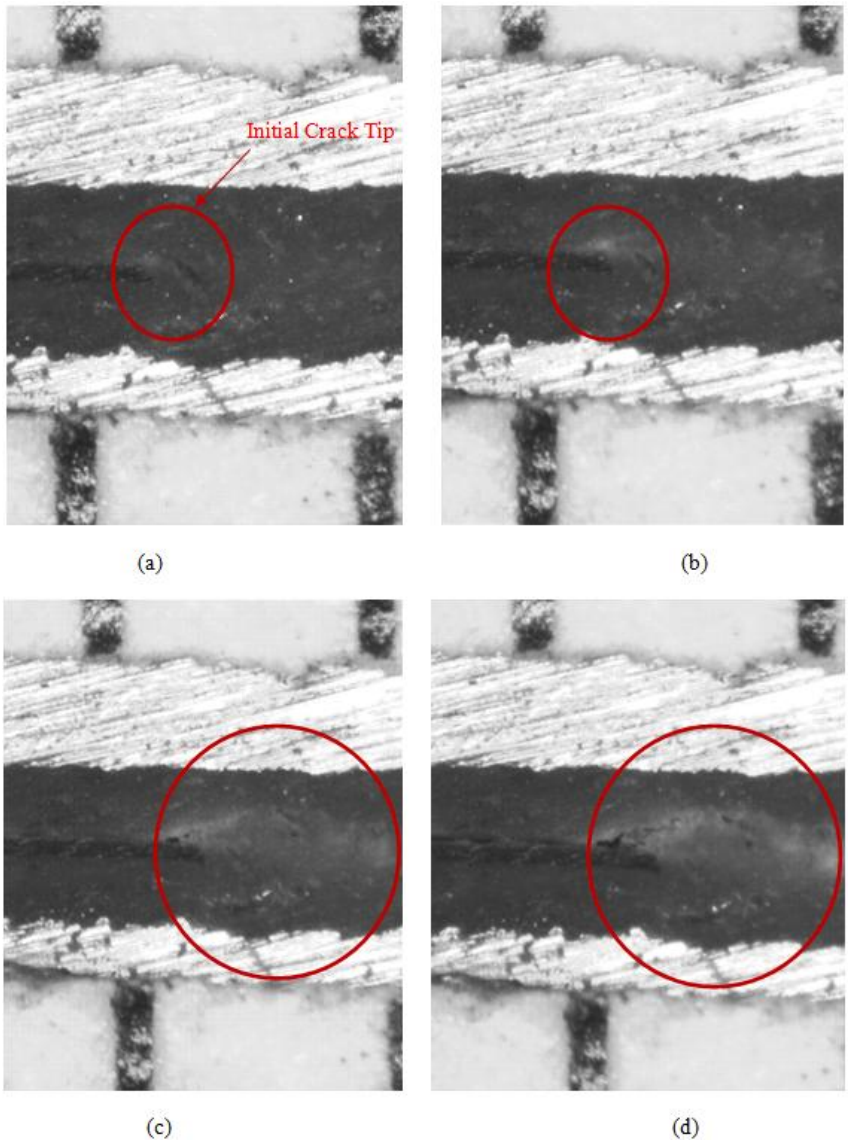

Figure 5.1.4: Local damage, fracture and deformation in the bondline

It was believed that the whiting zone consisted of numerous microcracks. When a lot of micro cracks were merged together and formed a macro crack, the initial crack started to propagate with the continuously increasing load, as shown in Fig. 5.1.5. Based on Eq. (2-45), these experimental *J*-*w* curves are used to determine the equivalent

interface cohesive laws or $\tau=\tau(w)$ at different adhesive thicknesses. Fig. 5.1.6 gives a typical shear stress vs. local slip displacement curve (a specimen in group 1 with thickness of 0.1 mm).

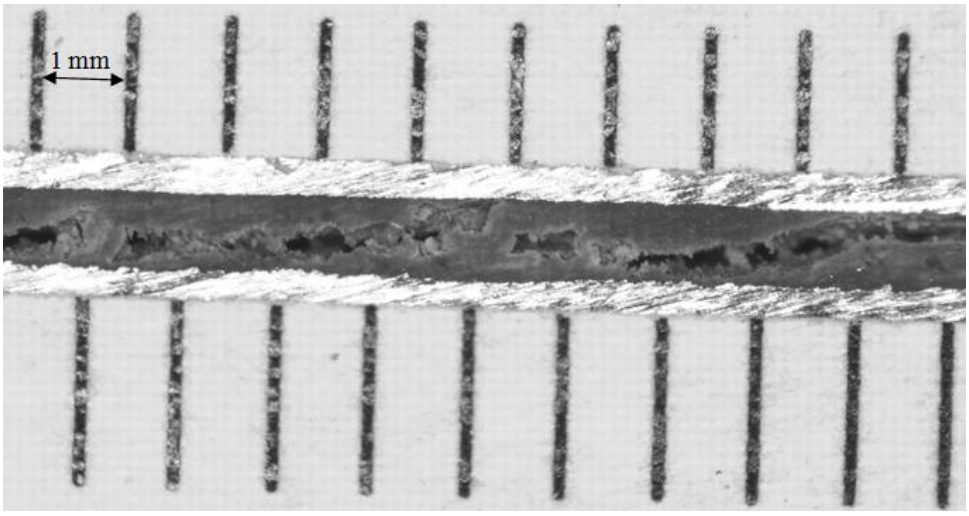

Figure 5.1.5 Crack propagates during the test

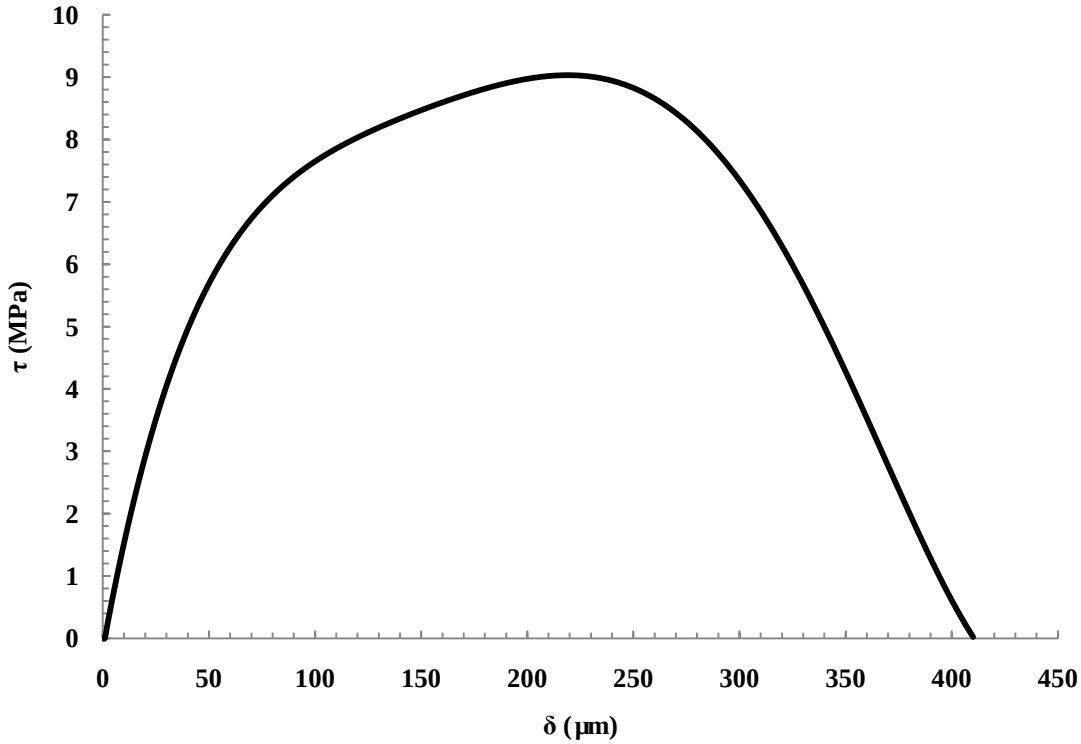

Figure 5.1.6: Typical interface constitutive relationship (equivalent cohesive law) for Group 1 (h_a=0.1 mm)

5.1.2 Effects of the Thickness of the Adhesive Layer

With the global experiment results for different groups, the maximum peel loads are plotted as a function of the adhesive thicknesses (0.1 mm, 0.2 mm, 0.4 mm, 0.6 mm, and 0.8 mm) as shown in Fig. 5.1.7. It can be observed that the average peak load is increased from 4912.24 N (Group 1) to 5836.33 N (Group 5) when the thickness of adhesive layer increases (from 0.1 mm to 0.8 mm). However, the rate of increase in the peak load reduces as the adhesive layer thickness increases, as shown by the trend line in Fig. 5.1.7.

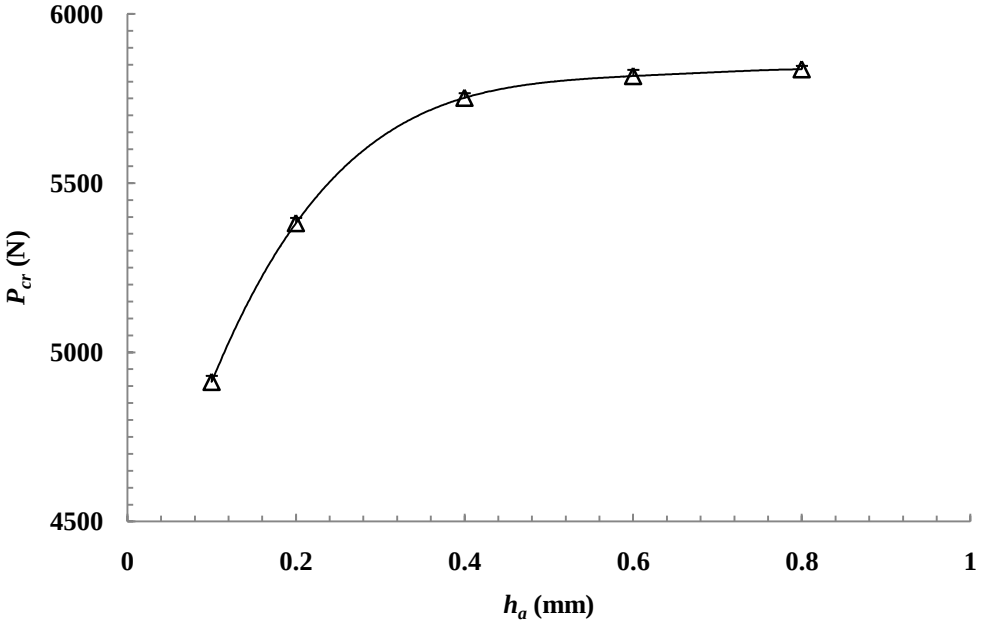

Figure 5.1.7: The average maximum shear load P_{cr} at different adhesive thicknesses h_a

The increase in the adhesive layer thickness might increase the bending stiffness of the ENF specimen. However, this contribution is very small since the adherends were made of low carbon steel with a much higher thickness of 9.535 mm and much higher bending stiffness. The estimated average fracture energy J_C and the average characteristic J_0 (at the maximum peel load) were plotted as a function of the adhesive thickness in Fig.

5.1.8 (0.1 mm, 0.2 mm, 0.4 mm, 0.6 mm and 0.8 mm). The significant increase in J_0 and J_C are responsible for the increased load capacity when the adhesive thickness becomes thicker. Meanwhile, one may see that when the adhesive thickness is thin, J_0 and J_C are relatively close to each other. When it is relatively thick, J_0 and J_C are relatively departed. After data collecting and curve-fitting process of the experimental J-w curves, by applying Eq. (2-45), one can see that the interfacial traction-slip laws are determined by numerically differentiating the experimental J-w curves.

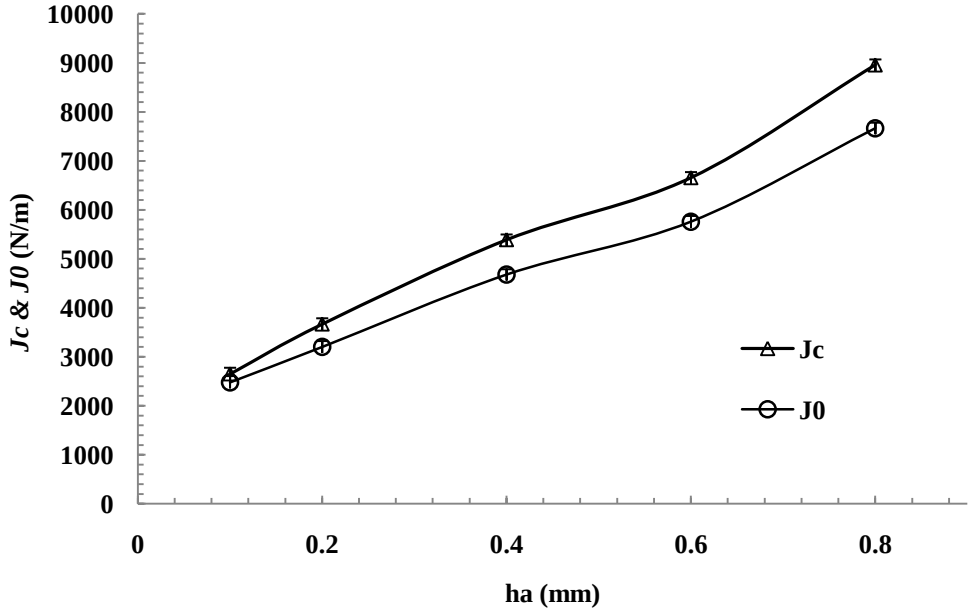

Figure 5.1.8: The estimated fracture energy J_C and the characteristic energy release rate J_0 (corresponding to P_{cr}) with different adhesive thicknesses h_a

A typical equivalent interfacial law of each group is given in Fig. 5.1.9 at different bondline thicknesses. One may see that the effects of the bondline thickness on the interfacial traction-slip laws. First, the interfacial strength increases for steel ENF joint with the increase of the bondline thickness. Second, the initial stiffness of the interfacial laws (the initial slope of the τ-w curve) is identical for steel ENF joints with various bondline thicknesses, which suggests that the shear deformation is controlled by

the adhesive layer. Finally, the fracture energy (the total area under the w-σ curve) increases with the bondline thickness. As shown in Fig. 5.1.9, the fracture energy J_C of the bonded joints is plotted as a function of the adhesive thickness. The fracture energy J_C at the thickness of 0.1 mm is increased by approximately 238% when the adhesive thickness is 0.8 mm. This significant increase in fracture energy can explain the increase in load capacity when the adhesive thickness is increased.

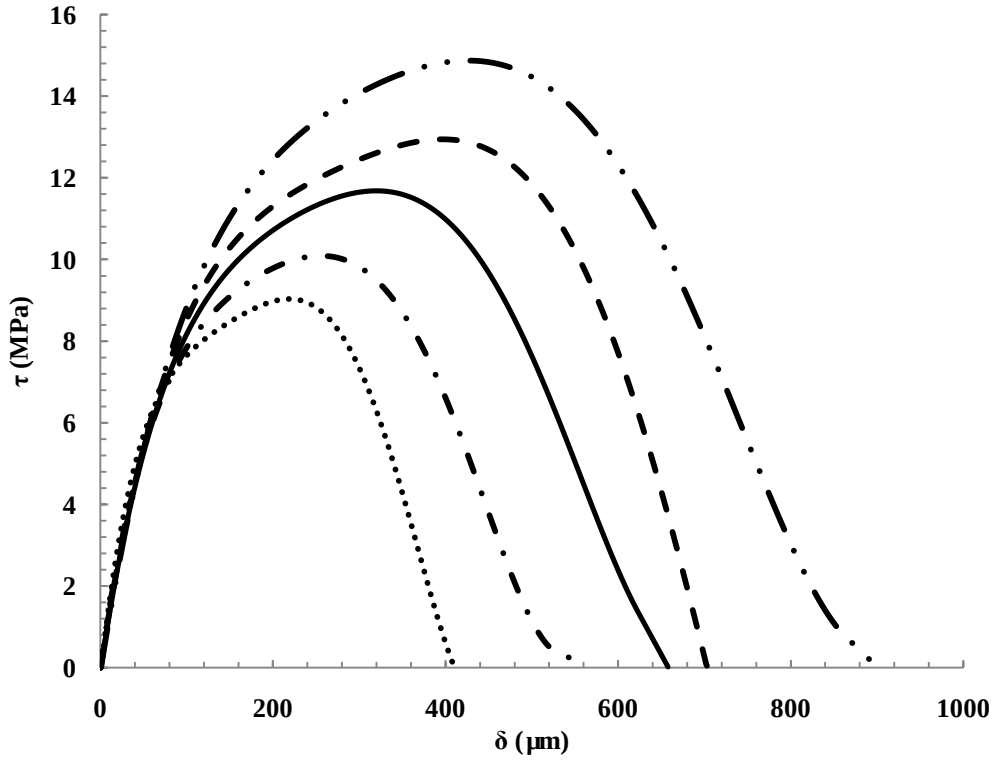

Figure 5.1.9: Typical shapes of the interfacial traction-slip laws of bonded steel with different bondline thicknesses h_a

The average interfacial strength τ_{max} of the five groups (with error bar) are plotted as a function of the adhesive thickness in Fig. 5.1.10. According to the manufacturer, the shear strength of the adhesive material is approximately 13.8 MPa (when the thickness is 0.75 mm with steel adherends). One can see that the interfacial strength was 14.9 MPa at the thickness of 0.8 mm, which is approximately the yield shear strength of the bulk

adhesive material. Finally, the complete fifteen interfacial traction-separation laws of the bonded steel ENF joints (three specimens in each of the five groups at various bondline thicknesses) are given in Fig. 5.1.11. One may see the fairly consistent results of the three specimens in each group at various bondline thicknesses.

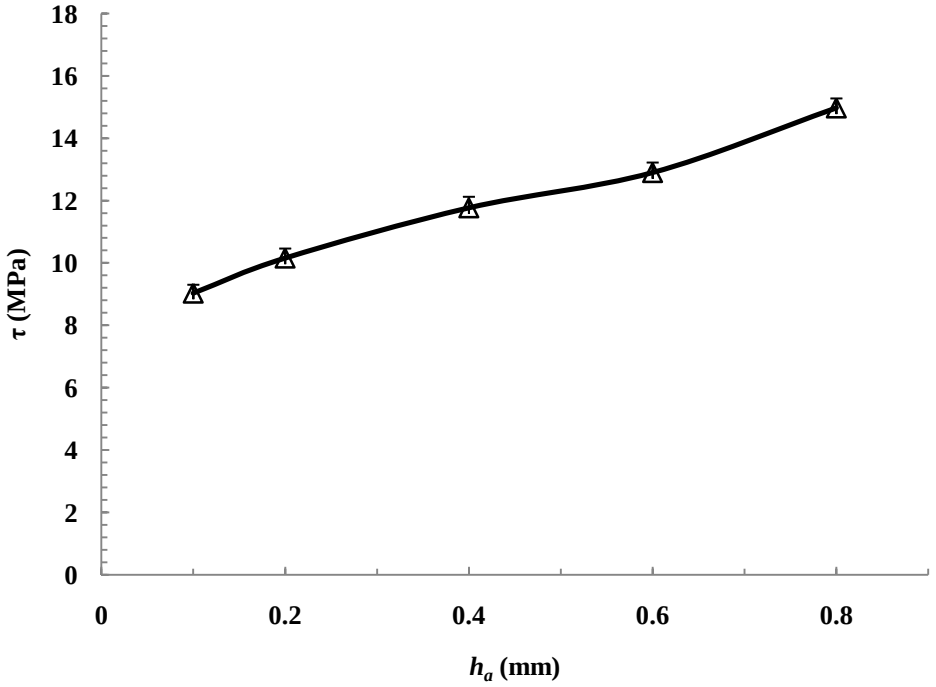

Figure 5.1.10: The effect of adhesive thickness on the maximum interface stress τ_f

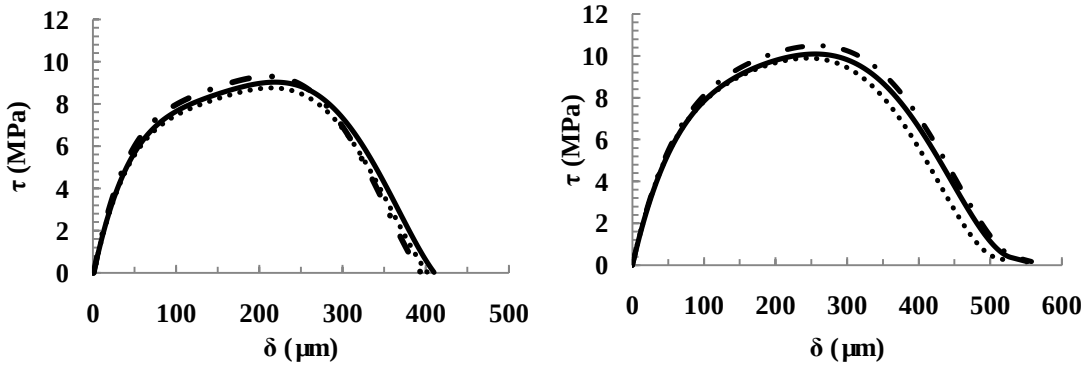

(a) (b)

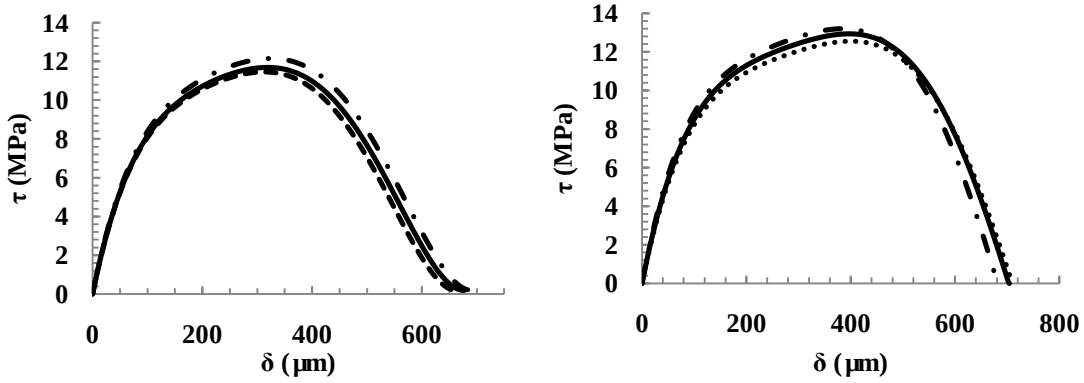

(c)

(d)

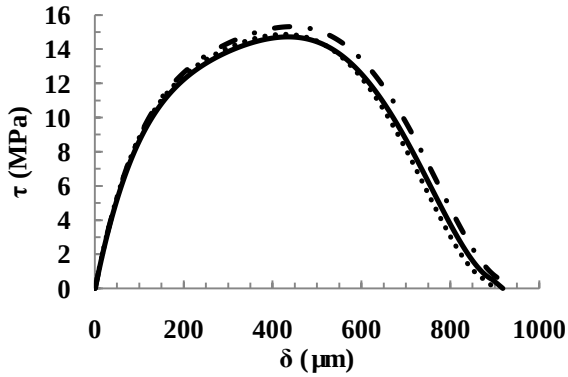

(e)

Figure 5.1.11: The shapes of all interfacial traction-slip laws with different thicknesses of bondline: (a) bondline thickness h_a=0.1 mm; (b) bondline thickness h_a=0.2 mm; (c) bondline thickness h_a=0.4 mm; (d) bondline thickness h_a=0.6 mm; (e) bondline thickness h_a=0.8 mm

5.2 Results and Discussions of Mode II Test with Laminated Composite Based Specimen

5.2.1 Global and Local Experimental Results

A typical force vs. displacement curve at the loading point is shown in Fig. 5.2.1 (a specimen in group 1 with thickness of 0.1 mm). The force linearly increases until the local damage occurs. However, the load increases in a nonlinear form until the crack initiation process is completed. After that, the crack tip starts propagating. The crack

continuously propagates with a continuous drop in the force until the crack propagates to the end of the DCB specimen. With Eq. (2-44), the experimental value of the strain energy release rate J_{II} can be obtained by combining experimental values of w_0 and Q_T.

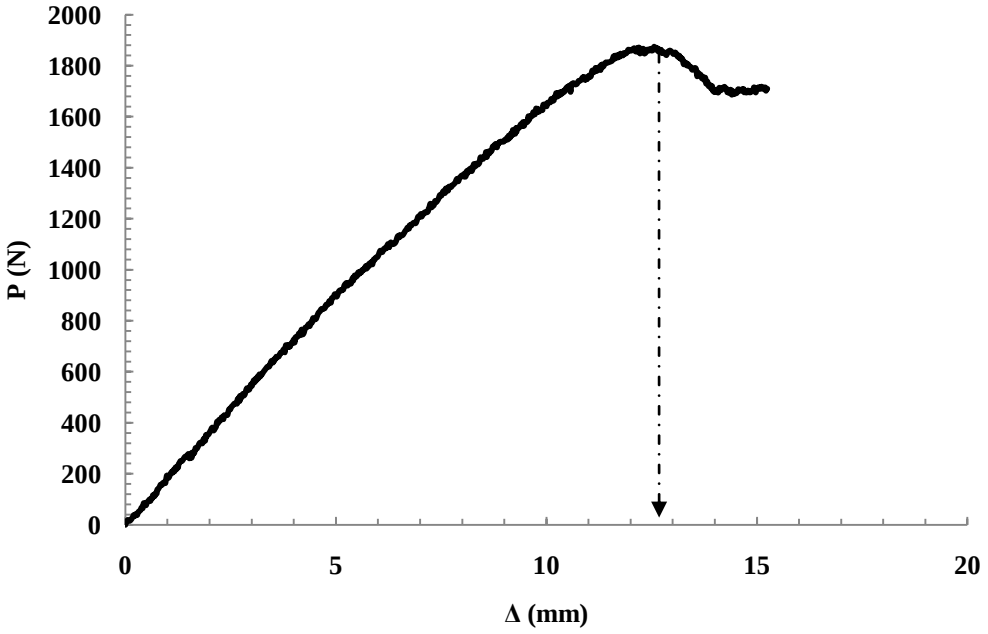

Figure 5.2.1: A typical relationship between loadline displacements Δ and loadline peel force *P* for Group 3 (h_a=0.4 mm)

The value of the shear slip w between the two adherends at the location of the initial crack tip is calculated based on the digital images, and they are plotted as a function of the loadline displacement Δ (global displacement) in Fig. 5.2.2 (a specimen in group 3 with thickness of 0.4 mm). By combining Fig. 5.2.1 and Fig. 5.2.2, a typical experimental J-w curve is obtained as shown in Fig. 5.2.3 (a specimen in group 3 with thickness of 0.4 mm). With Eq. (2-45), the experimental J-w curves are used to determine the equivalent interfacial traction-separation laws or $\tau=\tau(w)$ at different adhesive thicknesses. A characteristic strain energy release rate J_0 is defined as the J value when the crack starts propagating immediately after the maximum fracture load P_{cr} is reached.

It can be seen that J_0 is generally smaller than the critical strain energy release rate or the fracture energy J_{IIC}, which reflects that the strain energy release rate J_{II} keeps increasing after the crack propagation. This is because the plastic dissipation (or plastic zone) can be further increased after the crack initiation.

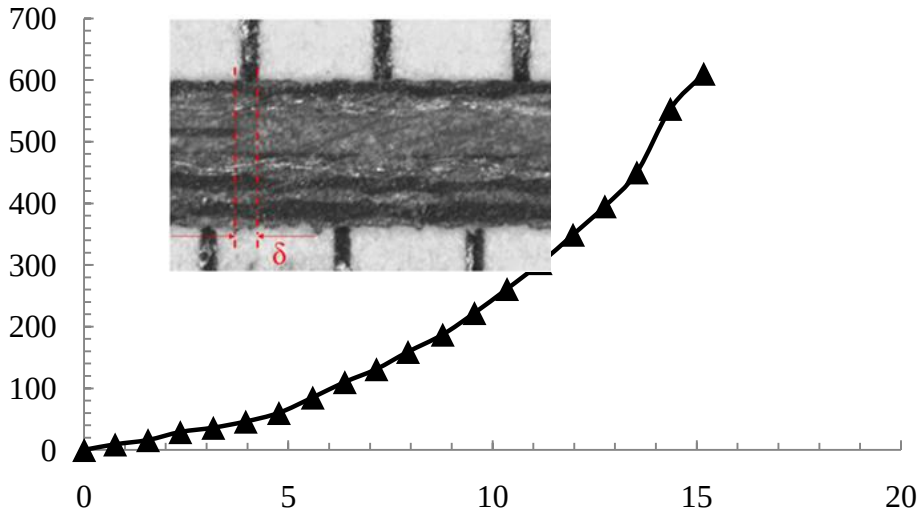

Figure 5.2.2: A typical relationship between loadline displacement Δ and local crack tip slip *w* for Group 3 (h_a=0.4 mm)

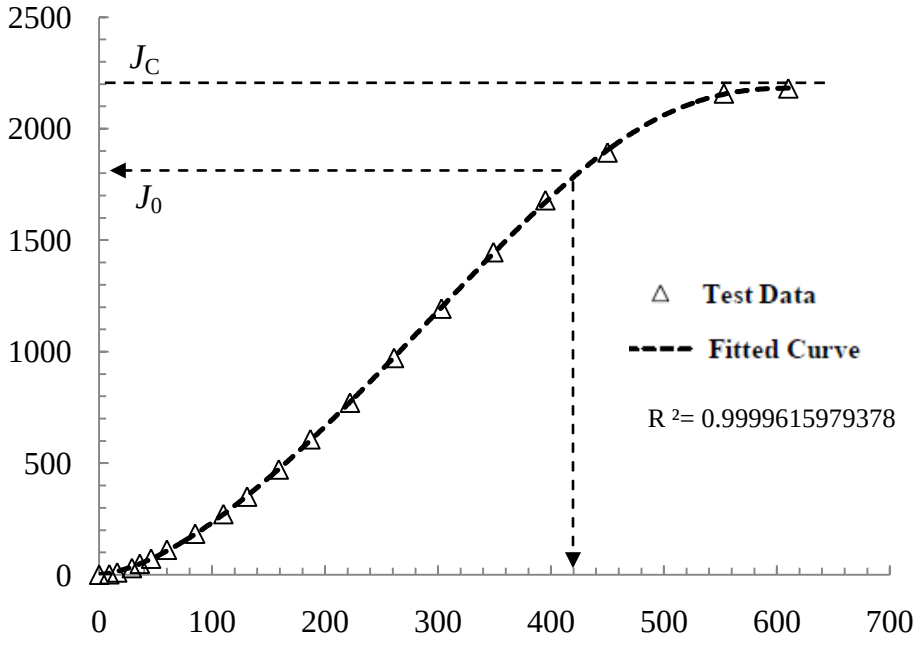

Figure 5.2.3: A typical relationship between energy release rate J and local crack tip slip w for Group 3 (ha=0.4 mm)

In this study, the crack initiation and propagation process were recorded by using the high resolution CCD camera. It was observed that the initial crack tip started opening as the shear load increased. It was also observed that the whiting zone appeared near the initial crack tip and was becoming more visible as the load was increased, as shown in Fig. 5.2.4. It was believed that the whiting zone consisted of numerous microcracks. When a lot of micro cracks were merged together and formed a macro crack, the initial crack started to propagate with the continuously increasing load, as shown in Fig. 5.2.5. Based on Eq. (2-44), these experimental *J*-*w* curves are used to determine the equivalent interface cohesive laws or $\tau=\tau(w)$ at different adhesive thicknesses. Fig. 5.2.6 gives a typical shear stress vs. local slip displacement curve (a specimen in group 3 with thickness of 0.4 mm).

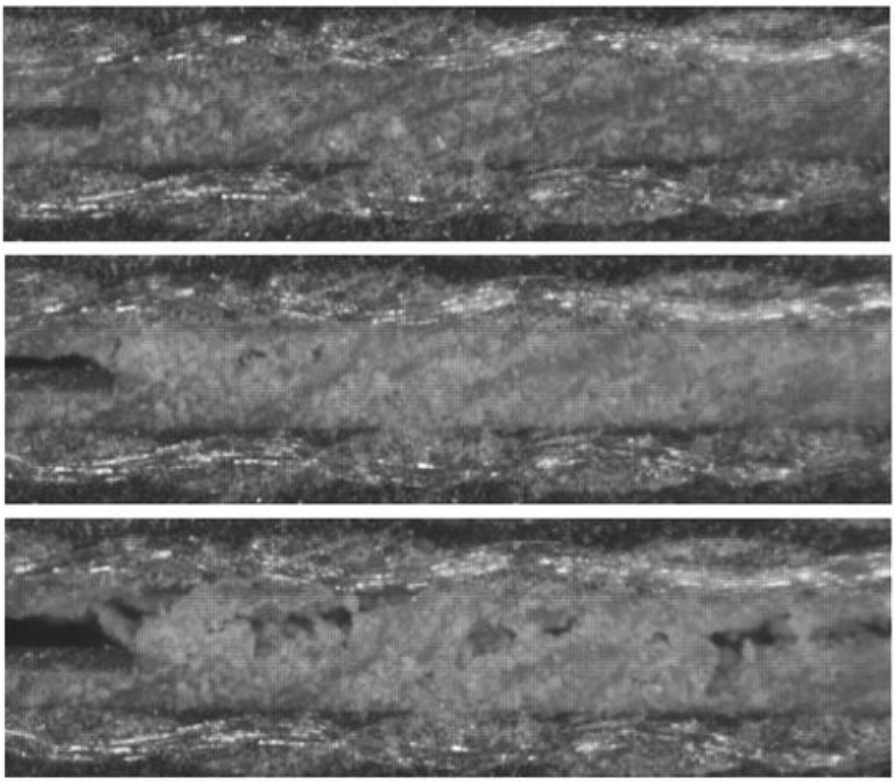

Figure 5.2.4: Local damage, fracture and deformation in the bondline

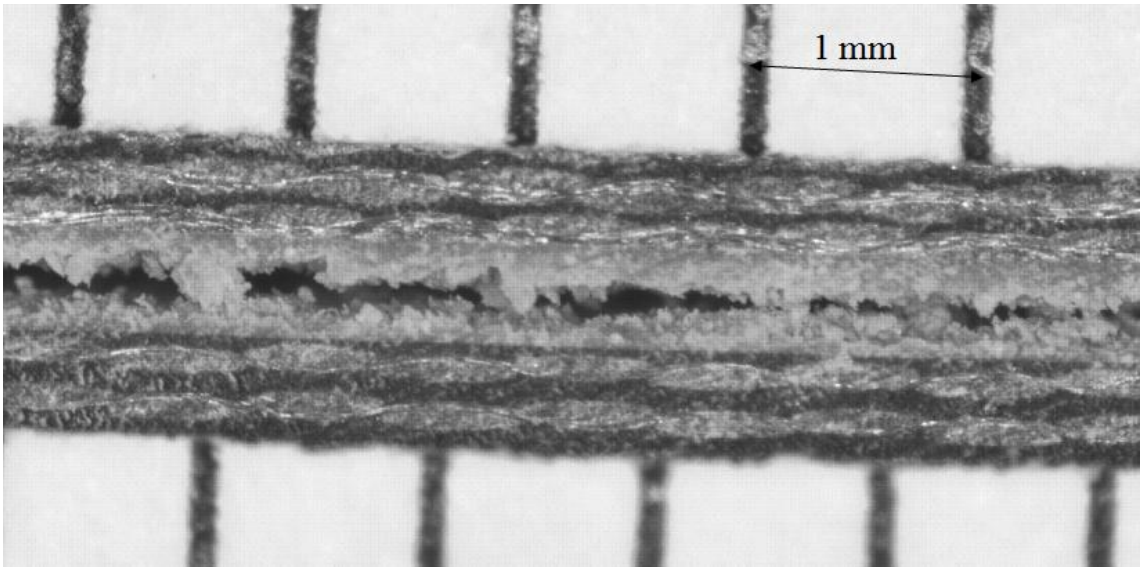

Figure 5.2.5 Crack propagates during the test

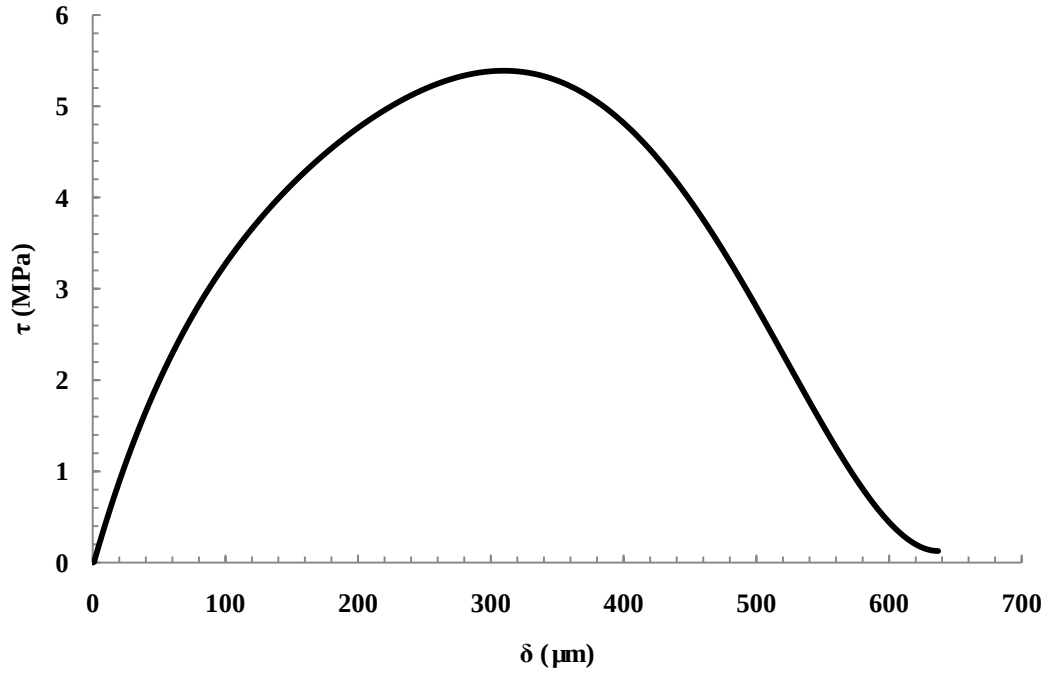

Figure 5.2.6: Typical interface constitutive relationship (equivalent cohesive law) for Group 3 (h_a=0.4 mm)

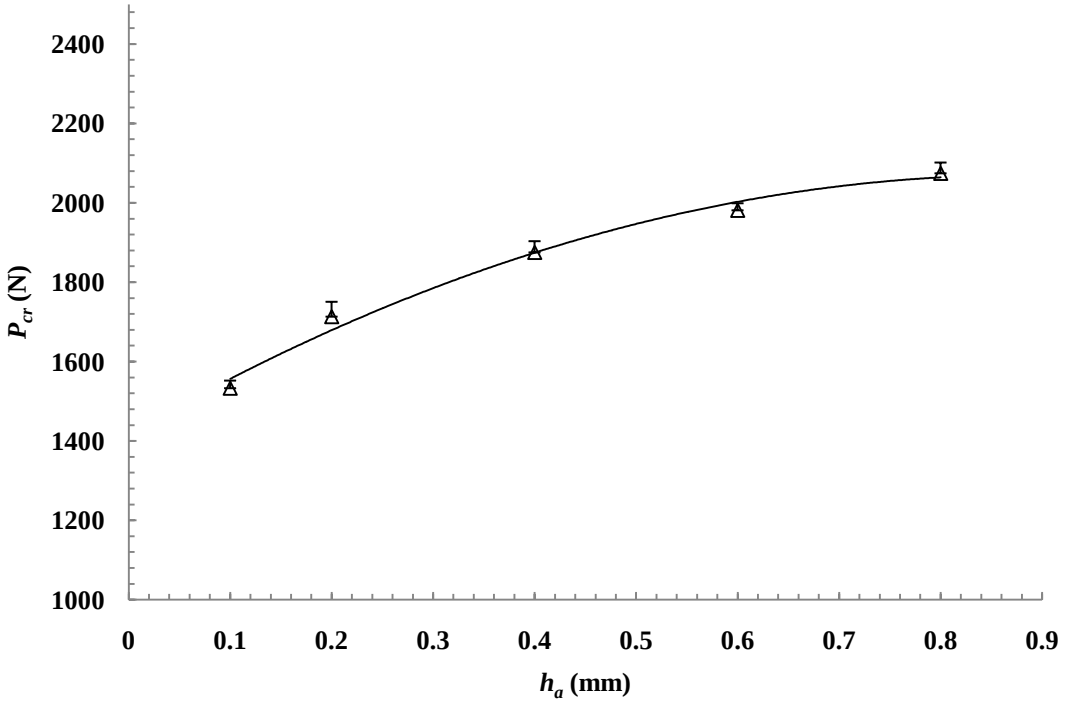

Figure 5.2.7: The average maximum load P_{cr} at different adhesive thicknesses h_a

5.2.2 Effects of the Thickness of the Adhesive Layer

With the global experiment results for different groups, the maximum peel loads are plotted as a function of the adhesive thicknesses (0.1 mm, 0.2 mm, 0.4 mm, 0.6 mm, and 0.8 mm) as shown in Fig. 5.2.7 It can be observed that the average peak load is increased from 1532.873N (Group 1) to 2074.183N (Group 5) when the thickness of adhesive layer increases from 0.1 mm to 0.8 mm. However, the rate of increase in the peak load reduces as the adhesive layer thickness increases, as shown by the trend line in Fig. 5.2.7.

The estimated average fracture energy J_C and the average characteristic J_0 (at the maximum peel load) were plotted as a function of the adhesive thickness in Fig. 5.2.8 (0.1 mm, 0.2 mm, 0.4 mm, 0.6 mm and 0.8 mm). As shown in Fig. 5.2.8, the fracture energy J_C of the bonded joints is plotted as a function of the adhesive thickness.

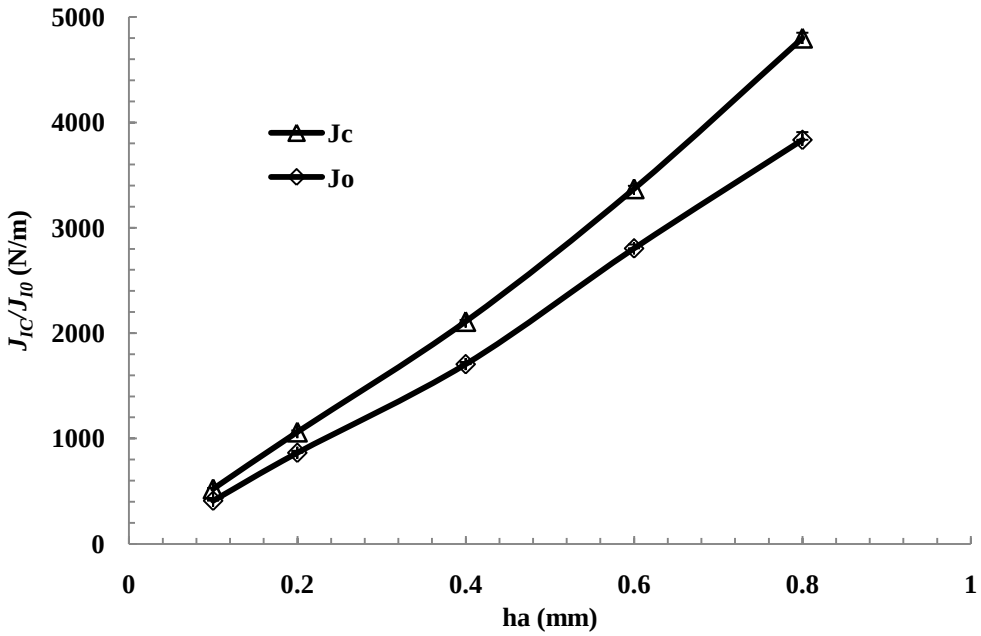

Figure 5.2.8: The estimated fracture energy J_C and the characteristic energy release rate J_0 (corresponding to P_{cr}) with different adhesive thicknesses h_a

The fracture energy J_C at the thickness of 0.1 mm is increased by approximately 825% when the adhesive thickness becomes 0.8 mm. This significant increase in fracture energy can explain the increase in load capacity when the adhesive thickness is increased.

The significant increase in J_0 and J_C are responsible for the increased load capacity when the adhesive thickness becomes thicker. Meanwhile, one may see that when the adhesive thickness is thin, J_0 and J_C are relatively close to each other. When it is relatively thick, J_0 and J_C are relatively departed.

After data collecting and curve-fitting process of the experimental J-w curves, by applying Eq. (2-44), one can see that the interfacial traction-slip laws are determined by numerically differentiating the experimental J-w curves. A typical equivalent interfacial law of each group is given in Fig. 5.2.9 at different bondline thicknesses. One may see

the five specimens in each group (each adhesive thickness) present fairly consistent results.

One may see that the effects of the bondline thickness on the interfacial traction-slip laws. First, the interfacial strength increases for laminate composite ENF joint with the increase of the bondline thickness. Second, the initial stiffness of the interfacial laws (the initial slope of the τ-w curve) is identical for laminate composite ENF joints with various bondline thicknesses, which suggests that the shear deformation is controlled by the adhesive layer. Finally, the fracture energy (the total area under the w-τ curve) increases with the bondline thickness.

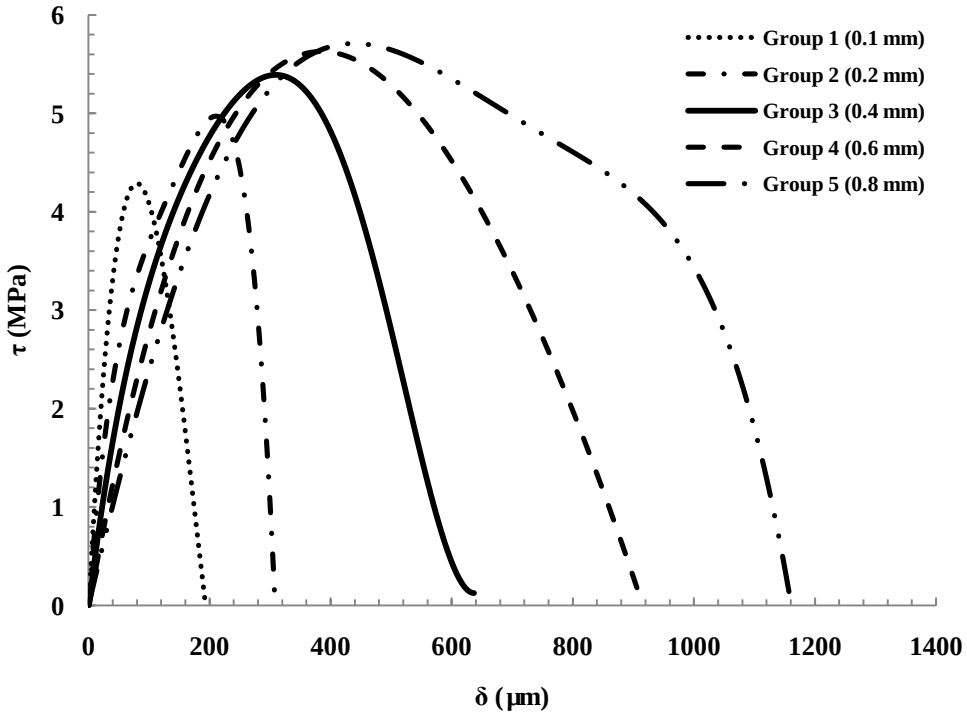

Figure 5.2.9: Typical shapes of the interfacial traction-slip laws of bonded steel with different bondline thicknesses h_a

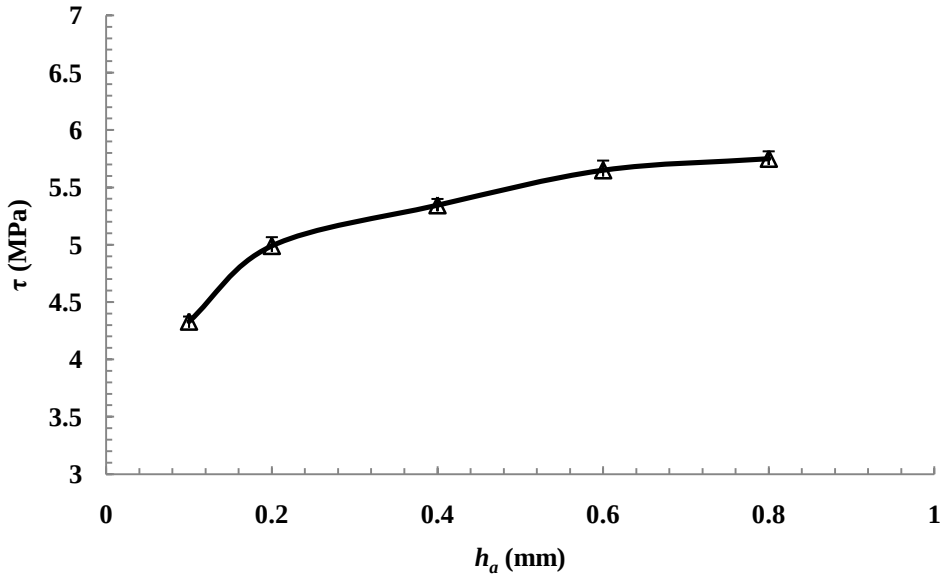

Figure 5.2.10: The effect of adhesive thickness on the maximum interface stress τ_f

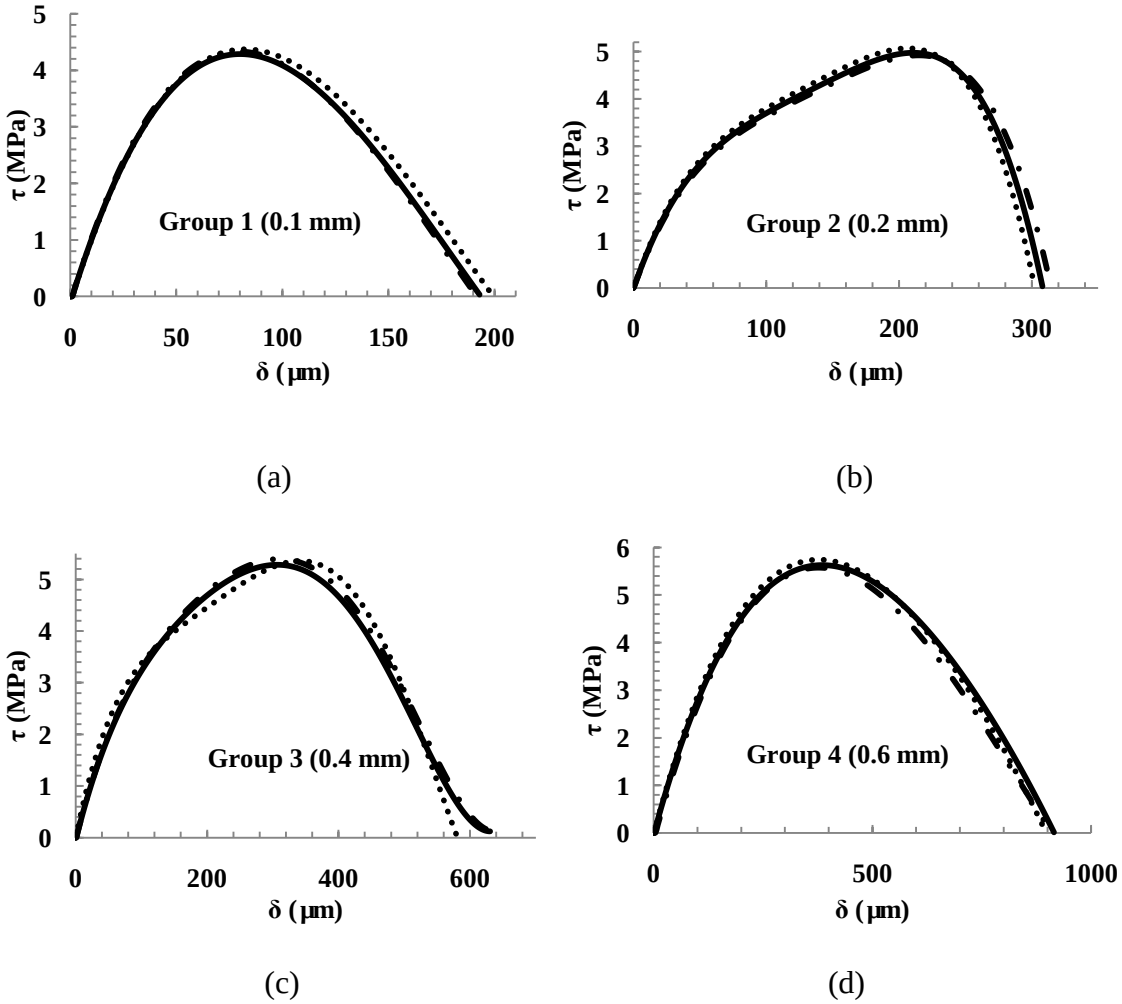

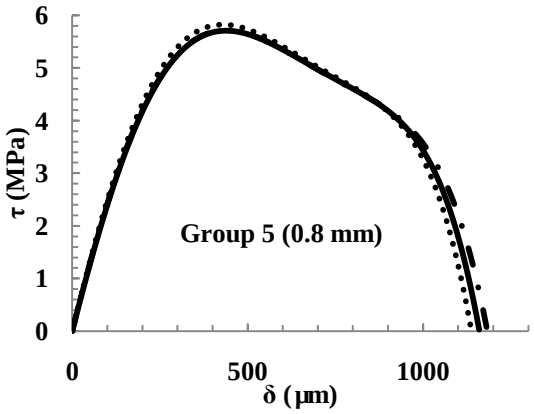

(e)

Figure 5.2.11: The shapes of all interfacial traction-slip laws with different thicknesses of bondline: (a) bondline thickness h_a=0.1 mm; (b) bondline thickness h_a=0.2 mm; (c) bondline thickness h_a=0.4 mm; (d) bondline thickness h_a=0.6 mm; (e) bondline thickness h_a=0.8 mm

The average interfacial strength τ_{max} of the five groups (with error bar) are plotted as a function of the adhesive thickness in Fig. 5.2.10. According to the manufacturer, the shear strength of the adhesive material is approximately 6.6 MPa (when the thickness is 0.75 mm with laminated composite adherends). One can see that the interfacial strength was 5.8 MPa at the thickness of 0.8 mm, which is approximately the yield shear strength of the bulk adhesive material. Finally, the complete fifteen interfacial traction-separation laws of the bonded laminate composite ENF joints (three specimens in each of the five groups at various bondline thicknesses) are given in Fig. 5.2.11. One may see the fairly consistent results of the three specimens in each group at various bondline thicknesses.

CHAPTER 6

RESULTS AND DISCUSSION OF MIXED MODE I AND MODE II TEST

This chapter includes two parts: one is the results and discussion based on the mixed Mode I/II test data of steel adherends specimens; the other is based on the data of laminated composite specimens.

6.1 Test Results and Discussions of Mixed Mode I/II with Steel Based Specimen

6.1.1 Global and Local Test Results

The geometric parameters of each specimen are given in Table 6.1.1. A typical force vs. displacement curve (a specimen in ha=0.1mm with an initial crack length a=80mm) at the loading point is shown in Fig.6.1.1.

Table 6.1.1 Geometry of specimens

Average adhesive thickness (mm)	Length (mm)	Height (mm)	Width (mm)	Initial Crack Length (mm)	Initial Crack Length (mm)	Initial Crack Length (mm)
0.1	254.10	6.35	25.41	20.06	50.12	80.11
0.2	254.11	6.35	25.44	20.11	50.22	79.95
0.4	254.09	6.34	25.42	20.09	50.18	80.21
0.6	254.08	6.35	25.39	20.13	50.44	80.05
0.8	254.10	6.36	25.46	20.12	50.37	80.14

The force linearly increased until the local damage occurs. The load nonlinearly increases until the crack initiation process is completed. After that, the crack tip starts propagating. A continuous drop in the bending force was seen as the crack continuously propagated until the crack reached the specimen's end.

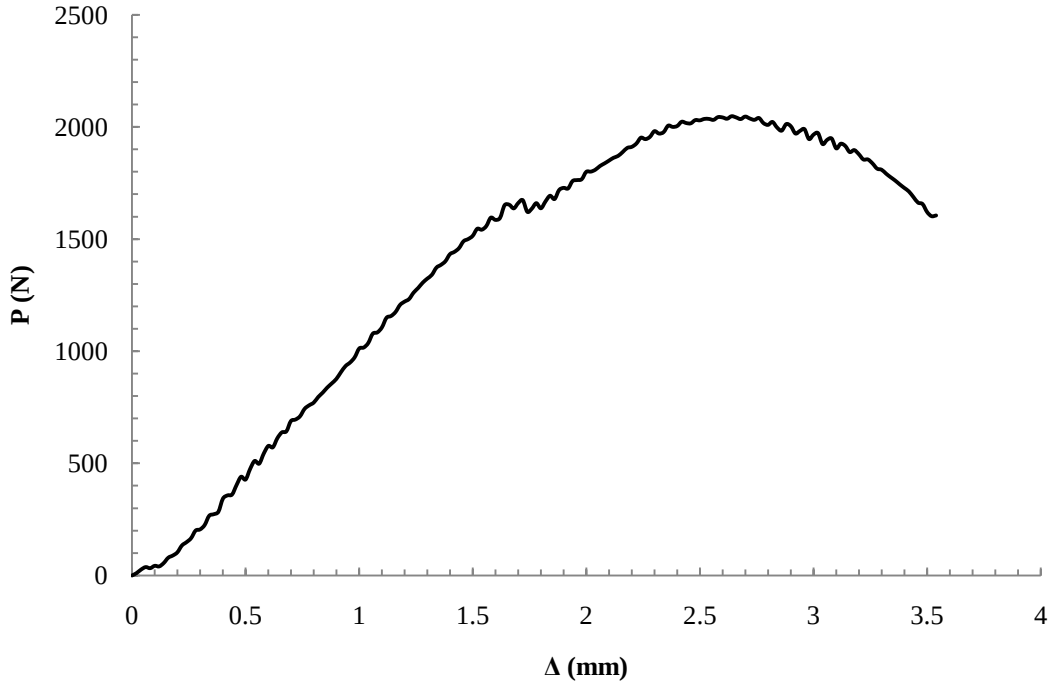

Figure 6.1.1: A typical relationship between loadline displacements Δ and loadline bending force *P* for h_a=0.1mm with initial crack length a=80mm

The data of the rotation angel at the loading point were collected by the inclinometer. With Eq. (2-50), the experimental energy release rate J is determined by combining the measured θ_P and P. A typical relationship (a specimen in ha=0.1mm with initial crack length of 20mm) between global energy release rate J and loadline displacement Δ is given in Fig. 6.1.2. In a real test, we found that it was fairly difficult to exactly define when the initial crack tip was propagated. Therefore, a characteristic strain energy release rate J_0 was defined which represented the J value when the maximum peel force P was reached. Note that with the growth of the crack, the global strain energy release rate keeps increasing as shown in Fig. 6.1.2 (J-Δ curve). This implies that the plastic dissipations beyond the crack tip must keep increasing during this stable growth process. However, the increase of J becomes slower and slower as the crack grows, which seems nearly stable even by the end of the test. Therefore, an approximate

asymptote is added in Fig. 6.1.2 to estimate the interfacial toughness of the bonded joints. And this estimated asymptotic value is denoted by J_C or fracture energy.

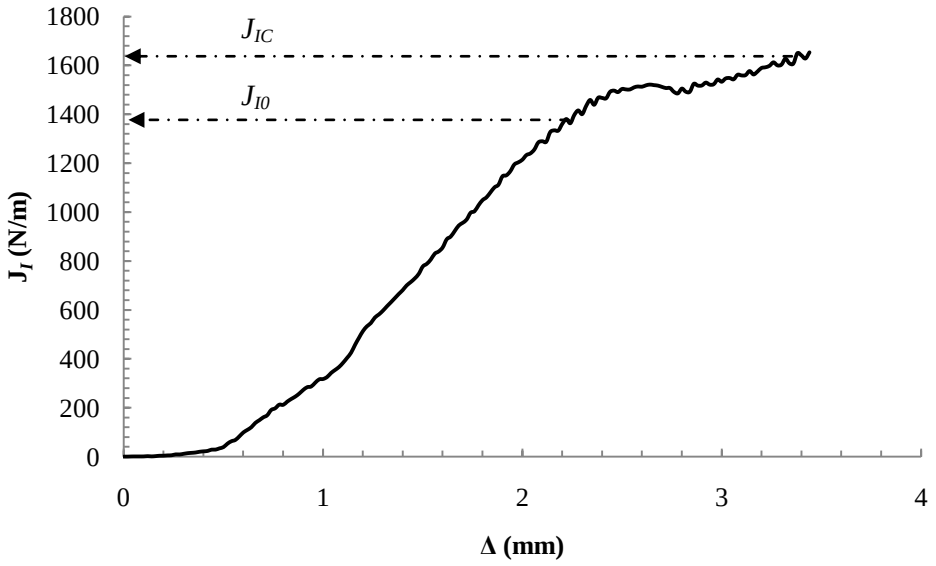

Figure 6.1.2: A typical relationship between loadline displacements Δ and energy release rate *J* for specimen with ha=0.1mm (*a*=20mm)

In this study, crack tip local deformations along the entire adhesive layer were recorded using the high resolution CCD camera. The value of the crack tip separation δ was measured as the relative normal displacement between the two steel adherends at the location of initial crack tip through the recorded digital images. By combining J_I-δ curve and crack tip separation δ, a typical experimental J_I-δ curve was obtained as shown in Fig. 6.1.3 (a specimen ha=0.1mm with initial crack length of 80mm). With Eq. (2-51), the experimental J_I-δ curves were used to determine the equivalent interfacial traction-separation laws or σ=σ(δ), as show in Fig. 6.1.4.

It was observed that the initial crack tip started opening as the shear load increased. It was also observed that the whiting zone appeared near the initial crack tip and was becoming more visible as the load was increased, as shown in Fig. 6.1.5 (circle area).

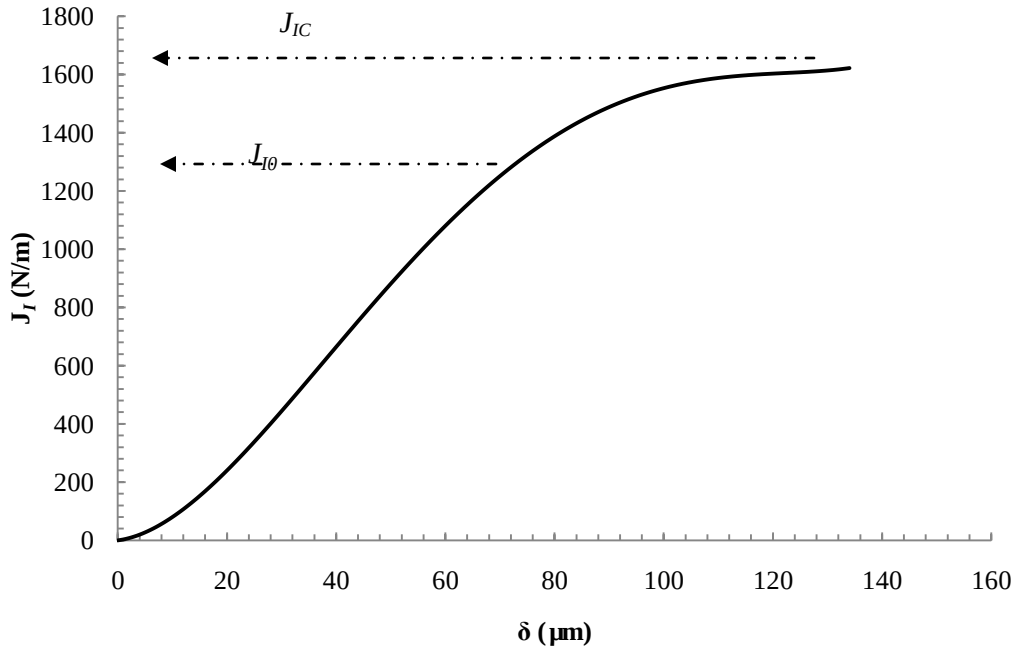

Figure 6.1.3: A typical relationship between energy release rate *J* and local crack tip separation *δ* for specimen with ha=0.1mm (a=80mm)

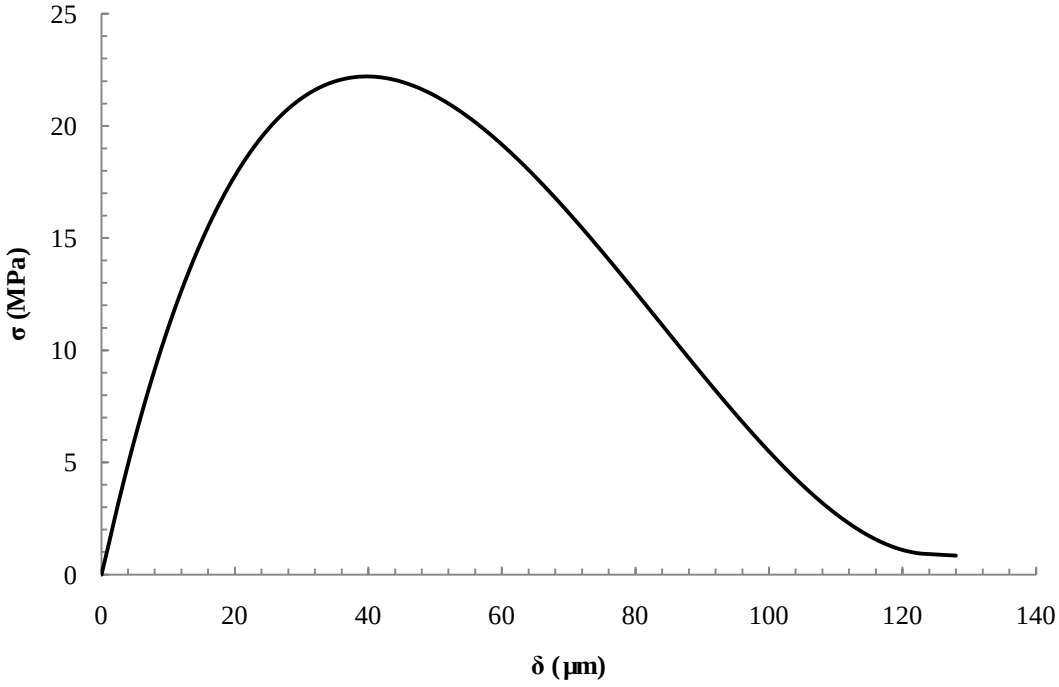

Figure 6.1.4: A typical shape of the equivalent interfacial traction-separation laws with ha=0.1mm (a=80mm) adhesive layer

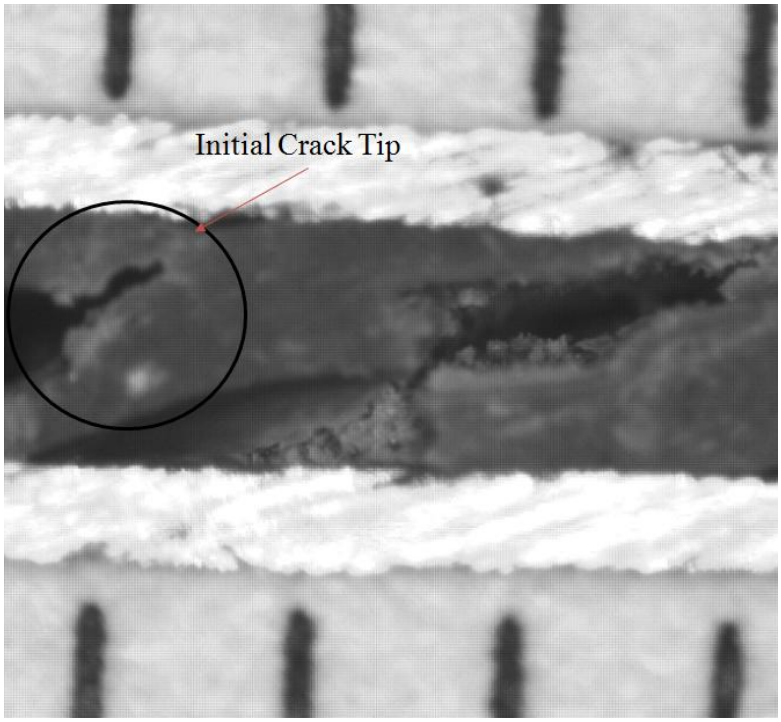

Figure 6.1.5: Local damage, fracture and deformation in the bondline

The value of the shear slip δ between the two adherends at the location of the initial crack tip is calculated based on the digital images. By combining P-Δ curve and local shear slip δ, according to Eq.(2-46), a typical experimental J_{II}-w curve is obtained as shown in Fig. 6.1.6 (a specimen in ha=0.1mm with initial crack length 80mm). With Eq. (2-49), the experimental J_{II}-w curves are used to determine the equivalent interfacial traction-separation laws or $\tau=\tau(w)$ at different adhesive thicknesses. A characteristic strain energy release rate J_0 is defined as the J value when the crack starts propagating immediately after the maximum fracture load P_{cr} is reached. It can be seen that J_0 is generally smaller than the critical strain energy release rate or the fracture energy J_{IIC}, which reflects that the strain energy release rate J_{II} keeps increasing after the crack propagation. This is because the plastic dissipation (or plastic zone) can be further increased after the crack initiation.

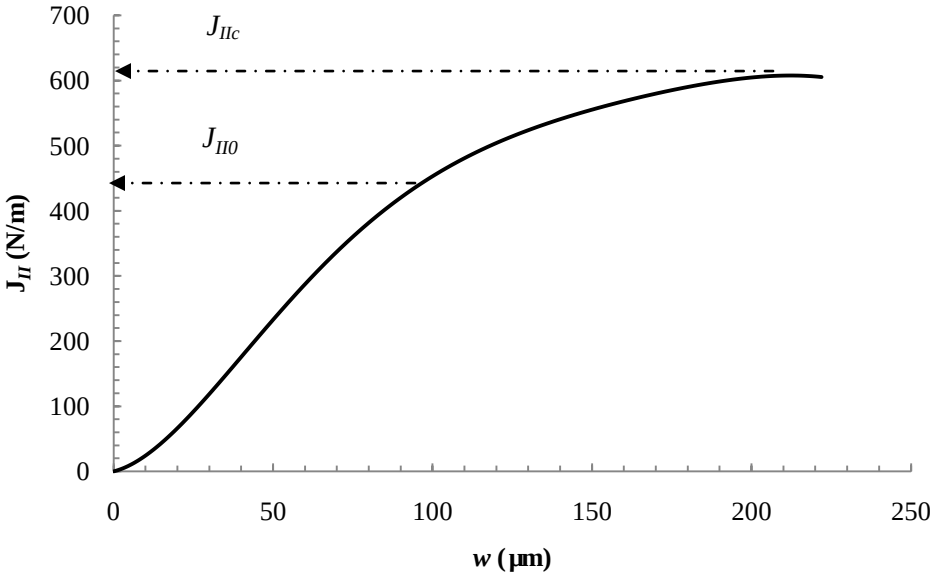

Figure 6.1.6: A typical relationship between energy release rate J and local crack tip slip δ for specimen with ha=0.1mm (a=80 mm)

Based on Eq. (2-47), these experimental J_{II}-w curves are used to determine the equivalent interface cohesive laws or $\tau=\tau(w)$ at different adhesive thicknesses. Fig. 6.1.7 gives a typical shear stress vs. local slip displacement curve (a specimen in ha=0.1mm with initial crack length of 80mm).

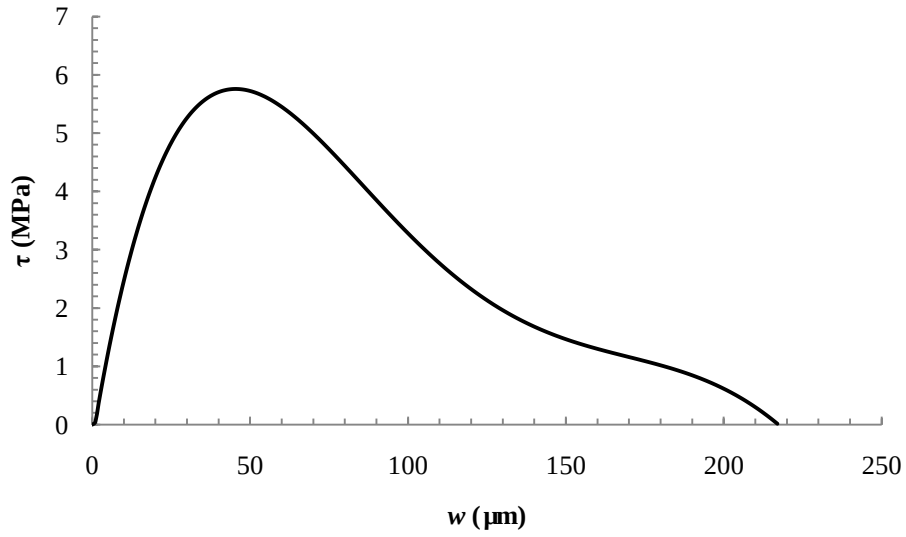

Figure 6.1.7: Typical interface constitutive relationship (equivalent cohesive law) for specimen with h_a=0.1 mm (a=80mm)

6.1.2 Effects of the Thickness of the Adhesive Layer

With the global experiment results for different groups, the maximum bending loads are plotted as a function of the adhesive thicknesses (0.1 mm, 0.2 mm, 0.4 mm, 0.6 mm, and 0.8 mm) as shown in Fig. 6.1.8. It can be observed that the average peak load is increased from 3417.67 N to 4791.10 N when the thickness of adhesive layer increases (from 0.1 mm to 0.8 mm), as shown by the trend line in Fig. 6.1.8.

The increase of the adhesive layer thickness might increase the bending stiffness of the specimen. However, this contribution is very small since the adherends were made of low carbon steel with a much higher thickness of 6.35 mm and much higher bending stiffness. The estimated average fracture energy J_{IC}, J_{IIC} and the average characteristic J_{I0}, J_{II0} (at the maximum peel load) were plotted as a function of the adhesive thickness in Fig. 6.1.9 and Fig. 6.1.10 (0.1 mm, 0.2 mm, 0.4 mm, 0.6 mm and 0.8 mm). The significant increase in J_0 and J_C are responsible for the increased load capacity when the adhesive thickness becomes thicker. Meanwhile, one may see that when the adhesive thickness is thin, J_0 and J_C are relatively close to each other. When it is relatively thick, J_0 and J_C are relatively departed. After data collecting and curve-fitting process of the experimental J-δ curves, by applying Eq. (2-51), one can see that the interfacial traction-slip laws are determined by numerically differentiating the experimental J-δ curves.

A typical equivalent interfacial law of each group is given in Fig. 6.1.11 and Fig. 6.1.12 at different bondline thicknesses with initial crack length a=20mm. One may see that the effects of the bondline thickness on the interfacial traction-slip laws.

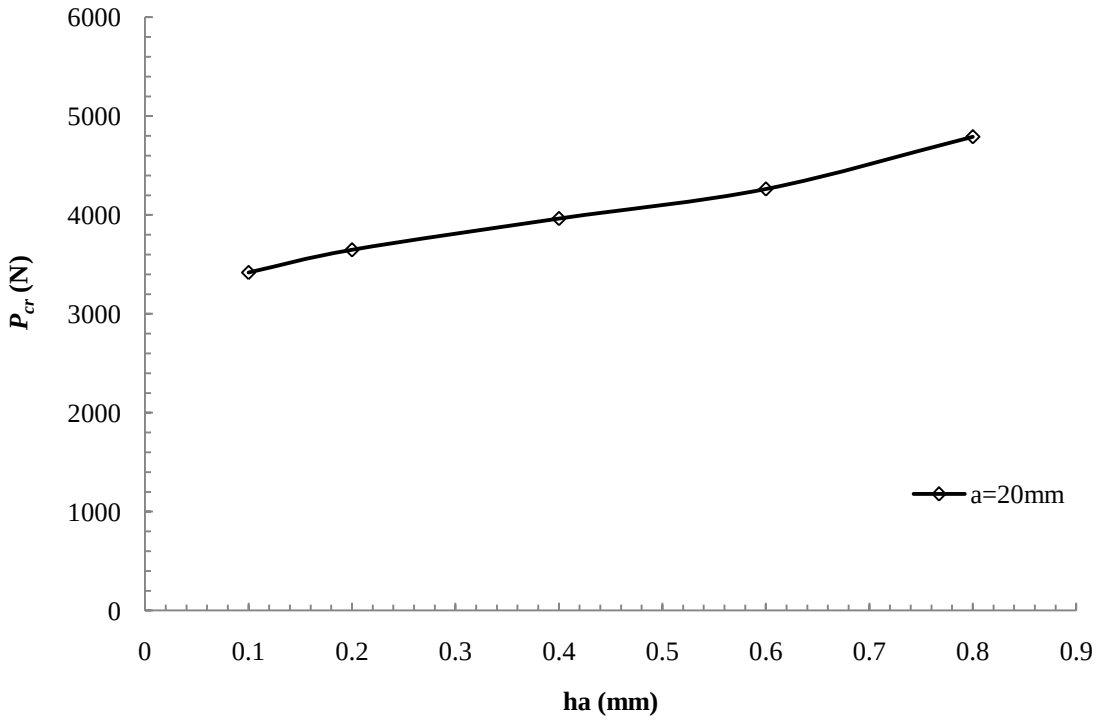

Figure 6.1.8: The average maximum shear load P_{cr} at different adhesive thicknesses h_a

- **Mode I Portion**

After data collecting and curve-fitting process of the experimental *J*-δ curves, by applying Eq. (2-46), one can see that the interfacial traction-separation laws were determined by numerically differentiating the experimental *J*-δ curves. The cohesive law was calculated for each specimen. The typical equivalent cohesive law of each group is given in Fig.6.1.11 at different adhesive thicknesses. From Fig. 6.1.11, one can see that three major effects of the adhesive thickness. First, the local characteristic separation (δ_0) corresponding to the interfacial strength $\sigma_{\max}$, decreases with the decrease of the adhesive thickness. Second, the interfacial strength increases with the decrease of the adhesive thickness. Finally, the total area under the δ-σ curve, which represents the strain energy release rate at crack propagation, increases with the increase of the adhesive thickness.

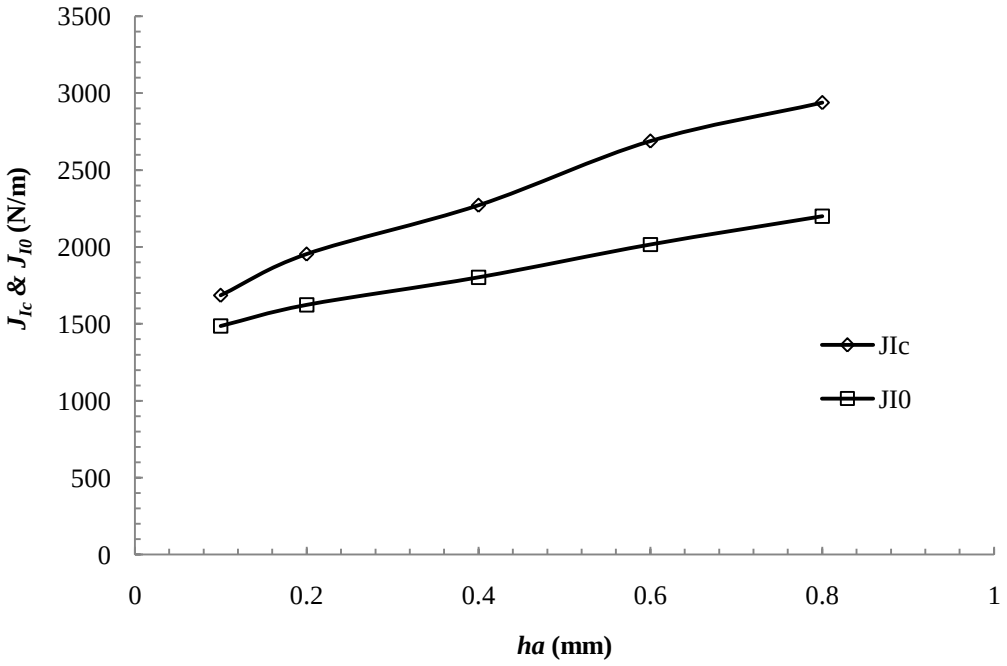

Figure 6.1.9: The estimated fracture energy J_{IC} and the characteristic energy release rate J_{I0} (corresponding to P_{cr}) with different adhesive thicknesses (a=20mm)

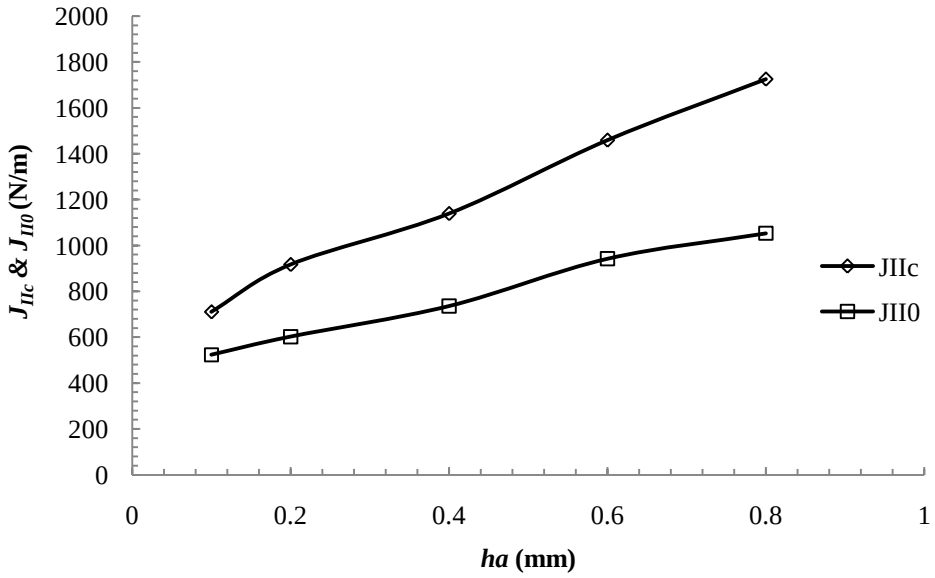

Figure 6.1.10: The estimated fracture energy J_{IIC} and the characteristic energy release rate J_{II0} (corresponding to P_{cr}) with different adhesive thicknesses (a=20mm)

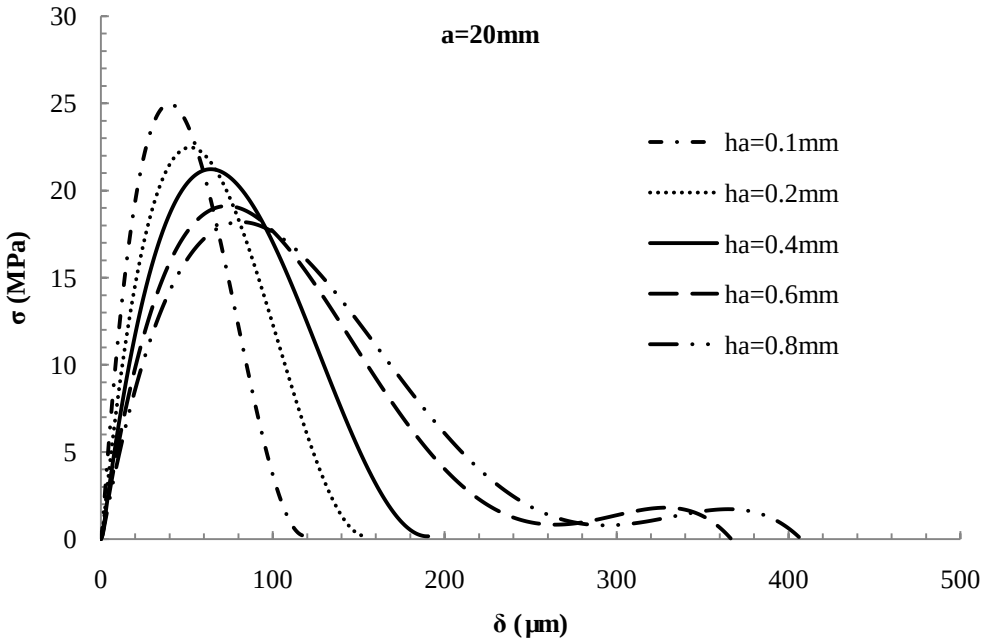

Figure 6.1.11: Typical shapes of the interfacial traction-separation laws of bonded steel with different bondline thicknesses h_a (a=20mm)

- **Mode II Portion**

First, the interfacial strength increases for steel joint with the increase of the bondline thickness. Second, the initial stiffness of the interfacial laws (the initial slope of the τ-w curve) is identical for steel joints with various bondline thicknesses, which suggests that the shear deformation is controlled by the adhesive layer. Finally, the fracture energy (the total area under the w-τ curve) increases with the bondline thickness. As shown in Fig. 6.1.10, the fracture energy J_{IIC} of the bonded joints is plotted as a function of the adhesive thickness. The fracture energy J_{IIC} at the thickness of 0.1 mm is increased by approximately 143% when the adhesive thickness becomes 0.8 mm. This significant increase in fracture energy can explain the increase in load capacity when the adhesive thickness is increased.

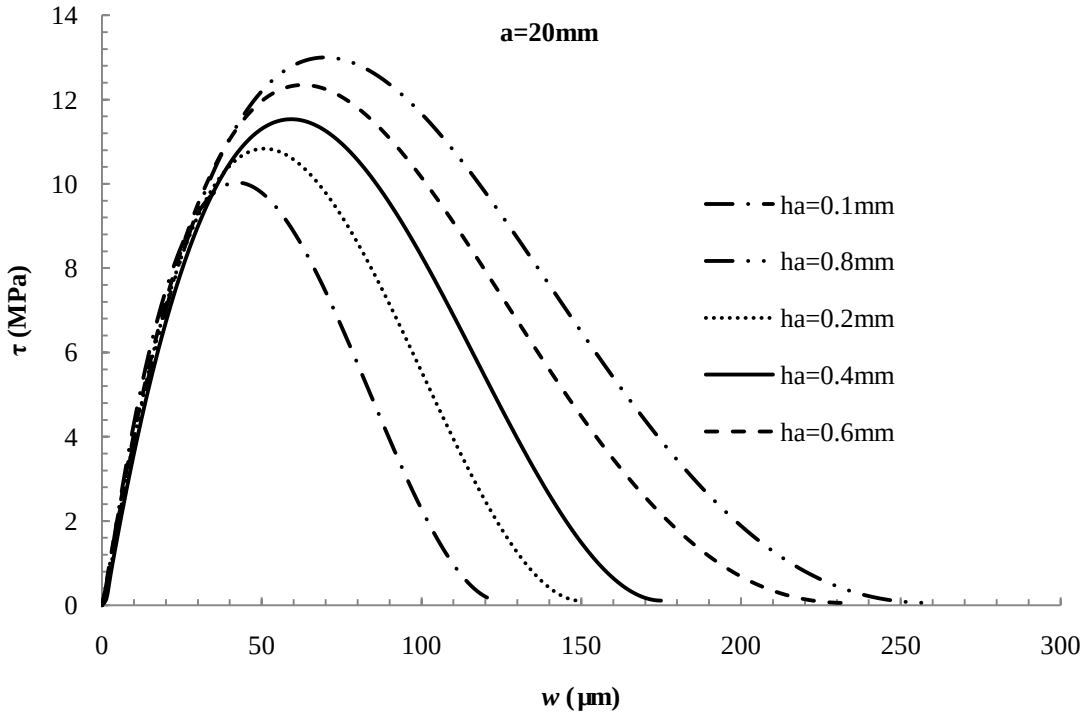

Figure 6.1.12: Typical shapes of the interfacial traction-slip laws of bonded steel with different bondline thicknesses h_a (a=20mm)

- **Mode Mixities**

The ratio of the estimated fracture energy J_{IIC} and total fracture energy (J_{IC} +J_{IIC}) with different adhesive thickness was plotted in Fig. 6.1.13. The ratio of the shear strength and total strength with different adhesive thickness was plotted in Fig. 6.1.14. It is observed that the ratio of the estimated fracture energy J_{IIC} and the ratio of the shear strength were increased with the thickness of adhesive layer increased. It is indicated that the ratio of mode I within the mixed mode I/II was decreased as the thickness of adhesive layer increased. The stiffness of the adhesive layer is much lower than the stiffness of the adherends. Therefore, as the thickness of adhesive layer increased, the plastic dissipation increased.

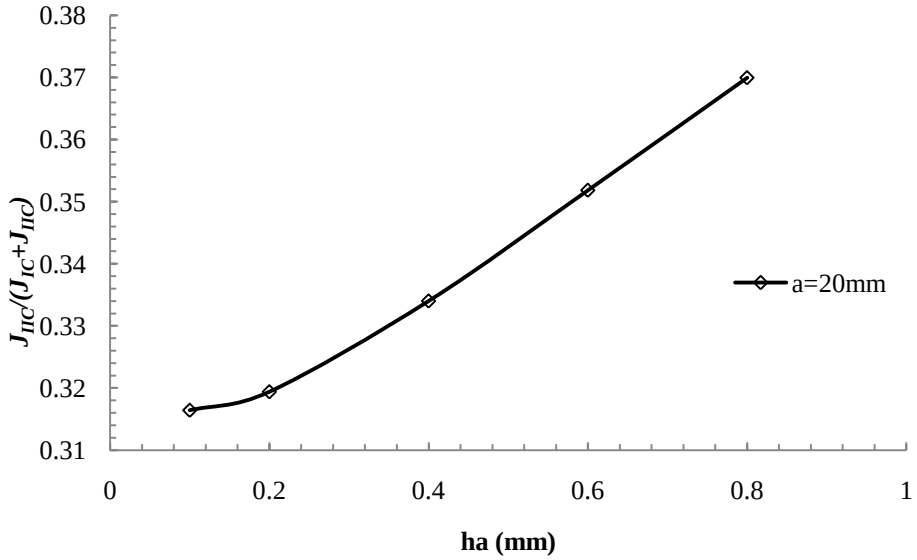

Figure 6.1.13: The ratio of the estimated fracture energy J_{IIC} and total fracture energy (J_{IC} + J_{IIC}) with different adhesive thicknesses (a=20mm)

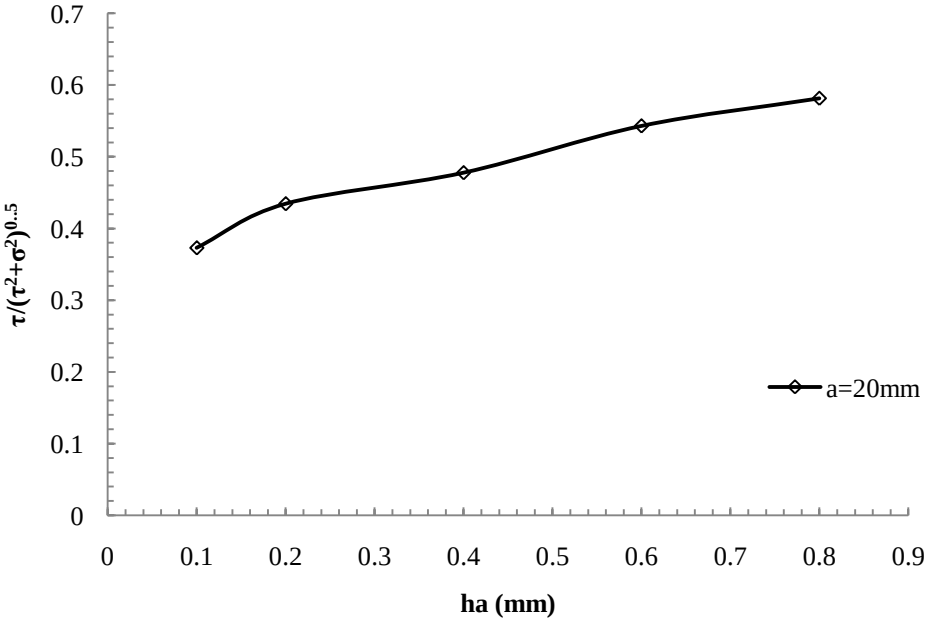

Figure 6.1.14: The ratio of the shear strength and total strength with different adhesive thicknesses (a=20mm)

6.1.3 Effects of the Initial Crack Tip Length of Adhesive Layer

In this study, the effects of the initial crack tip length of the adhesive layer were also considered with different thickness of adhesive layer. Three different initial crack length a=20mm, 50mm, and 80mm were selected in this study.

The maximum load P_{cr} at each initial crack length with different thickness of adhesive layer was plotted in Fig. 6.1.15. It is observed that the maximum load was decreased as the initial crack length increased; the maximum load was increased as the thickness of adhesive layer increased at each initial crack length. As the initial crack length increased at the same thickness of adhesive layer, the bending moment was increased at the initial crack tip. It caused that peeling force increase near the crack tip area at the same time. In other words, the mode I portion was increased as the initial crack length increased.

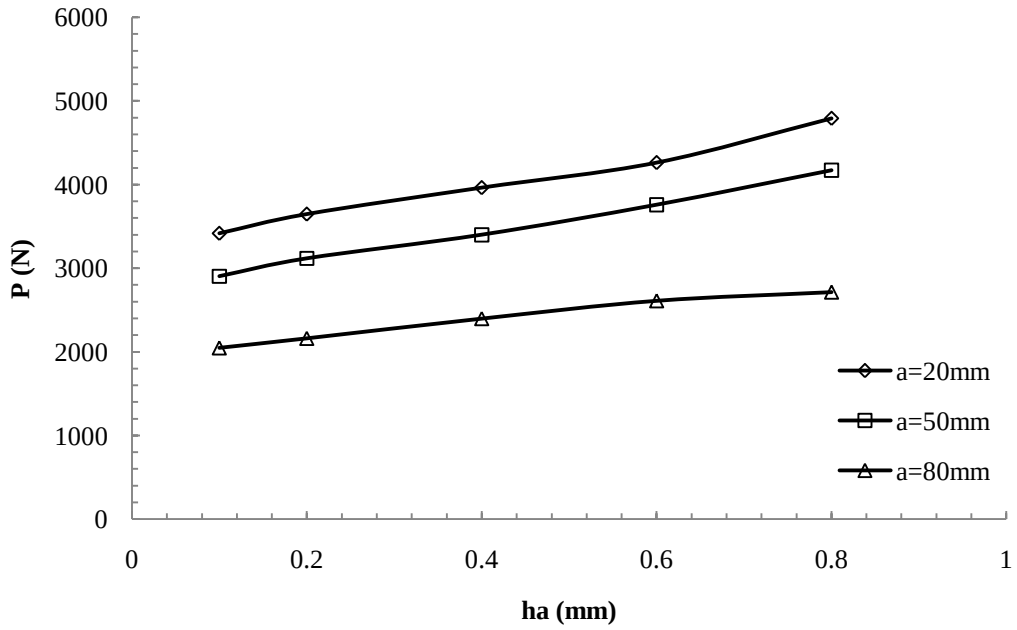

Figure 6.1.15: The average maximum shear load P_{cr} at different initial crack length with different adhesive thicknesses h_a

The estimated fracture energy J_{IC} and J_{IIC} at each initial crack length with different adhesive thickness were plotted in Fig. 6.1.16 and Fig. 6.1.17. It is observed that the J_{IC} and J_{IIC} were increased at each initial crack length with different thickness of adhesive layer.

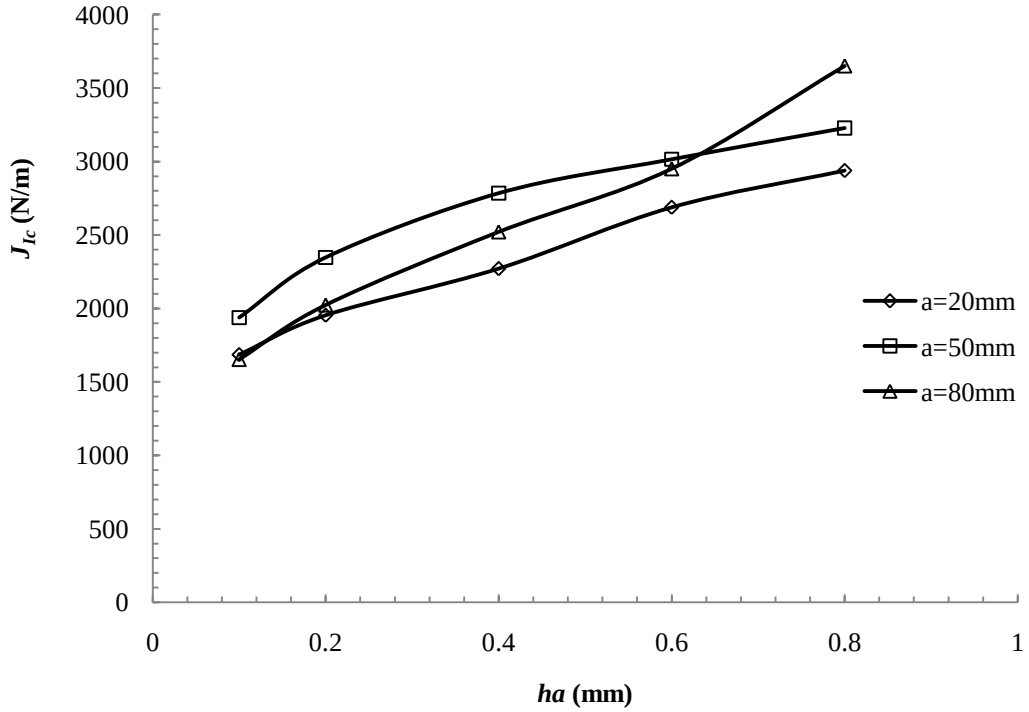

Figure 6.1.16: The estimated fracture energy J_{IC} at each initial crack length with different adhesive thicknesses

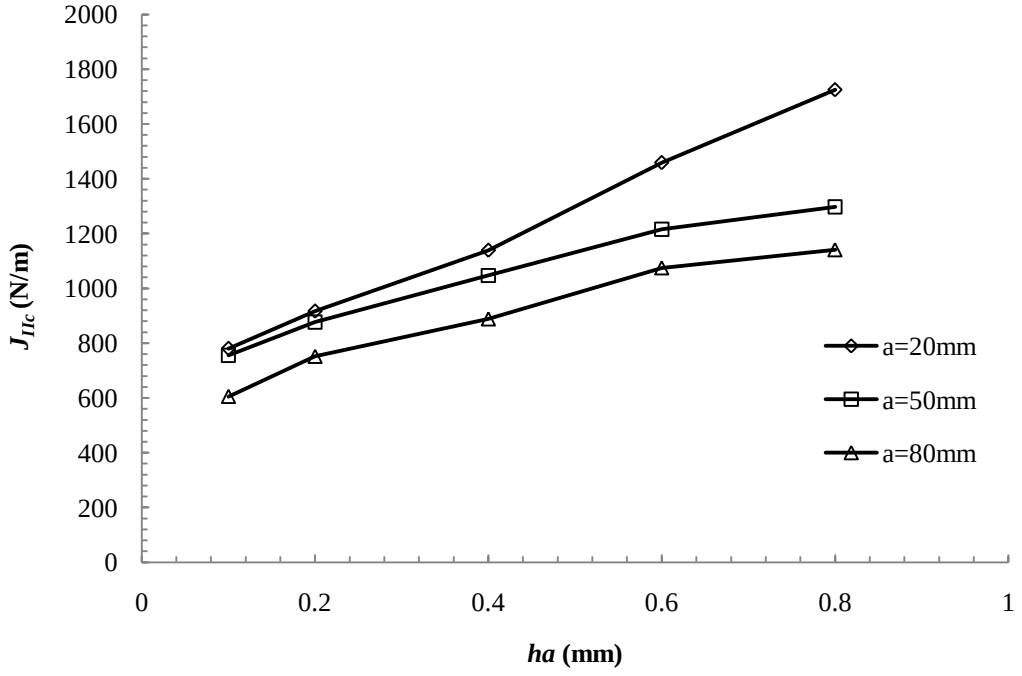

Figure 6.1.17: The estimated fracture energy J_{IIC} at each initial crack length with different adhesive thicknesses

The J_{IIC} was decreased as the initial crack length increased with the same thickness of adhesive layer. It is understandable due to the decreased loading force with increased initial crack length. Additionally, as the thickness of the adhesive layer increased, the relative rotation angle between the two adherends increased and caused the increase in shear force. However, the J_{IC} was increased when the initial crack length was at 20mm and 50mm. When the initial crack length reached 80mm, the fracture energy trend line crossed the other trending lines with initial crack length at 20mm and 50mm. The phenomenon may be due to the combination effect of the thickness of the adhesive layer and initial crack length. This is a very interesting point.

When the thickness of the adhesive layer was 0.1mm, as the initial crack length increased, the mount of the adhesive material between the adherends decreased and the moment around the initial crack tip area increased. Additionally, the relative rotation angle between the two adherends increased and caused that the smallest peeling force can make the crack propagate, as shown in Fig. 6.1.15. According to Eq. (2-50): J_I=P*θ/4, although the loading force increased from 2047N to 3417N as the initial crack length decreased from 80mm to 20mm, the relative rotation angle decreased from 3.23rad to 1.97rad. As the thickness of the adhesive layer increased, the ratio of the increased relative rotation angle increased. It can be explained that why the increased ratio of J_{IC} with initial crack length a=80 is larger than the other two, as the thickness of adhesive layer increased.

Typical shapes of the interfacial traction-separation laws and traction-slip laws of the bonded steel with different bondline thickness were plotted in Fig.6.1.18 and Fig.6.1.19 (a=50mm), Fig.6.1.20 and Fig.6.1.21 (a=80mm). The interfacial strength σmax,

τmax at each initial crack length with different thickness of the adhesive layer were plotted in Fig. 6.1.22 and Fig. 6.1.23. For each initial crack length, first, the local characteristic separation (δ0) corresponding to the interfacial strength σmax decreased with the decrease of the adhesive thickness. Second, the interfacial strength increases with the decrease of the adhesive thickness. Finally, the total area under the δ-σ curve, which represents the strain energy release rate at crack propagation, increases with the increase of the adhesive thickness.

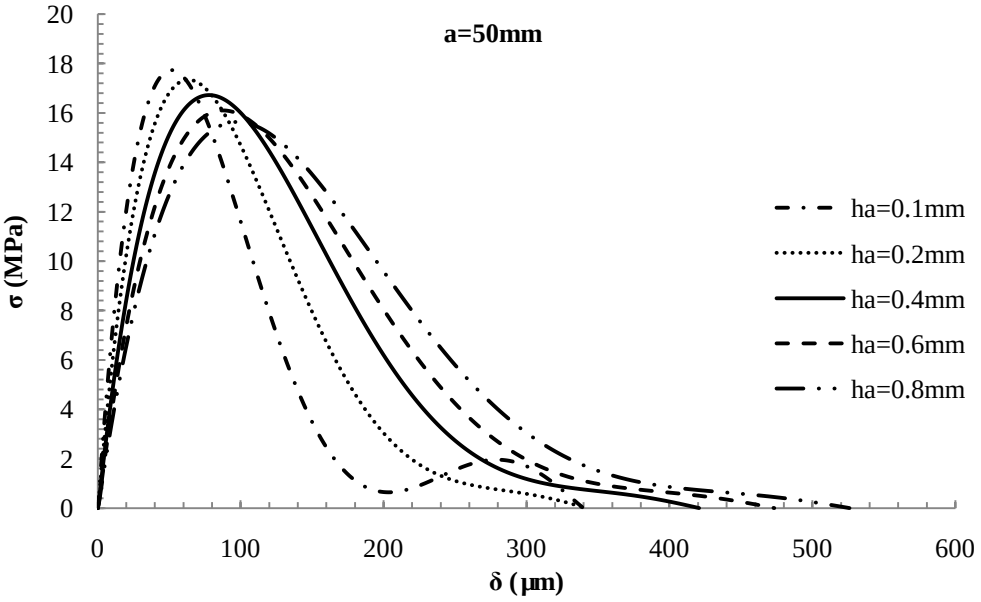

Figure 6.1.18: Typical shapes of the interfacial traction-separation laws of bonded steel with different bondline thicknesses h_a (a=20mm)

Additionally, the interfacial strength τ_{max} increases for steel joint with the increase of the bondline thickness. The initial stiffness of the interfacial laws (the initial slope of the τ-w curve) is identical for steel joints with various bondline thicknesses, which suggests that the shear deformation is controlled by the adhesive layer. The fracture energy (the total area under the w-τ curve) increases with the bondline thickness.

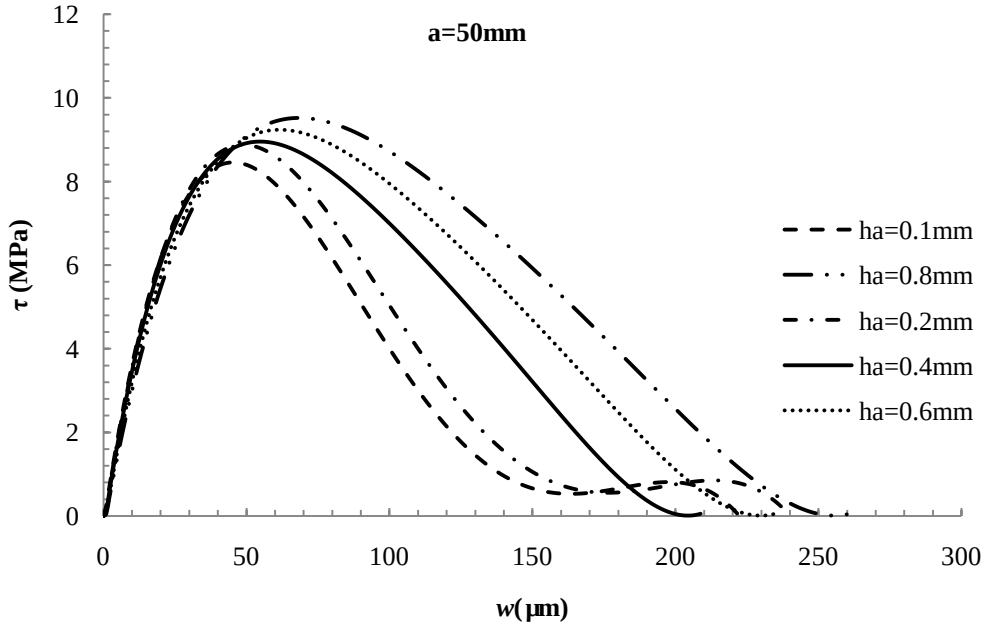

Figure 6.1.19: Typical shapes of the interfacial traction-slip laws of bonded steel with different bondline thicknesses h_a (a=20mm)

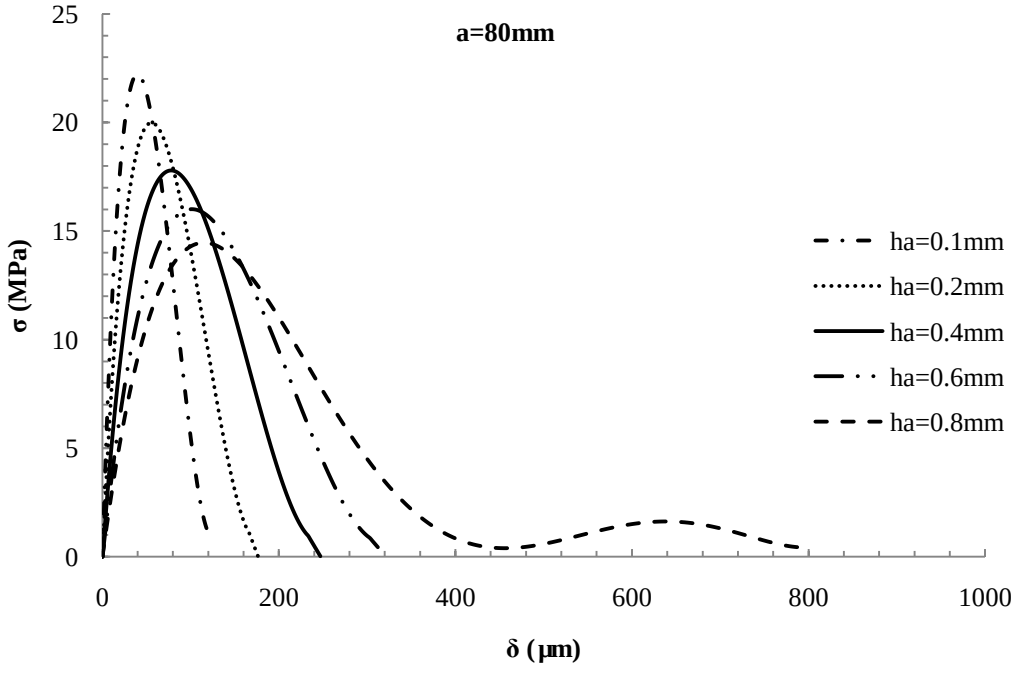

Figure 6.1.20: Typical shapes of the interfacial traction-separation laws of bonded steel with different bondline thicknesses h_a (a=20mm)

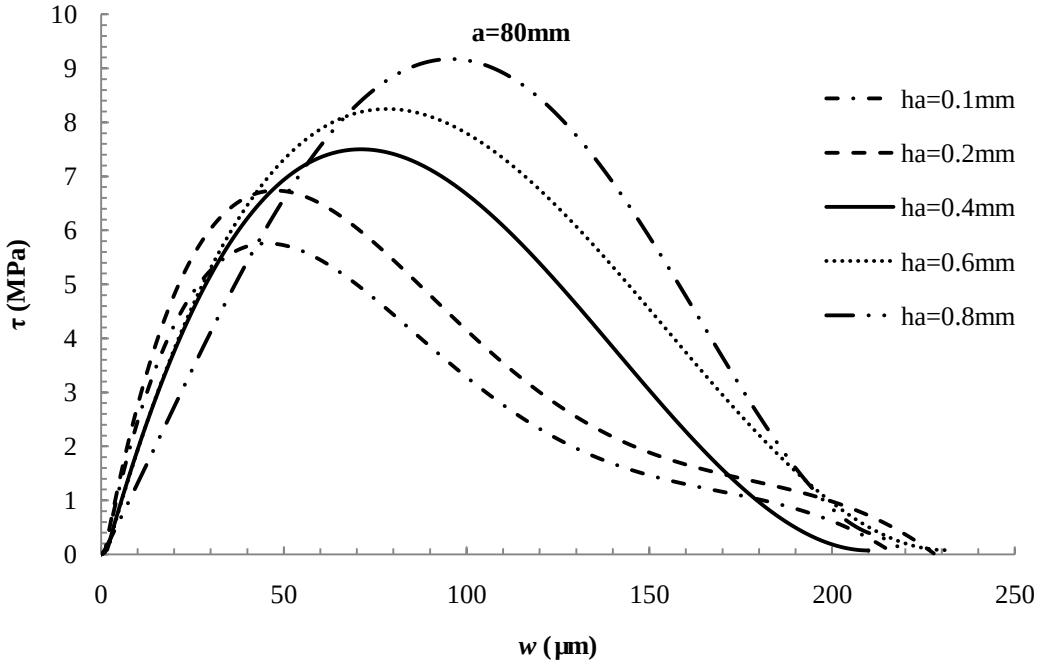

Figure 6.1.21: Typical shapes of the interfacial traction-slip laws of bonded steel with different bondline thicknesses h_a (a=20mm)

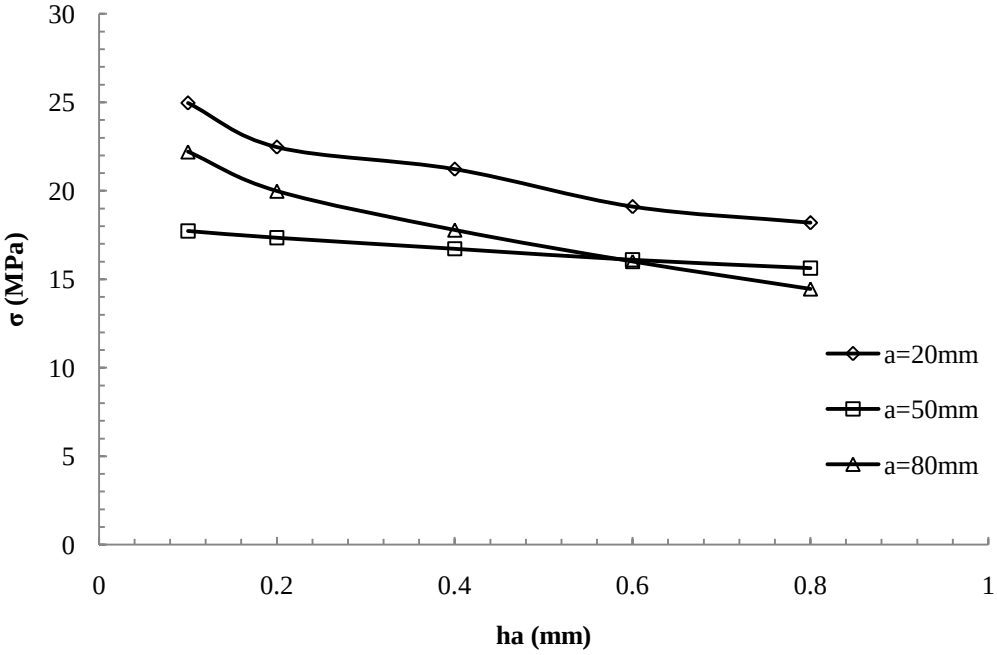

Figure 6.1.22: The effect of the adhesive thickness on the interfacial strength σ_{max} with different initial crack length

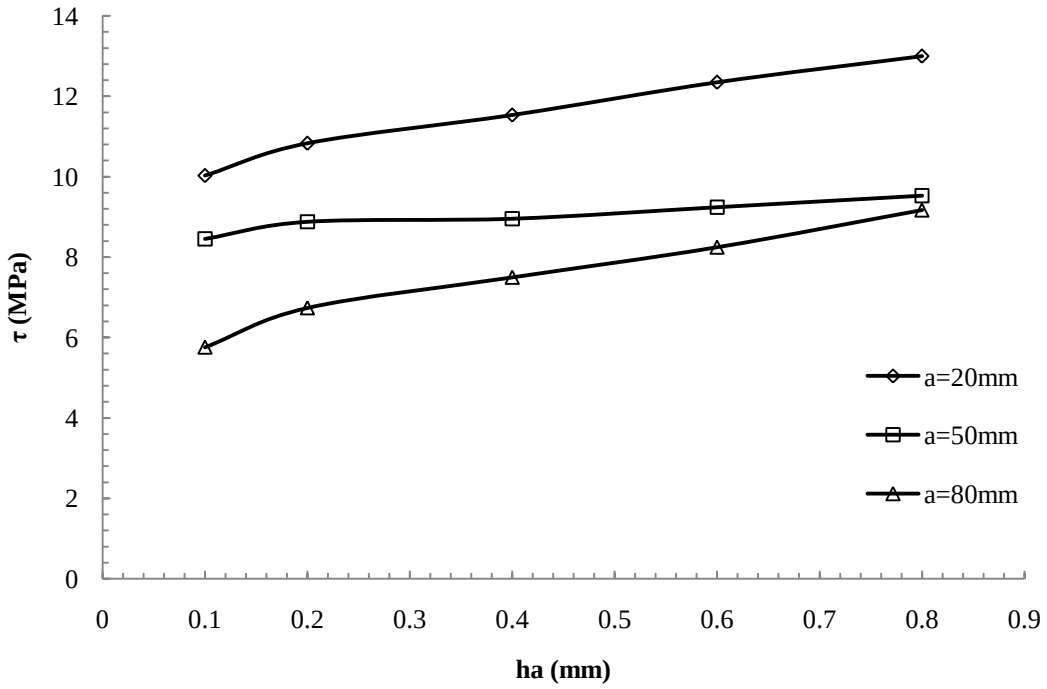

Figure 6.1.23: The effect of the adhesive thickness on the interfacial strength τ_{max} with different initial crack length

According to Fig. 6.1.22 and Fig. 6.1.23, as the initial crack tip length increased, the interfacial shear strength was decreased with the increased thickness of the adhesive layer. Additionally, as the initial crack tip length increased from a=20mm to a=50mm, the interfacial peel strength decreased with increased thickness of the adhesive layer. However, when the initial crack length increased from 50mm to 80mm and the thickness increased from 0.1mm to 0.6mm, the peel strength increased due to the increased moment and relative rotation angle which caused a compression zone near the crack tip area and prevented the crack propagation. Therefore, the peel strength increased. When the thickness increased from 0.6mm to 0.8mm, the bending stiffness of the adhesive layer increased and caused the decreased relative rotation angle. Therefore, the peel strength decreased without the compression zone around the crack tip area.

6.2 Test Results and Discussions of Mixed Mode I/II with Steel Based Specimen

6.2.1 Global and Local Test Results

The geometric parameters of each specimen are given in Table 6.2.1. A typical force vs. displacement curve (a specimen in ha=0.6mm with an initial crack length a=80mm) at the loading point is shown in Fig.6.2.1.

Table 6.2.1 Geometry of specimens

Average adhesive thickness (mm)	Length (mm)	Height (mm)	Width (mm)	Initial Crack Length (mm)	Initial Crack Length (mm)	Initial Crack Length (mm)
0.1	254.12	6.35	25.42	20.16	50.22	80.01
0.2	254.09	6.35	25.43	20.15	50.12	79.91
0.4	254.08	6.34	25.42	20.10	50.16	80.22
0.6	254.11	6.35	25.40	20.06	50.24	80.09
0.8	254.16	6.36	25.46	20.15	50.31	80.17

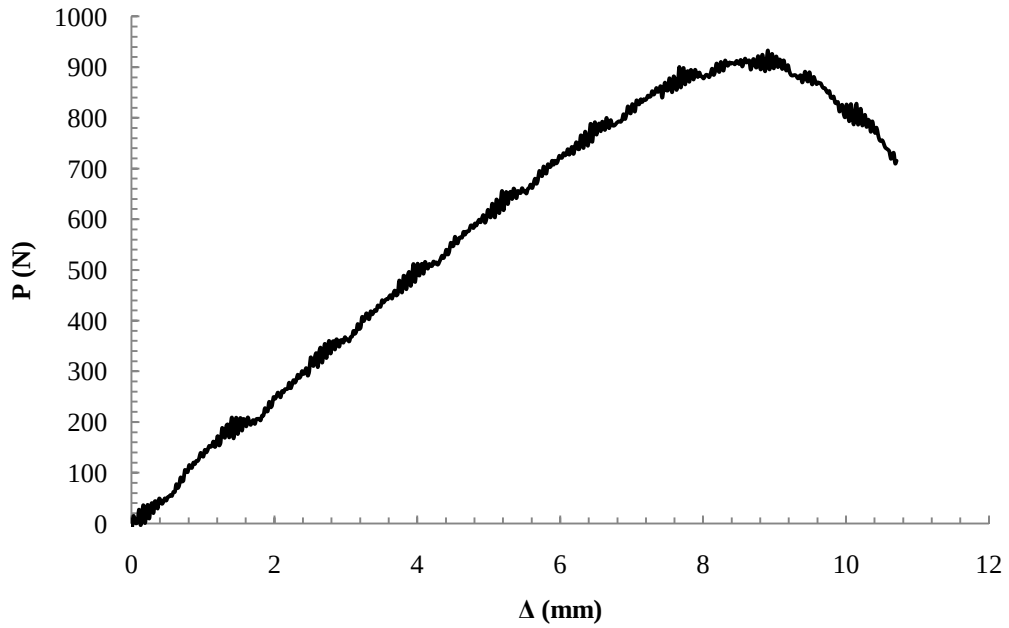

Figure 6.1.1: A typical relationship between loadline displacements Δ and loadline bending force *P* for h_a=0.6mm with initial crack length a=80mm

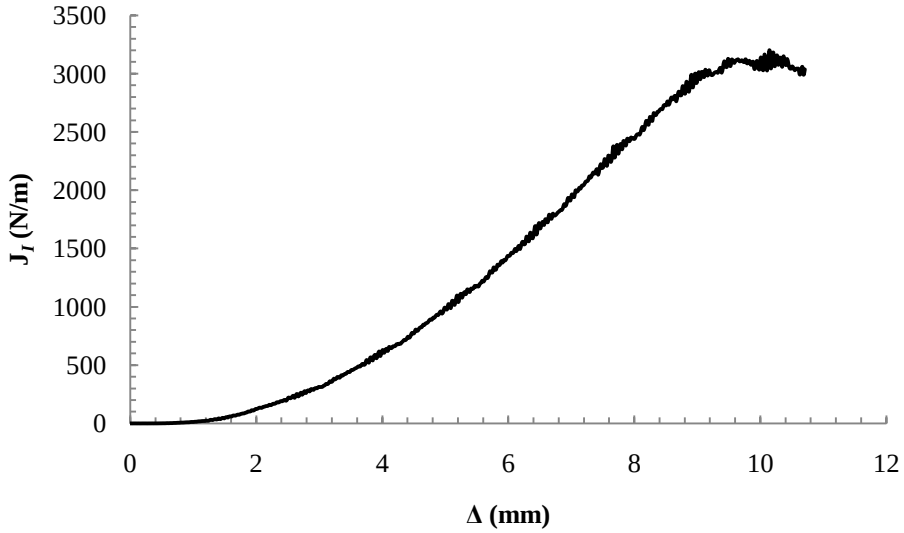

Figure 6.2.2: A typical relationship between loadline displacements Δ and energy release rate *J* for specimen with ha=0.6mm (*a*=80mm)

The force linearly increased until the local damage occurs. The load nonlinearly increases until the crack initiation process is completed. After that, the crack tip starts propagating. A continuous drop in the bending force was seen as the crack continuously propagated until the crack reached the specimen's end.

The data of the rotation angel at the loading point were collected by the inclinometer. With Eq. (2-50), the experimental energy release rate J_I is determined by combining the measured θ_P and P. A typical relationship (a specimen having ha=0.6mm with initial crack length of 80mm) between global energy release rate J and loadline displacement Δ is given in Fig. 6.2.2. In a real test, we found that it was fairly difficult to exactly define when the initial crack tip was propagated. Therefore, a characteristic strain energy release rate J_0 was defined which represented the J value when the maximum peel force P was reached. Note that with the growth of the crack, the global strain energy release rate keeps increasing as shown in Fig. 6.2.2 (J-Δ curve). This implies that the plastic dissipations beyond the crack tip must keep increasing during this stable growth

process. However, the increase of J becomes slower and slower as the crack grows, which seems nearly stable even by the end of the test. Therefore, an approximate asymptote is added in Fig. 6.2.2 to estimate the interfacial toughness of the bonded joints. And this estimated asymptotic value is denoted by J_{IC} or fracture energy

In this study, crack tip local deformations along the entire adhesive layer were recorded using the high resolution CCD camera. The value of the crack tip separation δ was measured as the relative normal displacement between the two laminate adherends at the location of the initial crack tip through the recorded digital images. By combining J_I-δ curve and crack tip separation δ, a typical experimental J_I-δ curve was obtained as shown in Fig. 6.2.3 (a specimen with ha=0.6mm and initial crack length of 80mm). With Eq. (2-50), the experimental J_I-δ curves were used to determine the equivalent interfacial traction-separation laws or σ=σ(δ), as show in Fig. 6.2.4.

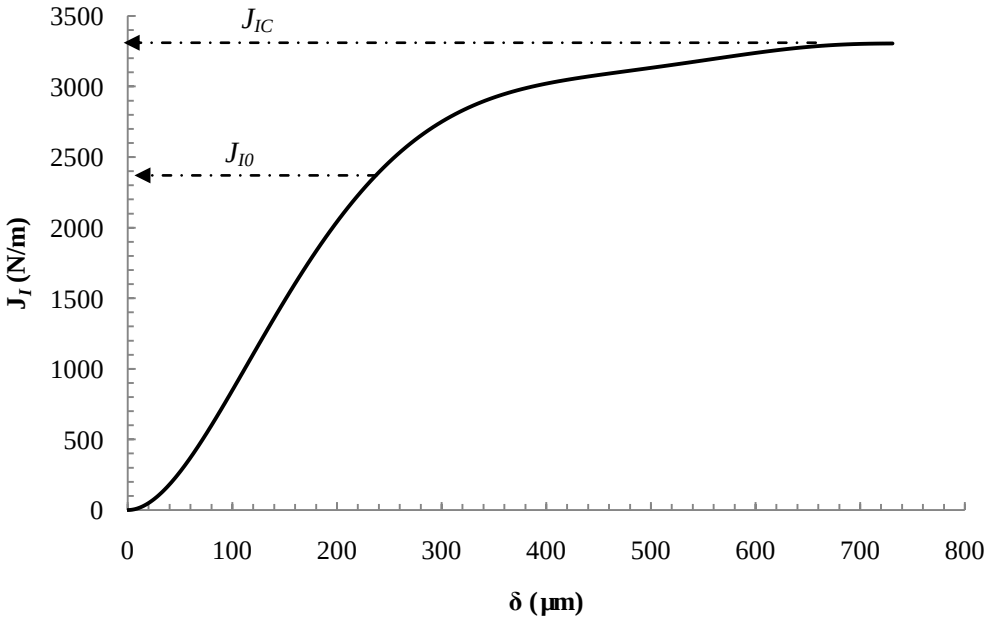

Figure 6.2.3: A typical relationship between energy release rate *J* and local crack tip separation *δ* for specimen with ha=0.6mm (a=80mm)

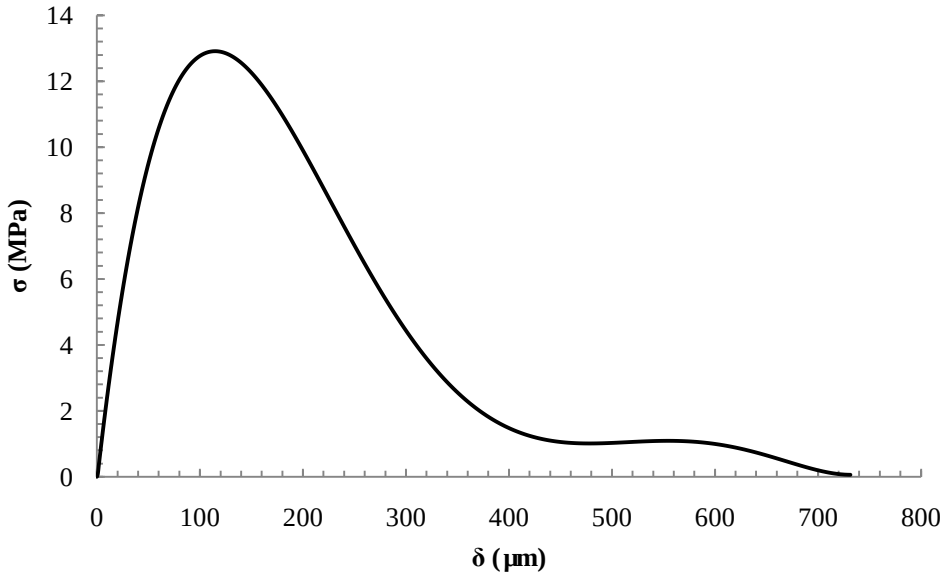

Figure 6.1.4: A typical shape of the equivalent interfacial traction-separation laws with ha=0.6mm (a=80mm) adhesive layer

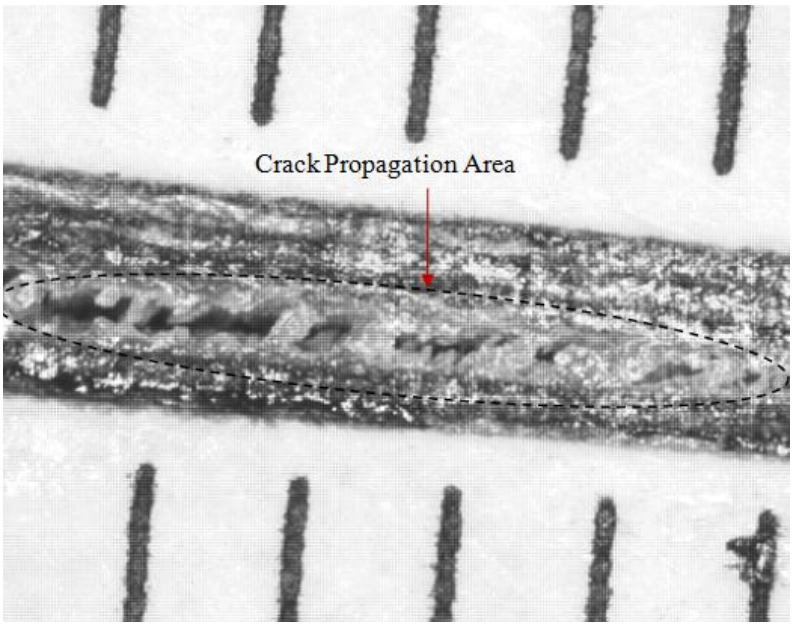

Figure 6.2.5: Local damage, fracture and deformation in the bondline

It was observed that the initial crack tip started opening as the shear load increased. It was also observed that the whiting zone appeared near the initial crack tip and was becoming more visible as the load was increased, as shown in Fig. 6.2.5 (circle area).

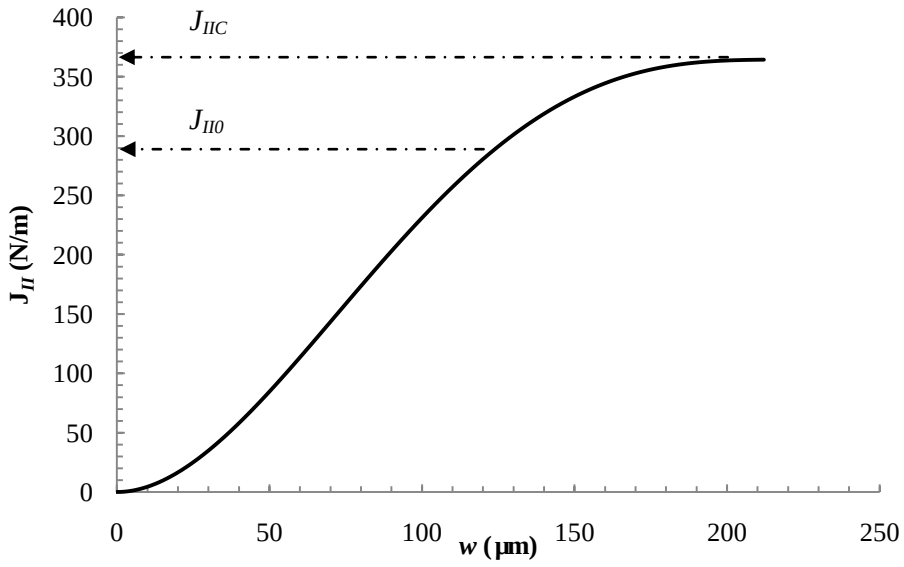

Figure 6.2.6: A typical relationship between energy release rate *J* and local crack tip slip *w* for specimen with ha=0.6mm (a=80 mm)

The value of the shear slip δ between the two adherends at the location of the initial crack tip is calculated based on the digital images. By combining P-Δ curve and local shear slip δ, according to Eq.(2-46), a typical experimental J_{II}-δ curve is obtained as shown in Fig. 6.2.6 (a specimen with ha=0.6mm and initial crack length 80mm). With Eq. (2-47), the experimental J_{II}-δ curves are used to determine the equivalent interfacial traction-separation laws or τ=τ(δ) at different adhesive thicknesses. A characteristic strain energy release rate J_0 is defined as the J value when the crack starts propagating immediately after the maximum fracture load P_{cr} is reached. It can be seen that J_0 is generally smaller than the critical strain energy release rate or the fracture energy J_{IIC}, which reflects that the strain energy release rate J_{II} keeps increasing after the crack propagation. This is because the plastic dissipation (or plastic zone) can be further increased after the crack initiation.

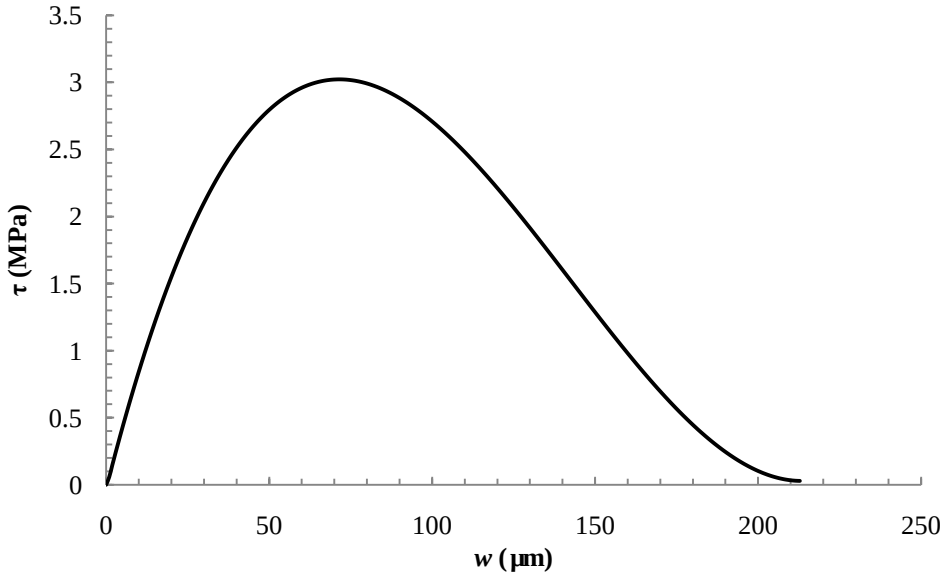

Figure 6.2.7: Typical interface constitutive relationship (equivalent cohesive law) for specimen with h_a=0.6 mm (a=80mm)

Based on Eq. (2-47), these experimental J_{II}-w curves are used to determine the equivalent interface cohesive laws or $\tau=\tau(w)$ at different adhesive thicknesses. Fig. 6.2.7 gives a typical shear stress vs. local slip displacement curve (a specimen in ha=0.6mm with initial crack length of 80mm).

6.2.2 Effects of the Thickness of the Adhesive Layer

With the global experiment results for different groups, the maximum peel loads are plotted as a function of the adhesive thicknesses (0.1 mm, 0.2 mm, 0.4 mm, 0.6 mm, and 0.8 mm) as shown in Fig. 6.2.8. It can be observed that the average peak load is increased from 2042.19 N to 2813.71 N when the thickness of adhesive layer increases (from 0.1 mm to 0.8 mm), as shown by the trend line in Fig. 6.2.8.

The increase in the adhesive layer thickness might increase the bending stiffness of the specimen. However, this contribution is very small since the adherends were made

of laminated composite with a thickness of 6.35 mm and much higher bending stiffness. The estimated average fracture energy J_{IC}, J_{IIC} and the average characteristic J_{I0}, J_{II0} (at the maximum peel load) were plotted as a function of the adhesive thickness in Fig. 6.2.9 and Fig. 6.2.10 (0.1 mm, 0.2 mm, 0.4 mm, 0.6 mm and 0.8 mm). The significant increase in J_0 and J_C are responsible for the increased load capacity when the adhesive thickness becomes thicker. Meanwhile, one may see that when the adhesive thickness is thin, J_0 and J_C are relatively close to each other. When it is relatively thick, J_0 and J_C are relatively departed. After data collecting and curve-fitting process of the experimental J-δ curves, by applying Eq. (2-50), one can see that the interfacial traction-slip laws are determined by numerically differentiating the experimental J-δ curves.

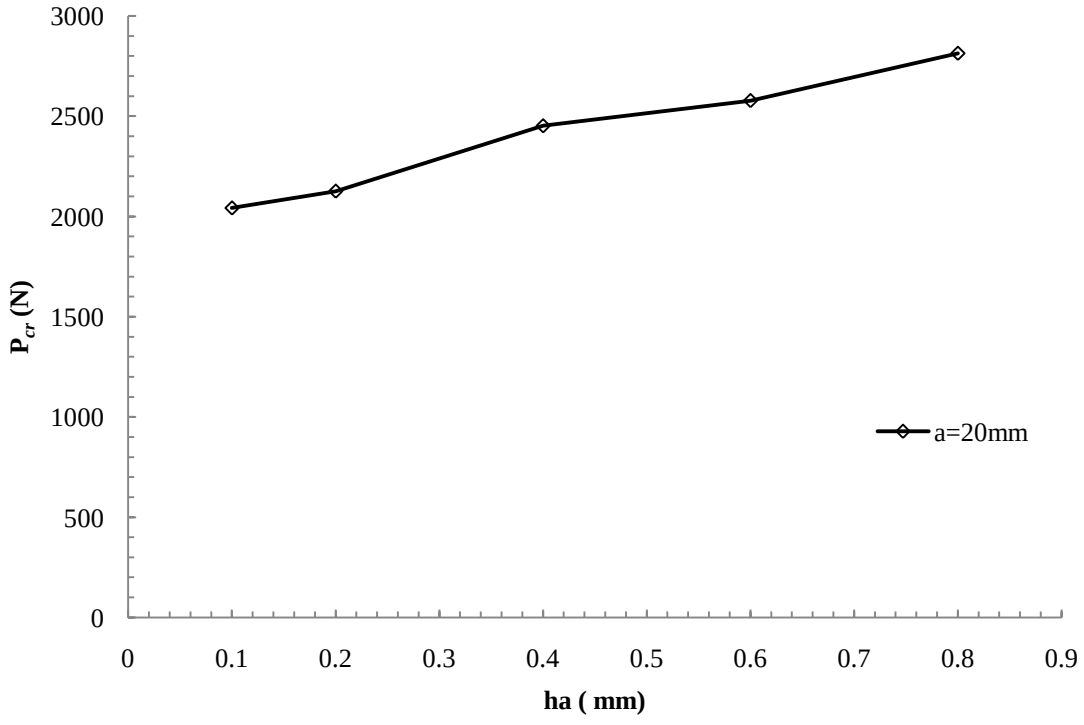

Figure 6.1.8: The average maximum shear load P_{cr} at different adhesive thicknesses h_a

A typical equivalent interfacial law of each group is given in Fig. 6.2.11 and Fig. 6.2.12 at different bondline thicknesses with initial crack length a=20mm. One may see that the effects of the bondline thickness on the interfacial traction-slip laws.

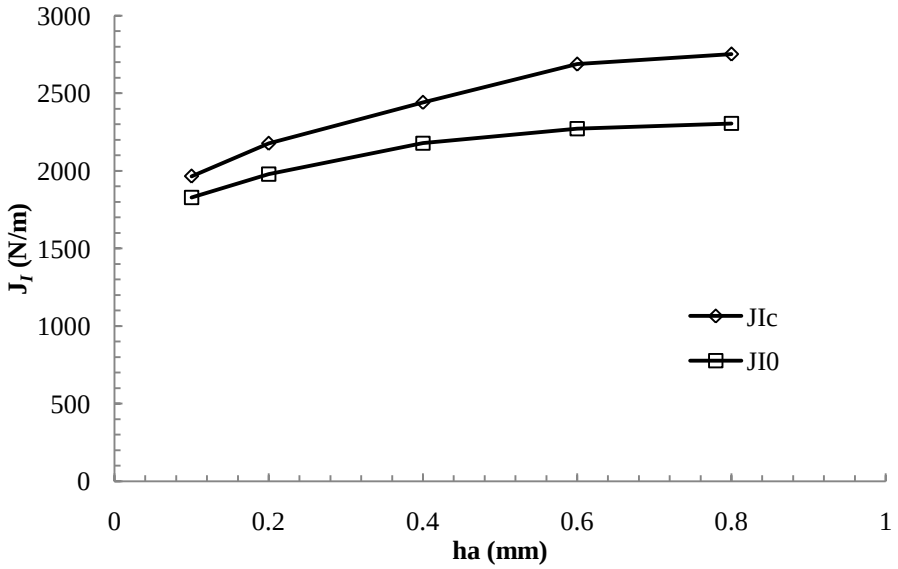

Figure 6.2.9: The estimated fracture energy J_{IC} and the characteristic energy release rate J_{I0} (corresponding to P_{cr}) with different adhesive thicknesses (a=20mm)

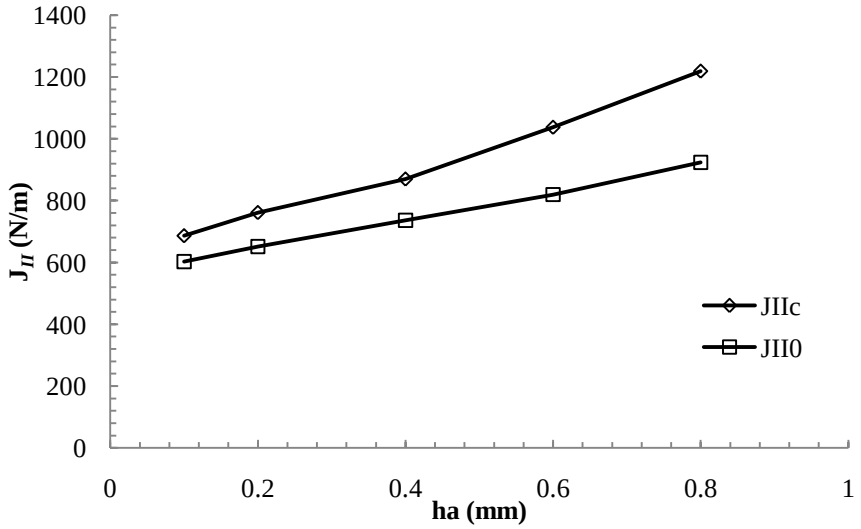

Figure 6.2.10: The estimated fracture energy J_{IIC} and the characteristic energy release rate J_{II0} (corresponding to P_{cr}) with different adhesive thicknesses (a=20mm)

- **Mode I Portion**

After data collecting and curve-fitting process of the experimental *J*-δ curves, by applying Eq. (2-51), one can see that the interfacial traction-separation laws were determined by numerically differentiating the experimental *J*-δ curves. The cohesive law was calculated for each specimen. The typical equivalent cohesive law of each group is given in Fig.6.2.11 at different adhesive thicknesses. From Fig. 6.2.11, one can see that three major effects of the adhesive thickness. First, the local characteristic separation (δ_0) corresponding to the interfacial strength σ_{max}, decreases with the decrease of the adhesive thickness. Second, the interfacial strength increases with the decrease of the adhesive thickness. Finally, the total area under the δ-σ curve, which represents the strain energy release rate at crack propagation, increases with the increase of the adhesive thickness.

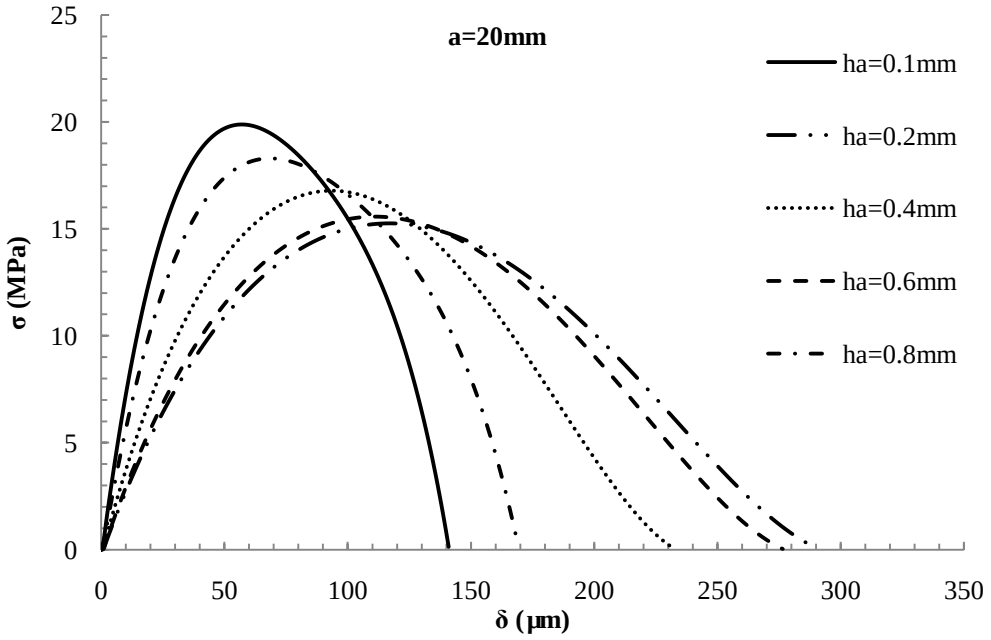

Figure 6.2.11: Typical shapes of the interfacial traction-separation laws of bonded steel with different bondline thicknesses h_a (a=20mm)

- **Mode II Portion**

First, the interfacial strength increases for laminated composite joint with the increase of the bondline thickness. Second, the initial stiffness of the interfacial laws (the initial slope of the τ-δ curve) is identical for laminated composite joints with various bondline thicknesses, which suggests that the shear deformation is controlled by the adhesive layer. Finally, the fracture energy (the total area under the δ-τ curve) increases with the bondline thickness. As shown in Fig. 6.2.10, the fracture energy J_{IIC} of the bonded joints is plotted as a function of the adhesive thickness. The fracture energy J_{IIC} at the thickness of 0.1 mm is increased by approximately 77.5% when the adhesive thickness becomes 0.8 mm. This significant increase in fracture energy can explain the increase in load capacity when the adhesive thickness is increased.

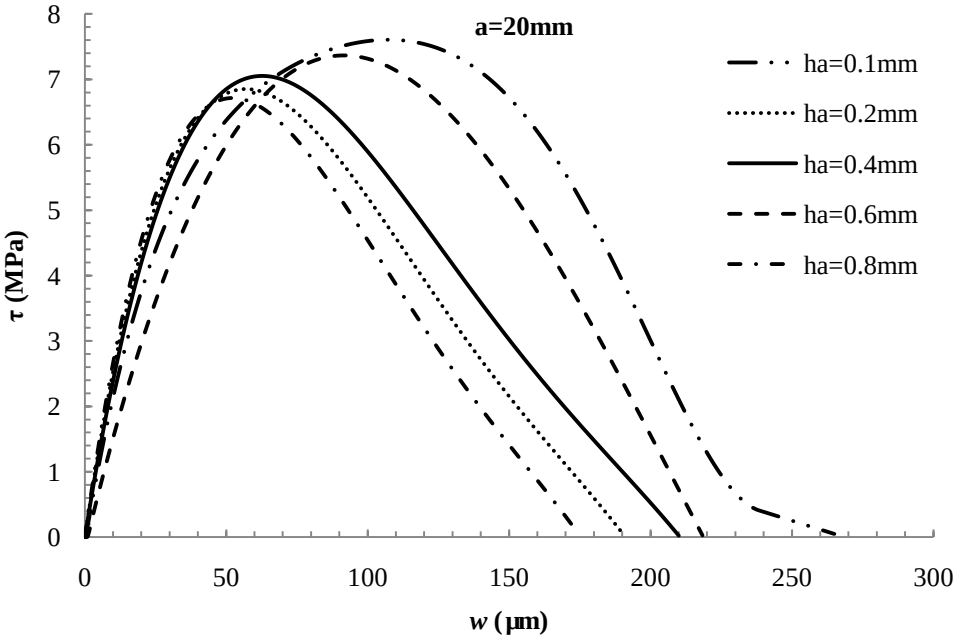

Figure 6.2.12: Typical shapes of the interfacial traction-slip laws of bonded steel with different bondline thicknesses h_a (a=20mm)

- **Mode Mixities**

The ratio of the estimated fracture energy J_{IIC} and total fracture energy (J_{IC} +J_{IIC}) with different adhesive thickness was plotted in Fig. 6.2.13. The ratio of the shear strength and total strength with different adhesive thickness was plotted in Fig. 6.2.14. It is observed that the ratio of the estimated fracture energy J_{IIC} and the ratio of the shear strength were increased as the thickness of the adhesive layer increased. It is implied that the ratio of mode I within the mixed mode I/II was decreased as the thickness of the adhesive layer increased. The stiffness of the adhesive layer is much lower than the stiffness of the adherends. As the thickness of the adhesive layer increased, the plastic dissipation increased due to the constraining of adherends.

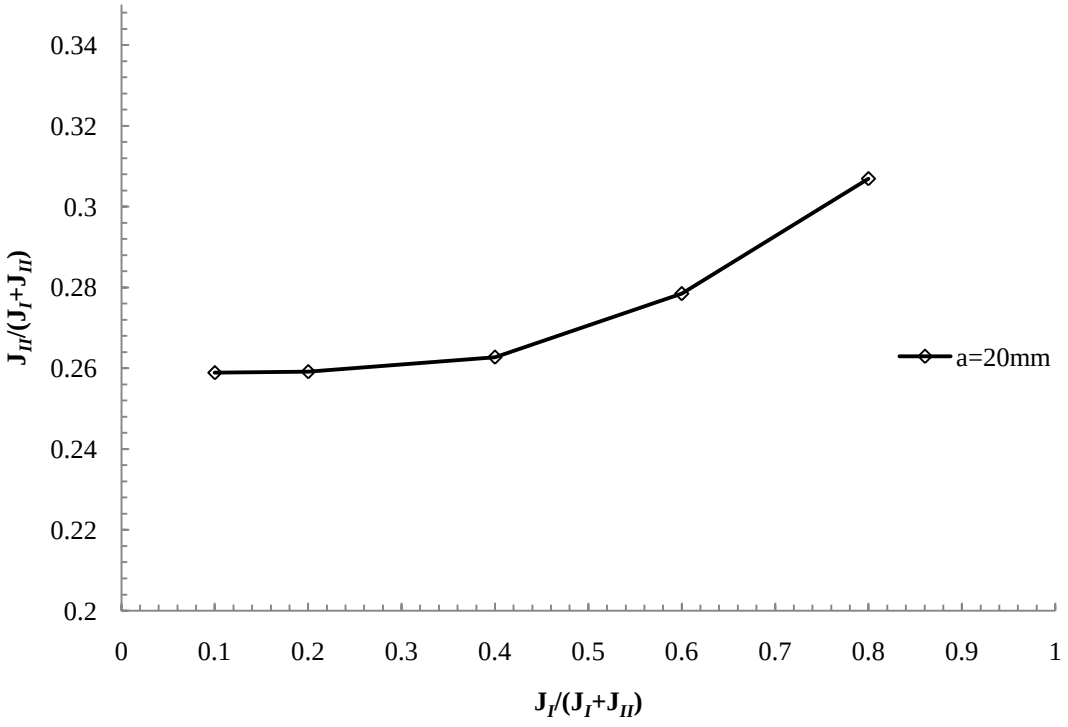

Figure 6.2.13: The ratio of the estimated fracture energy J_{IIC} and total fracture energy (J_{IC} + J_{IIC}) with different adhesive thicknesses (a=20mm)

6.2.3 Effects of the Initial Crack Tip Length of the Adhesive Layer

In this study, the effects of the initial crack tip length of the adhesive layer were also considered with different thicknesses of the adhesive layer. Three different initial crack lengths of a=20mm, 50mm, and 80mm were selected in this study. The maximum load P_{cr} at each initial crack length with different thicknesses of the adhesive layer was plotted in Fig. 6.2.15. It is observed that the maximum load was decreased as the initial crack length increased; the maximum load was increased as the thickness of the adhesive layer increased at each initial crack length. As the initial crack length increased at the same thickness of the adhesive layer, the bending moment was increased at the initial crack tip. It caused peeling force increase near the crack tip area at the same time. In other words, the mode I portion was increased as the initial crack length increased.

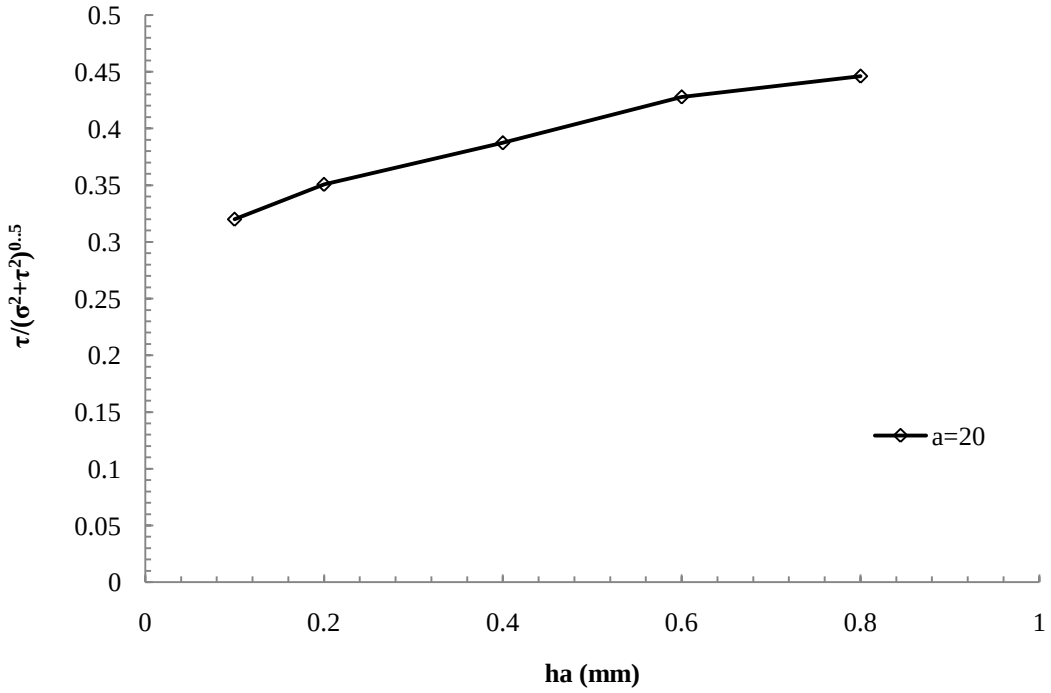

Figure 6.2.14: The ratio of the shear strength and total strength with different adhesive thicknesses (a=20mm)

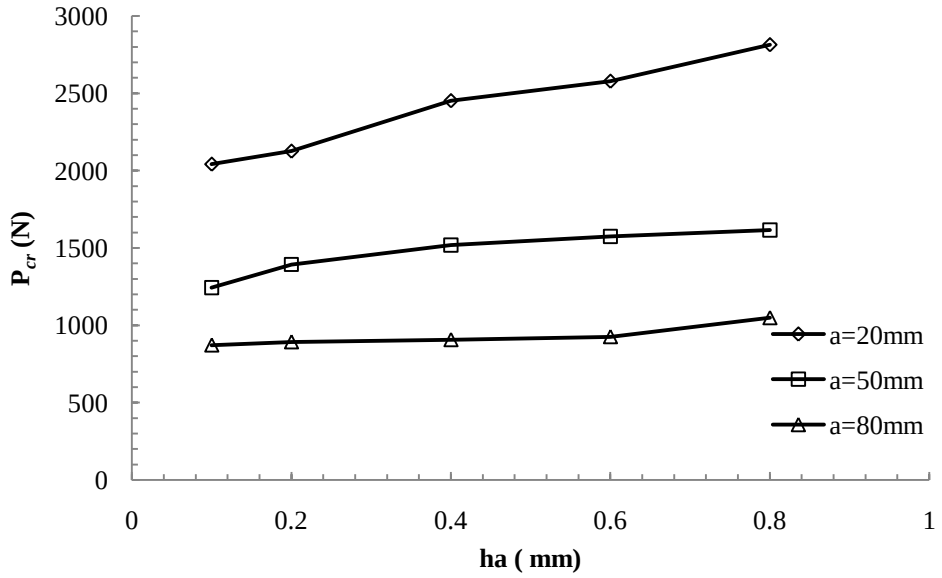

Figure 6.2.15: The average maximum shear load P_{cr} at different initial crack length with different adhesive thicknesses h_a

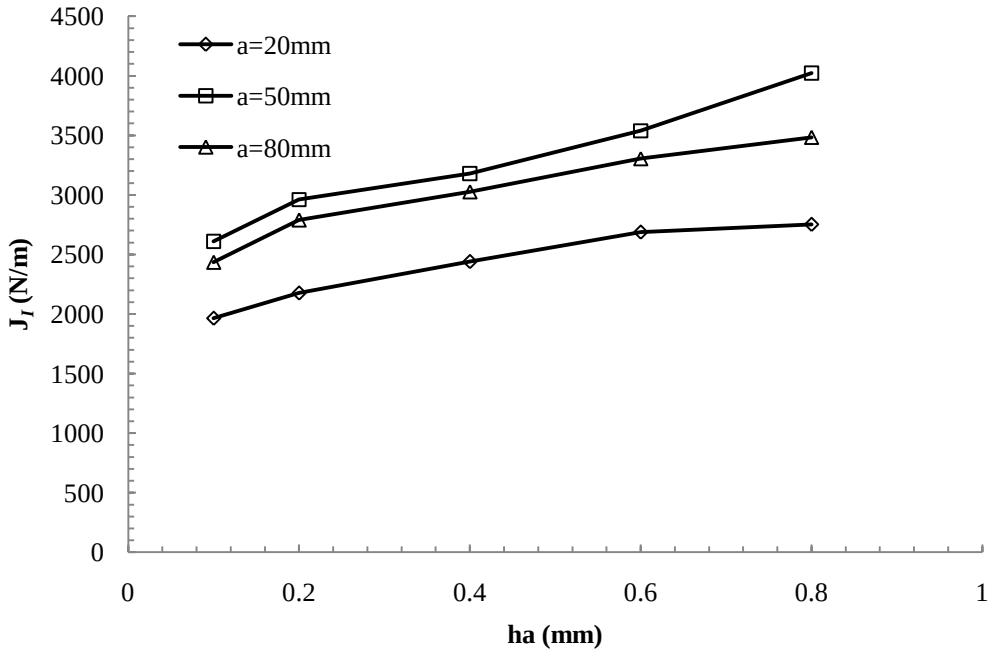

Figure 6.2.16: The estimated fracture energy J_{IC} at each initial crack length with different adhesive thicknesses

The estimated fracture energy J_{IC} and J_{IIC} at each initial crack length with different adhesive thickness were plotted in Fig. 6.2.16 and Fig. 6.2.17. It is observed that

the J_{IC} and J_{IIC} were increased at each initial crack length with different thicknesses of the adhesive layer.

The J_{IIC} was decreased as the initial crack length increased with the same thickness of the adhesive layer. It is understandable due to the decreased loading force as the initial crack length increased. Additionally, as the thickness of the adhesive layer increased, the relative rotation angle between the two adherends increased and caused the increase in shear force. However, the J_{IC} increased when the initial crack length at 20mm and 50mm. When the initial crack length reached 80mm, the fracture energy trending line is between the other trending lines with initial crack length at 20mm and 50mm. The phenomenon may be due to the combination the effect of the thickness of the adhesive layer and the initial crack length. This is a very interesting point.

When the thickness of the adhesive layer is 0.1mm, as the initial crack length increased, the mount of the adhesive material between the adherends decreased and the moment around the initial crack tip area increased. Additionally, the relative rotation angle between the two adherends increased and caused that the smallest peeling force can make the crack propagate, as shown in Fig. 6.2.15. According to Eq. (2-50): J_I=P*θ/4, although the loading force increased from 872N to 2042N as the initial crack length decreased from 80mm to 20mm, the relative rotation angle decreased from 11.17rad to 3.85rad. As the initial crack length a=50mm, the loading force is 1243N and the rotation angle is 8.39rad. As the thickness of the adhesive layer increased, the increased ratio of loading force and relative rotation angle is between the other two specimens (a=20mm and a=80mm). It can be explained that why the J_{IC} with initial crack length a=50 is larger than the other two, as the thickness of adhesive layer increased.

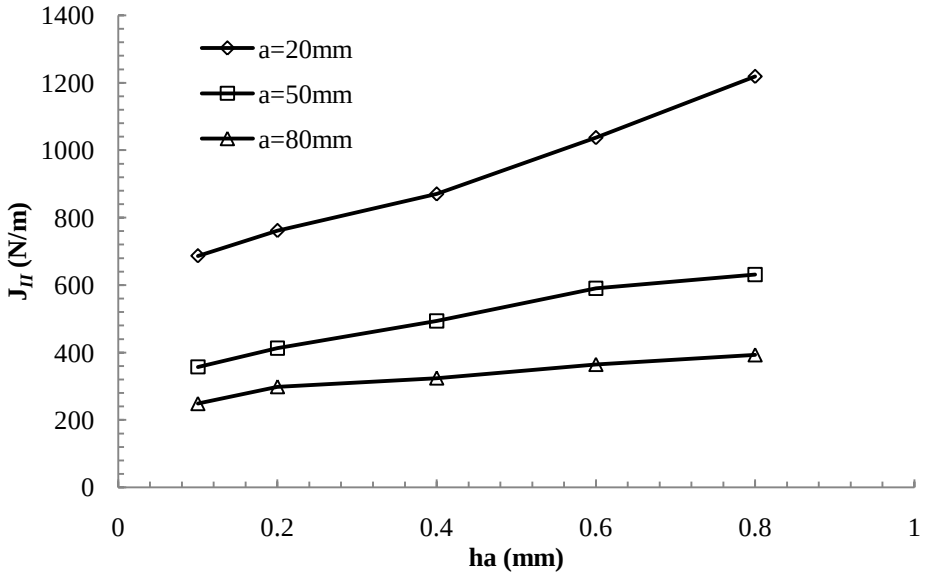

Figure 6.2.17: The estimated fracture energy J_{IIC} at each initial crack length with different adhesive thicknesses

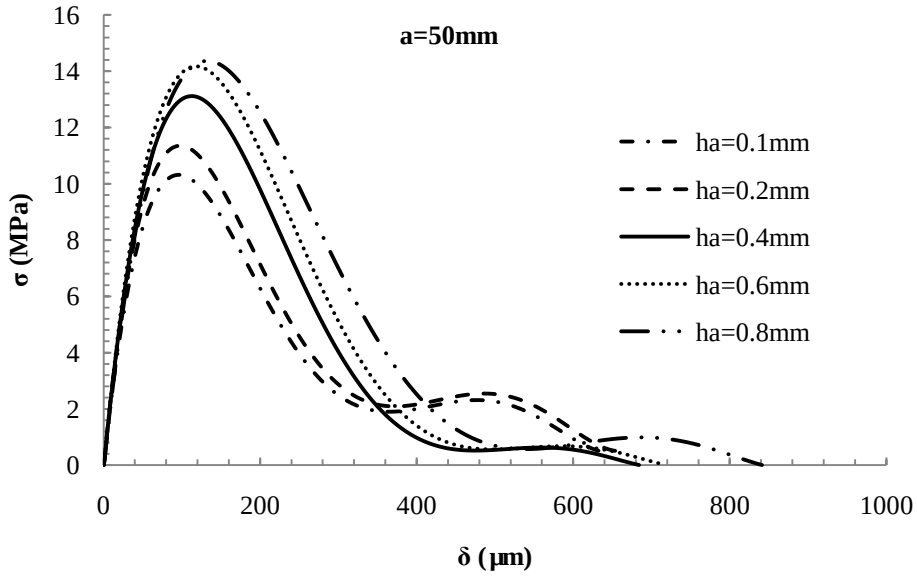

Figure 6.2.18: Typical shapes of the interfacial traction-separation laws of bonded steel with different bondline thicknesses h_a (a=50mm)

Typical shapes of the interfacial traction-separation laws and traction-slip laws of bonded laminated composite with different bondline thickness were plotted in Fig.6.2.18 and Fig.6.2.19 (a=50mm), Fig.6.2.20 and Fig.6.2.21 (a=80mm). The interfacial strength

σ_{max}, τ_{max} at each initial crack length with different thicknesses of the adhesive layer were plotted in Fig. 6.2.22 and Fig. 6.2.23. For each initial crack length, first, the local characteristic separation (δ_0) corresponding to the interfacial strength σ_{max} decreased with the decrease of the adhesive thickness. Second, the interfacial strength increases with the decrease of the adhesive thickness. Finally, the total area under the δ-σ curve, which represents the strain energy release rate at crack propagation, increases with the increase of the adhesive thickness.

Additionally, the interfacial strength τ_{max} increases for composite joint with the increase of the bondline thickness. The initial stiffness of the interfacial laws (the initial slope of the τ-δ curve) is identical for composite joints with various bondline thicknesses, which suggests that the shear deformation is controlled by the adhesive layer. The fracture energy (the total area under the δ-τ curve) increases with the bondline thickness.

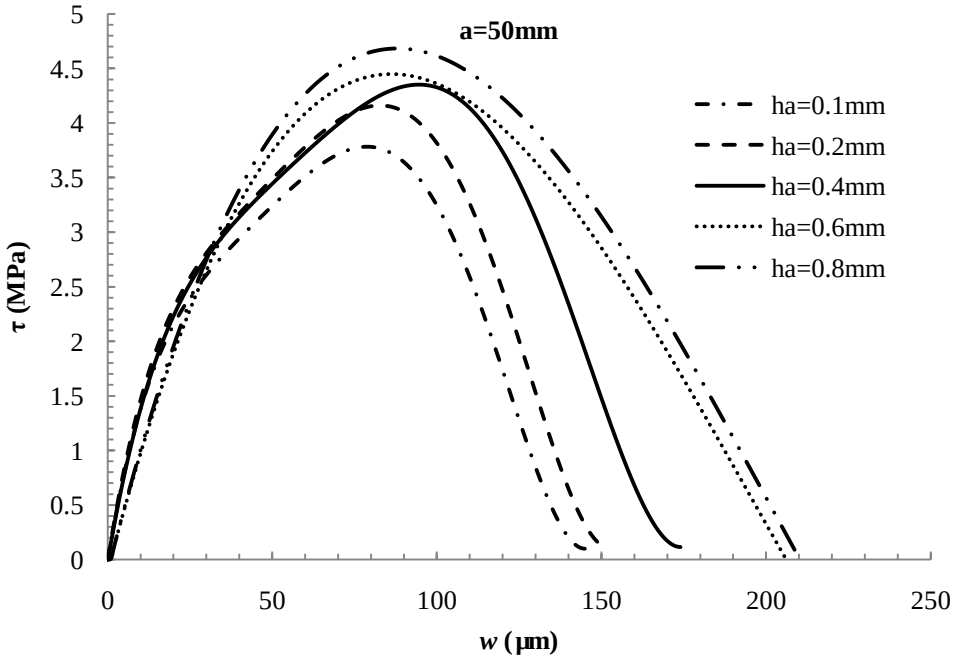

Figure 6.2.19: Typical shapes of the interfacial traction-slip laws of bonded steel with different bondline thicknesses h_a (a=50mm)

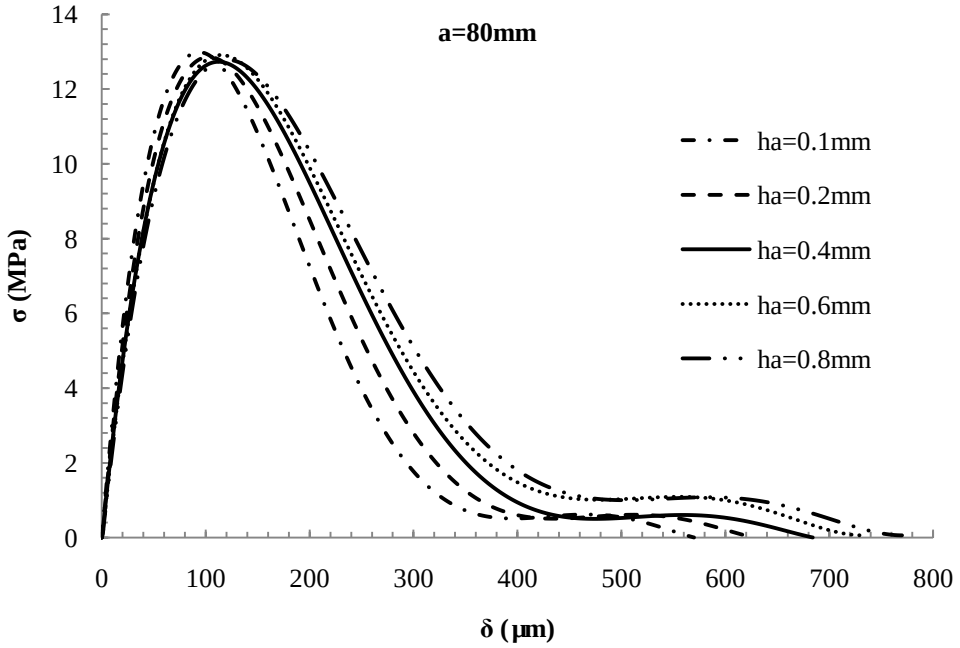

Figure 6.2.20: Typical shapes of the interfacial traction-separation laws of bonded steel with different bondline thicknesses h_a (a=80mm)

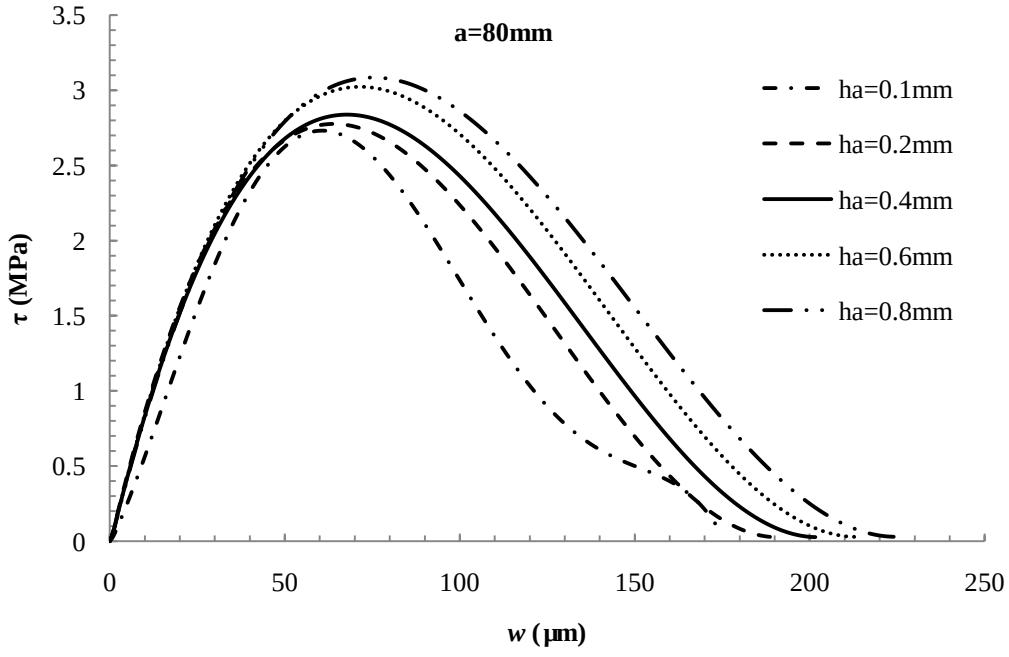

Figure 6.2.21: Typical shapes of the interfacial traction-slip laws of bonded steel with different bondline thicknesses h_a (a=80mm)

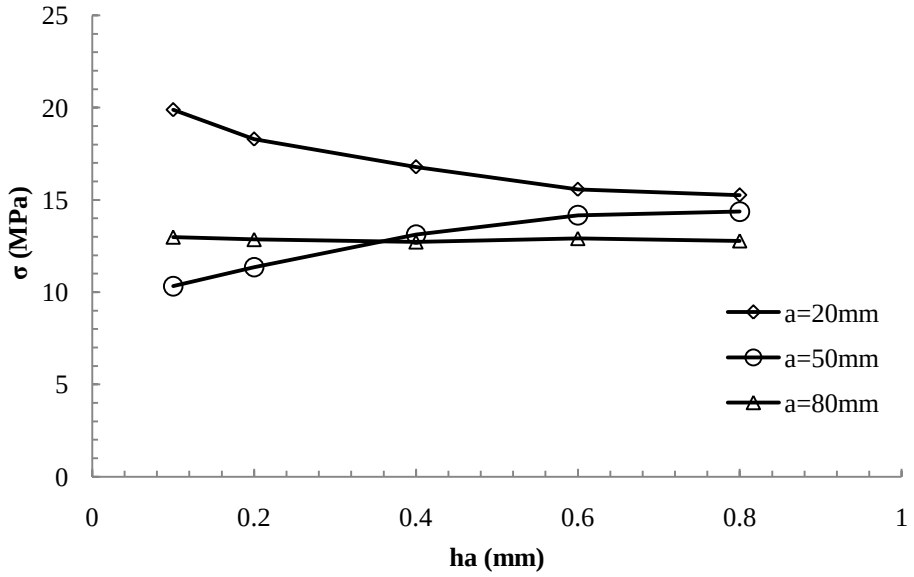

Figure 6.2.22: The effect of the adhesive thickness on the interfacial strength σ_{max} with different initial crack length

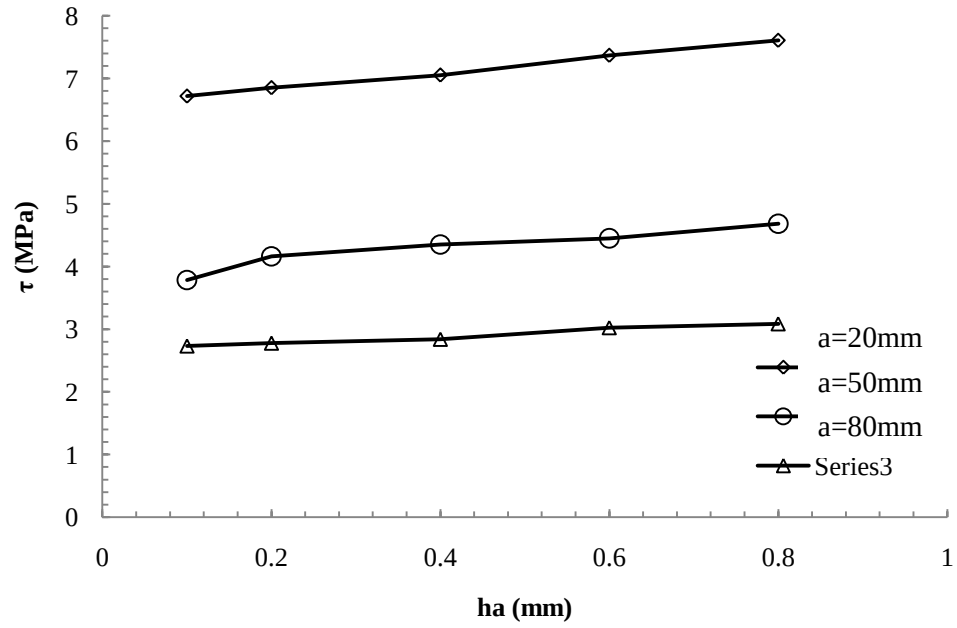

Figure 6.2.23: The effect of the adhesive thickness on the interfacial strength τ_{max} with different initial crack length

According to Fig. 6.2.22 and Fig. 6.2.23, as the initial crack tip length increased, the interfacial shear strength was decreased as the thickness of the adhesive layer increased. Additionally, as the initial crack tip length increased from a=20mm to

a=50mm, the interfacial shear strength decreased with increased thickness of the adhesive layer. However, when the initial crack length increased from 50mm to 80mm and the thickness increased from 0.1mm to 0.2mm, the shear strength increased due to the increased moment and relative rotation angle which caused a compression zone near the crack tip area and prevented the crack from propagation. Therefore, the normal strength increased. When the thickness increased from 0.2mm to 0.8mm, the bending stiffness of adhesive layer increased and caused the decreased relative rotation angle. Therefore, the normal strength decreased without the compression zone around the crack tip area.

CHAPTER 7

CONCLUSIONS AND FUTURE WORKS

7.1 Conclusions

Three fundamental fracture mechanics test (mode I, mode II, and mixed mode I/II) were conducted by the Double Cantilever Beam (DCB), End Notched Flexure (ENF), and Single Leg Bending (SLB) specimens with different adhesive thicknesses. According to the global test results of load and displacement and local test results of opening and slipping of initial crack tip under the quasi-static load, the fracture toughness and cohesive laws of traction-separation and traction-slipping (σ-δ and τ-δ curves) were developed with different thicknesses of adhesive layers. Based on the theoretical and experimental studies in this dissertation, some primary conclusions were made as follows.

7.1.1 Mode I Test

Both the steel based adherends and laminated composite based adherends of DCB specimens with different adhesive thicknesses experienced peel test (mode I test). Within the boundaries of the used materials parameters and based on the obtained data results, the following conclusions are yielded:

a) The adhesive thickness has an influence on the critical peel loadings. As the thickness of the adhesive layer increases, the critical force is increased.
b) As the adhesive thickness increases, the fracture toughness J_{IC} and characteristic energy J_{I0} (corresponding to critical load) are increased.
c) The increasing rate of peel loadings and fracture toughness J_{IC} with adhesive thickness slows down when the adhesive layer is thicker than a certain value; it

seems that the critical peel loadings and toughness are approaching an upper limit, respectively, as the thickness of adhesive layer increases.

d) The local crack tip separation δ is also increased, as the thickness of the adhesive layer increases. However, the major contribution was made by the enlarged plastic zone and plastic strain, instead of elastic deformation in the adhesive layer.

e) The thickness of the adhesive layer also has an important effect on the measured equivalent interfacial normal strength (σ_f). However, this effect was opposite for steel joints and composite joints. The interfacial normal strength σ_f decreases for steel joints while increases for composite joints as the thickness of adhesive layer increases. This phenomenon seems caused by the different constraining effects from the adherends which alters the local stress distribution.

f) The present work presents the experimental results that the interfacial normal strength σ_f was approximately 88 MPa which was about 3 times of the yield strength of the bulk adhesive when the adhesive thickness was 90 μm (steel specimen). The test data implied that localized stress could be very high when the proper constraints and loading conditions are applied.

7.1.2 Mode II Test

In this dissertation, the steel based adherends and laminated composite based adherends of cracked adhesively bonded joints are subjected to mode II loading using Edge Notched Flexure (ENF) specimens. Within the boundaries of the used materials parameters and based on the test results, the following conclusions are obtained:

a) Similar to Mode I test, the thicker adhesive thickness is, the higher the critical loading force is.

b) As the adhesive thickness increases, the fracture toughness J_{IIC} and characteristic energy J_{II0} (corresponding to critical load) are increased.

c) The local crack tip slipping δ is *a*lso increased as the thickness of the adhesive layer increases due to the significant plastic flowing through the thickness of adhesive layer.

d) The thickness of the adhesive layer also has a considerable effect on the fracture strength (τ_f). Different from DCB test (Mode I), for the ENF tests, the interfacial shear strength τ_f increases for both steel and composite joints when adhesive layer's thickness increases. The results implied that how the adherends' constraining affects the interfacial strength also depends on how the specimens are loaded.

7.1.3 Mixed Mode I/II Test

In this work, the steel based adherends and laminated composite based adherends of cracked adhesively bonded joints are subjected to mixed mode I/II loading using single leg bending (SLB) specimens. The objective is to measure the fracture toughness components (J_{IC} & J_{IIC}) and interfacial laws (σ-w and τ-δ curves) of the bonded joints corresponding to different thicknesses of the adhesive layer and different initial crack lengths. Within the boundaries of the used materials parameter and based on the test results, the following conclusions are derived:

a) The adhesive thickness has an influence on the critical loading force. As the thickness of adhesive layer increases, the critical force is increased; Meanwhile, the total fracture toughness increases as the adhesive thickness increases for the given initial crack length.

b) As the thickness of the adhesive layer increase, the local crack tip opening w and slipping δ are increased, too.

c) As the adhesive thickness decreases, both the interfacial normal strength σ_f and shear strength τ_f are increased with the given initial crack length.

d) As initial crack length increases, the critical loading force is decreased with the same adhesive thickness.

e) The fracture toughness J_{IIC} and fracture strength τ are increased as the initial crack length decreased with the same thickness of adhesive layer. It means the mode II portion is decreased as initial crack length increased.

f) [comments: this conclusion is opposite to (e)]:

g) However, the fracture toughness J_{IC} and normal strength (σ_f) are not always increased or decreased as the initial crack length increases. It is very complicated due to the combination effect of the initial crack length and adhesive thickness.

7.2 Future Works — Effects of Adhesive Thickness on the Fracture Behavior of Dissimilar Materials Joint

Modern manufacturing technologies require joining of dissimilar materials for fabrication of multi-material components and structures. A number of existing and emerging industrial applications are dependent on layered substrates with dissimilar materials. In addition to the apparent bi-material systems, laminated composite material & structures should also be treated as bi-material systems, because the plies and sections have different stiffness values due to different fiber orientations (being nonsymmetrical). Bi-material interfaces are thus quite common in various layered material and structure systems. Due to the different mechanical, physical, chemical, and thermal behaviors of

individual materials, bonding between dissimilar materials may exhibit interfacial properties different from that with identical materials. A bi-material system (or a hybrid joint) is thus referred to such systems in which two dissimilar materials are joined using a thin layer of adhesive interlayer. In despite of the importance of the problem, there were limited studies on characterizing the local interfacial laws of bonded dissimilar materials under pure Mode-I, Mode II, and Mixed Mode I/II loading.

Among those studies, very few studies focused on the effect of the thickness of the adhesive layer. The plan of the future study is to develop a simple while useful theoretical model and experimental method to reveal and characterize the effects of adhesive thickness on the interfacial fracture of hybrid joints.

REFERENCES

[1] Alfano, G., Crisfield, M.A., Finite element interface models for the delamination analysis of laminated composites: mechanical and computational issues. International Journal of Numerical Methods in Engineering, Vol. 50, 2001, pp. 1701-1736.

[2] Andersson, T., Stigh, U., 2004. The stress-elongation relation for an adhesive layer loaded in peel using equilibrium and energetic forces, *International Journal of Solids and Structures*, Vol. 41, pp. 413-434.

[3] Andersson, T., Biel, A., 2006. On the effective constitutive properties of a thin adhesive layer loaded in peel, International Journal of Fracture, Vol. 141, pp. 227-246.

[4] Andruet, R.H., Dillard, D.A. and Holzer, S.M., 2001. Two- and three-dimensional geometrical nonlinear finite elements for analysis of adhesive joints. International Journal of Adhesion and Adhesives, 21, 17-34.

[5] Atkinson, C., 1979, ‘‘Stress Singularities and Fracture Mechanics,’’ *Applied Mechanics Review*, 32 (2), pp. 123–135.

[6] Barenblatt, G. I., 1959, ‘‘The Formation of Equilibrium Cracks During Brittle Fracture. General Ideas and Hypothesis. Axisymmetrical Cracks,’’ *Journal of Applied Mathematics and Mechanics* (PMM), 23(3), pp. 622-636 (English Translation).

[7] Beer, F.P., Dewolf, J.T., 2004, Mechanics of materials.

[8] Blackman, B.R.K., Hadavinia, H., Kinloch, A.J. and Williams, J.G. 2003, “The Use of a Cohesive Zone Model to Study the Fracture of Fibre Composites and Adhesively-Bonded Joints,” *International Journal of Fracture*, 119, pp. 25-46.

[9] Boeman, R., Erdman, D., Lynn Klett, and Lomax, R., 1999, A Practical Test Method for Mode I Fracture Toughness of Adhesive Joints with Dissimilar Substrates, Proc. SAMPE-ACCE-DOE Advanced Composites Conference, Sept. 27-28, Detroit, Michigan, pp. 358-366.

[10] Bruno, D., Greco, F., 2001, Mixed mode delamination in plates: a refined approach, International Journal of Solids and Structures, Vol. 38, pp. 9149–9177.

[11] Bruno, D., Greco, F., Lonetti, P., 2005, A 3D delamination modelling technique based on plate and interface theories for laminated structures, European Journal of Mechanics A/Solids, Vol. 24, pp. 127–149.

[12] Camacho, G. T., and Ortiz, M., 1996, "Computational Modeling of Impact Damage in Brittle Materials," *International Journal of Solids and Structures*, 33, pp. 2899–2938.

[13] Chai, H., 1988. Shear fracture, International Journal of Fracture, Vol. 37, 137-159.

[14] Chai, H., 1995. Deformation and fracture of particulate epoxy in adhesive bonds, Acta Metallurgica Materialia, Vol. 43, pp. 163-172.

[15] Chowdhury, S. R. and Narasimhan, R., A finite element analysis of stationary crack tip fields in a pressure sensitive constrained ductile layer, International Journal of Solids and Structures, Vol. 37, 2000,3079-3100.

[16] Corigliano, A., 1993. Formulation, identification and use of interface models in the numerical analysis of composite delamination. International Journal of Solids and Structures, Vol. 30 (20), pp. 2779–2811.

[17] Davidson, B.D., Hurang, H., Schapery, R.A., 1995, An analytical crack-tip element for layered elastic structures, ASME Journal of Applied Mechanics, Vol. 62, pp. 294–305.

[18] Davidson, B.D., Hurang, H., Schapery, R.A., 1995, An analytical crack-tip element for layered elastic structures, ASME Journal of Applied Mechanics, Vol. 62, pp. 294–305.

[19] Dugdale, D. S., 1960, ''Yielding of Steel Sheets Containing Slits,'' *Journal of the Mechanics and Physics of Solids*, 8, pp. 100–104.

[20] England, A.H., 1965, A crack between dissimilar media. ASME Journal of Applied Mechanics, Vol. 32, pp. 400–402.

[21] Erdogan, F., 1965, Stress distribution in bonded dissimilar materials with cracks. ASME Journal of Applied Mechanics, Vol. 32, pp. 403–410.

[22] Evans, A.G., Ruhle, M., Dalgleish, B.J., Charalambides, P.G., 1990, The fracture energy of bimaterial interfaces, Materials Science and Engineering A, Vol. 126, pp. 53–64.

[23] Griffith, A. A. 1921, "The phenomena of rupture and flow in solids", Philosophical Transactions of the Royal Society of London, A 221: 163–198,

[24] Hillerborg A., Modéer M., Petersson P.E., 1976, "Analysis of Crack Formation and Crack Growth in Concrete by means of Fracture Mechanics and Finite Elements," *Cement and Concrete Research*, 6, pp.773-782.

[25] Högberg, J.L., 2006, Mixed mode cohesive law, International Journal of Fracture, Vol.141, pp. 549–559.

[26] Hutchinson, J. W., and Evans, A. G., 2000, ‘‘Mechanics of Materials: Top-down Approaches to Fracture,’’ *Acta Materialia*, 48, pp. 125–135.

[27] Hwu, C. and Hu, J. S., 1992, Stress intensity factors and energy release rates of delaminations in composite laminates. Engineering Fracture Mechanics, Vol. 42 (6), pp. 977–988.

[28] Ikeda, T., Yamashita, A., Lee, D., Miyazaki, N., 2000. Failure of a ductile adhesive layer constrained by hard adherends, Journal of Engineering Materials and Technology, Vol. 122, pp. 80-85.

[29] Irwin, G. R. and Kies, J. A. 1954, Critical Energy Rate Analysis of Fracture Strength. Weld. J. 33, Welding Research Supplement, 193-s– 198-s

[30] Ji, G., Ouyang, Z., Li, G., Ibekwe, S., and Pang, S.S. Effects of Adhesive Thickness on Global & Local Mode-I Interfacial Fracture of Bonded Joints. *International Journal of Solids and Structures* 2010 (in revision).

[31] Kafkalidis, M. S., Thouless, M. D., Yang, Q. D. and Ward, S. M., 2000, Deformation and fracture of adhesive layers constrained by plastically-deforming adherends, Journal of Adhesion Science and Technology, Vol. 14 (13), pp. 1593-1607.

[32] Kinloch, A.J. and Shaw, S.J., 1981. The fracture resistance of a toughened epoxy adhesive, Journal of Adhesion, Vol. 12, pp. 59-77.

[33] Klarbring, A., 1991, Derivation of a model of adhesively bonded joints by the asymptotic expansion method, International Journal of Engineering Science, Vol. 29, pp. 493-512.

[34] Lee, D., Ikeda, T., Miyazaki, N., Choi, N., 2004, Effect of Bond Thickness on the Fracture Toughness of Adhesive, Joints, Journal of Engineering Materials and Technology, Vol. 126 (1), pp. 14-18.

[35] Leffler, K., Alfredsson, K.S., Stigh, U., 2007. Shear behaviour of adhesive layers. International Journal of Solids and Structures, Vol. 44, 520-545.

[36] Li, S., et al., 2005, Use of a cohesive-zone model to analyze the fracture of a fiber-reinforced polymer-matrix composite. *Composites Science and Technology*, 65 (3-4): pp. 537-549.

[37] Lorenzis, L. D. and Zavarise, G., 2009, Cohesive zone modeling of interfacial stresses in plated beams, International Journal of Solids and Structures, Vol. 46, pp. 4181-4191.

[38] Madhusudhana, K.S., Narasimhan, R., 2002. Experimental and numerical investigations of mixed mode crack growth resistance of a ductile adhesive joint, Engineering Fracture Mechanics, Vol. 69, pp. 865-883.

[39] Mazza, P "A new Palaeolithic discovery: tar-hafted stone tools in a European Mid-Pleistocene bone-bearing bed". Journal of Archaeological Science 33: 2006, 1310.

[40] Moura, M.F.S.F. de, Campilho, R.D.S.G.and Gonçalves, J.P.M., 2009. Pure mode II fracture characterization of composite bonded joints, *International Journal of Solids and Structures*, vol. 46(6), pp. 1589-1595.

[41] Needleman, A., 1987, "A Continuum Model for Void Nucleation by Inclusion Debonding," ASME *Journal of Applied Mechanics*, 54, pp. 525-531.

[42] Nguyen, C. and Levy, A. L., 2009, An exact theory of interfacial debonding in layered elastic composites, International Journal of Solids and Structures, Vol. 46, pp. 2712–2723.

[43] Ouyang, Z. and Li, G. 2009a, "Local Damage Evolution of DCB Specimens during Crack Initiation Process: A Natural Boundary Condition Based Method," ASME *Journal of Applied Mechanics*, 76, pp. 051003-1-051003-8.

[44] Ouyang, Z. and Li, G., 2009b, Nonlinear Interface Shear Fracture of End Notched Flexure Specimens, *International Journal of Solids and Structures*, vol. 46(13), pp. 2659-2668.

[45] Ouyang, Z. and Li, G., 2009c, Cohesive Zone Model Based Analytical Solutions for Adhesively Bonded Pipe Joints under Torsional Loading, *International Journal of Solids and Structures*, vol. 46(5), pp. 1205-1217.

[46] Ouyang, Z. and Li, G., 2009d, Interfacial Debonding of Pipe Joints under Torsion Loads: A Model for Arbitrary Nonlinear Cohesive Laws, *International Journal of Fracture*, vol. 155(1), pp. 19-31.

[47] Pan, J., Leung, C.K.Y., 2007. Debonding along the FRP-concrete interface under combined pulling/peeling effects, *Engineering Fracture Mechanics*, 74, 132-150.

[48] Pardoena, T., Ferracina, T., Landisb, C.M. and Delannay, F., 2005, Constraint effects in adhesive joint fracture, Journal of the Mechanics and Physics of Solids, Vol. 53, 1951–1983.

[49] Parrinello, F., Failla, B. and Borino, G., 2009, Cohesive–frictional interface constitutive model, International Journal of Solids and Structures, Vol. 46, pp. 2680-2692.

[50] Pardoena, T., Ferracina, T., Landisb, C.M. and Delannay, F., Constraint effects in adhesive joint fracture, Journal of the Mechanics and Physics of Solids, Vol. 53, 2005, 1951–1983.

[51] Raju, I.S., Crews Jr., J.H., Aminpour, M.A., 1988, Convergence of strain energy release rate components for edge-delaminated composite laminates, Engineering Fracture Mechanics, Vol. 30, pp. 383–396.

[52] Rice, J. R.; Sih, G. C., 1965, Plane problems of cracks in dissimilar media ASME Journal of Applied Mechanics, Vol. 32, pp. 418–423.

[53] Rice, J. R., 1968, "A Path Independent Integral and the Approximate Analysis of Strain Concentration by Notches and Cracks," *Journal of Applied Mechanics*, 35, pp. 379-386.

[54] Rice, J. R., 1988, Elastic fracture mechanics concepts for interfacial cracks. ASME Journal of Applied Mechanics, Vol. 55, pp. 98–103.

[55] Rose, J.H., Smith, J.R. and Ferrante, J., 1983, "Universal Features of Bonding in Metals, *Physical Review* B, 28, pp. 1835-1845.

[56] Salomonsson, K. and Andersson, T., 2008, Modeling and parameter calibration of an adhesive layer at the meso level, Mechanics of Materials, Vol. 40, pp. 48–65.

[57] Schapery, R.A. and Davidson, B.D., 1990, Prediction of Energy Release Rate for Mixed-mode Delamination using Classical Plate Theory, Applied Mechanics Review, 43(5), S281–S287.

[58] Sheinman, I., Kardomateas, G.K., 1997, Energy release rate and stress intensity factors for delaminated composite laminates, International Journal of Solids and Structures, Vol. 34, pp. 451–459.

[59] Sørensen, B.F., 2002. Cohesive law and notch sensitivity of adhesive joints, Acta Materialia, Vol. 50, pp. 1053-1061.

[60] Suo, Z. and Hutchinson, J.W., 1990, Interface crack between two layers, International Journal of Fracture Vol. 43, pp. 1–18.

[61] Tvergaard, V., 1990, "Effect of Fibre Debonding in a Whisker-Reinforced Metal,'' *Material Science and Engineering*, A, Vol. 125, pp. 203–213.

[62] Tvergaard, V., and Hutchinson, J. W., 1992, "The Relation between Crack Growth Resistance and Fracture Process Parameters in Elastic-Plastic Solids,'' *Journal of the Mechanics and Physics of Solids*, Vol. 40, pp. 1377–1397.

[63] Tvergaard, V., Hutchinson, J.W., 1994, Toughness of an interface along a thin ductile layer joining elastic solids, Philosophical Magazine, Vol. 70, pp. 641-656.

[64] Tvergaard, V., Hutchinson, J.W., 1996, On the toughness of ductile adhesive joints, Journal of the Mechanics and Physics of Solids, Vol. 44, pp. 789-800.

[65] Twisp, 2008, access http://en.wikipedia.org/wiki/File:Fracture_modes_v2.svg on 05/01/2010.

[66] Wei, Y. and Hutchinson, J.W., 1998. Interface strength, work of adhesion and plasticity in the peel test, International Journal of Fracture, Vol. 93, pp. 315-333.

[67] Williams JG., 1989, End corrections for orthotropic DCB specimens, Composite Science and Technology, Vol. 35, pp. 367-376.

[68] Williams J.G. and Hadavinia H., 2002, "Analytical Solutions for Cohesive Zone Models," *Journal of the Mechanics and Physics of Solids*, 50, pp. 809-825.

[69] Williams, M. L., 1959, The stress around a fault or crack in dissimilar media. Bulletin of the Seismological Society of America, Vol. 49, pp. 199-204.

[70] Wu, Z.S., Yuan H., and Niu, H., 2002. Stress transfer and fracture propagation in different kinds of adhesive joints. *Journal of Engineering Mechanics*, ASCE, 128 (5), 562-573.

[71] Xu, X. P., and Needleman, A., 1993, "Void Nucleation by Inclusion Debonding in a Crystal Matrix,'' *Modeling and Simulation in Materials Science and Engineering*, 1, pp. 111–132.

[72] Yan, C., Mai, Y, Ye, L., 2001, Effect of Bond Thickness on Fracture Behaviour in Adhesive Joints, The Journal of Adhesion, Vol. 75(1), pp.27- 44.

[73] Yan, Y. and Shang, F., 2009, Cohesive zone modeling of interfacial delamination in PZT thin films, International Journal of Solids and Structures, Vol. 46, pp.2739–2749.

[74] Yang, Q.D., Thouless, M.D., Ward, S.M., 1999, Numerical simulations of adhesively-bonded beams failing with extensive plastic deformation, Journal of the Mechanics and Physics of Solids, 47, pp. 1337-1353.

[75] Yang, Q.D., Thouless, M.D., Ward, S.M., 2001a. Elastic-plastic mode-II fracture of adhesive joints, International Journal of Solids and Structures, Vol. 38, pp, 3251–3262.

[76] Yang, Q.D., Thouless, M.D., Ward, S.M., 2001b, Mixed mode fracture analysis of plastically-deforming adhesive joints, International Journal of Fracture, Vol. 110, pp. 175-187.

[77] Zhu, Y., Liechti, K. M., Ravi-Chandar, K., 2009. Direct extraction of rate-dependent traction–separation laws for polyurea/steel interfaces, International Journal of Solids and Structures, Vol. 46 (1), pp. 31-51.

VITA

Gefu Ji was born in Wuhan, Hu Bei, P. R. China, in 1978. He received his bachelor degree of engineering in the specialty of mechanical and electrical engineering from Agricultural University in Wuhan, P. R. China, in June 2001. After receiving his undergraduate degree, Mr. Ji entered the Southern University A & M College in fall 2004 as a graduate assistant. Since entering S.U., Mr. Ji has been a co-investigator for two research projects. He received his Master of Engineering degree in August 2006. And then, he entered the Louisiana State University in fall 2006. He received another Master of Science degree in mechanical engineering in December 2008. He entered the doctoral program in engineering science in 2008. He is expected to receive the degree of Doctor of Philosophy in engineering science in December 2010.